Tombros, S., Kokkalas, S., Triantafyllidis, S., Fitros, M., Tsikos, H., Papadopoulou, L., Voudouris, P., Zhai, D., Skliros, V., Perraki, M., Kappis, K., Spiliopoulou, A., Simos, X., Papavasiliou, J., and Williams-Jones, A. 2023, Genesis of a new type of mangan skarn associated with peraluminous granitoids in Greece: Chemical Geology, v. 623, p. 121369

Modeling Mangan Skarn Formation Related to Peraluminous Granitoids in Greece

STYLIANOS F. TOMBROS[1],
STAVROS TRIANTAFYLLIDIS[2],
MICHALIS G. FITROS[3],
SOTIRIOS KOKKALAS[3],
ANNA-MARIA G. PAPASPYROU[4],
HARILAOS TSIKOS[3],
XENOFON C. SIMOS[3],
LAMBRINI PAPADOLOULOU[4]
PANAGIOTIS C. VOUDOURIS[5],
DEGAO ZHAI[6],
VASILEIOS SKLIROS[2],
MARIA PERRAKI[2],
KONSTANTINOS KAPPIS[1],
AIKATERINI SPILIOPOULOU[2],
JOAN PAPAVASILIOU[1], ANTHONY WILLIAMS-JONES[7] and
KONSTANTIN HATZIPANAGIOTOU[2].

[1]*Department of Materials Science, University of Patras, GR-26504 Rio Patras, Greece, stel@upatras.gr, tombrosfs@gmail.com, k.kappis@upatras.gr,*

[2]*School of Mining and Metallurgical Engineering, National Technical University of Athens, Iroon Polytechneiou 9, 157 80, Zografou, Athens, Greece, striantafyllidis@metal.ntua.gr, maria@metal.ntua.gr, sklirosbil/@gmail.com, spil.aikaterina@gmail.com/.*

[3]*Department of Geology, University of Patras, Rion, 26500, Patras, Greece, michalis.fitros92@gmail.com, fwntas.simos@gmail.com, skokalas@upatras.gr, htsikos@upatras.gr, K.Hatzipanagiotou@upatras.gr,*

[4]*Department of Mineralogy-Petrology-Economic Geology, School of Geology, Aristotle University of Thessaloniki, 54124, Thessaloniki, Greece, lambrini@geo.auth.gr,*

[5]*National and Kapodistrian University of Athens, Panepistimioupolis, Ano Ilisia 15784, Athens, Greece, voudouris@geol.uoa.gr,*

[6]*State Key Laboratory of Geological Processes and Mineral Resources, China University of Geosciences, Beijing, 100083, Beijing, China, zhaidgcugb@gmail.com,*

[7] *Department of Earth and Planetary Sciences, McGill University, 3450, Quebec, Canada, anthony.williams-jones@mcgill.ca.*

Tombros, S., Kokkalas, S., Triantafyllidis, S., Fitros, M., Tsikos, H., Papadopoulou, L., Voudouris, P., Zhai, D., Skliros, V., Perraki, M., Kappis, K., Spiliopoulou, A., Simos, X., Papavasiliou, J., and Williams-Jones, A. 2023, Genesis of a new type of mangan skarn associated with peraluminous granitoids in Greece: Chemical Geology, v. 623, p. 121369

Abstract

Mangan skarns and related manganese-oxide ore deposits are relatively uncommon. Two examples of mangan skarns were investigated in this study, namely the Panorama, Drama skarn in Rhodope and the Thapsana, Paros Island skarn in the Attico-Cycladic Metallogenic Massifs, respectively. The transitional calcic-to-mangan exoskarn at Panorama is exposed in a garnet-epidote zone (Grt-Ep), proximal to the Panorama granite-to-microgranite. At Thapsana, the mangan skarn is related to rhodonite (Rdn) (± vesuvianite), johannsenite-spessartine (Jhn-Sps) and spessartine-cummingtonite (Sps-Cum) zones, adjacent to marbles, and/or gneisses, and the Thapsana leucogranite, respectively. A two-stage manganese-oxide assemblage is present in the Thapsana, skarn and comprises jacobsite, hausmannite, braunite and magnetite (stage I) followed by hollandite, cryptomelane, vernadite, manjiroite and pyrite (stage II) with gangue rhodochrosite, calcite and ankerite, that was succeeded by a supergene stage with pyrolusite, manganite and Fe-oxides.

The Thapsana mangan skarn was deposited at a pressure of ~110 MPa, and a temperature of ~305° to 565°C, from an acidic (pH = 3.5 to 5.5), saline (~3.0 to ~48.0 wt. % NaCl equiv), carbonic, chlorine, manganese (~4390 ppm)-bearing, immiscible, mixed, skarn-forming fluids with elevated $\log[\alpha_{Mn}{}^{2+}/(\alpha_{H}{}^{+})^{2}]$ and $\log[\alpha_{Mn}{}^{3+}/(\alpha_{H}{}^{+})^{3}]$. Formation of the Thapsana mangan skarn was controlled by early boiling of metasomatic fluids (at ~480ºC and ~120 MPa), followed by late boiling (at ~400ºC and ~100 MPa), mixing and cooling. This conclusion is based on a study of fluid inclusions in spessartine of the Jhn-Sps zone. Stable and radiogenic isotopes (e.g., $\delta^{18}O$, δD, $\delta^{44}Ca_{BSE}$ and $\delta^{26}Mg_{DSM\text{-}3}$, $^{87}Sr/^{86}Sr$, U/Pb) suggest that the Panorama granite (dated at

~26.0 Ma) and Thapsana leucogranite (~7.4 Ma) were the sources for the metasomatic fluids at Thapsana (~6.3 to ~6.0 Ma) and Panorama (~24.8 Ma), respectively.

Thermodynamic simulation suggests that the manganoan skarn assemblages were formed due to simple cooling and fluid-rock interaction, controlled by pH increase and changes of the redox state of the metasomatic fluid and manganese activity. Fluid-rock interaction and cooling produced a mangan skarn paragenesis that comprises an early anhydrous paragenesis (Stage I), followed by complex hydrous manganoan oxides/hydroxides (Stage II). A metallogenic model for the formation of the mangan skarns is proposed based on field, mineralogical, lithogeochemical, isotope and fluid inclusion evidence and thermodynamic modeling. Our model suggests two different sources for manganese, namely the peraluminous granitoids, which were primarily enriched in manganese, and the host marbles and gneisses.

1. Introduction

Skarns are classified as magnesian, calcic, and mangan based on the skarn paragenesis and prevailing protolith composition (Meinert et al., 2005). Mangan skarns, and associated manganese ore deposits, linked to peraluminous granite and/or leucogranite are uncommon. Examples include Groundhog, San Antonio, Santa Eulalia and Naica, New Mexico, and Darwing, California, USA (Meinert, 1987; Megaw et al., 1988; Newberry, 1991), Nakatatsu, Japan (Shimizu and Iiyama, 1982), Yoenhwa-Ulchin, South Korea (Yun and Einaudi, 1982), Gasborn, and West Bergslagen, Sweden (Damman, 1989), Bajiazi, Liaoning and Shuikouskan, China (Zhao et al., 2003; Huang et al., 2015), Quartz Lake, Yukon, Canada (Liverton, 2016). The majority of mangan skarns exhibit features in exposure, mineralogy, zoning and related Mn-bearing or Pb-

Zn ore deposits (Zhao, 1991), which distinguish them from the magnesian and calcic skarns. Mangan skarns occur frequently along the lithological contacts of their host rocks, including dolomites, marbles and limestones, shales, manganiferous schists and quartzites. They appear as structurally-controlled veins, lenses or pipes, or along fault zones and typically relate to monzonites and/or granite porphyries. They are formed due to infiltration at temperatures ranging from 200º and 450ºC (Zhao, 1991) and most frequently post-date the calcic skarns. Mangan skarns comprise uncommon Mn-rich assemblages, which include Mn-olivine, i.e., tephroite, Mn-ilvaite and -vesuvianite, Mn-pyroxenoid, i.e., Mn-bearing-wollastonite, -babingtonite, rhodonite, bustamite and pyroxmangite, Mn-pyroxene, i.e., Mn-bearing-salite, -hedenbergite and johannsenite and Mn-garnet, i.e., spessartine (Zhao, 1991). Retrograde assemblages comprise Mn-amphibole, i.e., Mn-actinolite and -cummingtonite, piemontite and/or Mn-bearing epidote and rhodochrosite. Spatial zoning patterns include proximal spessartine and/or Mn-vesuvianite and distal johannsenite and Mn-hedenbergite, whereas the Mn-pyroxenoids occur adjacent to the host marbles and/or schists (Zhao, 1991; Meinert, 1987; Meinert et al., 2005; Yun and Einaudi, 1982).

Two mangan skarns were investigated. They are associated with Oligocene to Miocene alkaline-to-calc-alkaline porphyry intrusions in the Rhodope (NE Greece, Fig. 1A) and Attico-Cycladic (Fig. 1B) Metallogenic Massifs. They are exposed at Panorama in Drama (Fig. 1C, after Papaspyrou, 2016) and Thapsana in Paros Island (Fig. 1D, after Fitros et al., 2018). The mangan skarns occur adjacent to the Panorama granite-to-microgranite, and to leucogranite apophyses and related pegmatites and aplites Thapsana in Paros (Figs. 1C, D, E). The Thapsana mangan skarn was chosen to develop the model presented in this paper because of its distinct zoning and the manganese mineralization and then applied to the Panorama skarn. This model is based

on the results of a comprehensive study of the geology, mineralogy, paragenesis, geochronology and isotope chemistry of the Thapsana skarn complemented by thermodynamic modeling of the manganese-bearing metasomatic fluids. Using this information, we constrain the physicochemical conditions prevailing during mangan skarn development at Thapsana. A metallogenic model is then proposed for the formation of the Thapsana and Panorama skarns in the context of their spatial and temporal association to their parental leucogranite and peraluminous granite, respectively. The overarching objective of this study is to provide a model that could be employed in exploring manganese skarn prospects and associated deposits in Greece and elsewhere.

2. Geological setting of the Panorama and Thapsana skarns

The Rhodope (RM) and Attico-Cycladic (ACM) Metallogenic Massifs have had a complex geological, magmatic and tectono-metamorphic history, commencing in the Cenozoic. The Rhodope Massif forms the innermost zone of the Hellenic orogen in northern Greece (Kilias, 2021). In contrast, the Panorama Massif in Drama was intruded following the emplacement of Alpine nappes (Fig. 1A): i) The lower Pangaeon Unit (PU) represents a metamorphic dome consisting of orthogneisses, amphibolites and micaceous schists with Permian-to-Carboniferous protoliths, overlain by impure Triassic marbles topped by augen-gneisses, and ii) The middle Sidironero (SU) and upper Kimi (KU) units are composed of a mixture of ortho- and para-gneisses, amphibolites, Paleozoic and Mesozoic dolomitic and calcic marbles, Paleocene-to-Oligocene adakite and calc-alkaline meta-granitoids and sporadic meta-mafic or -ultramafic rocks and -ophiolites. The SU and KU experienced high pressure to ultra-high pressure metamorphism during the early Jurassic and a subsequent high

134 temperature overprint in the late Cretaceous (Moulas et al., 2013). The PU is bordered
135 (to the NE) by the Nestos Suture Zone (NSZ), a ductile, NW-verging thrust zone (Nagel
136 et al., 2011) between the PU and SU, which is of Jurassic-Cretaceous age.

137 The Attico-Cycladic Massif in southern Greece, (Fig. 1B) comprises: i) The
138 Cycladic Basement (CB), an anatectic igneous basement of Hercynian age comprising
139 ortho- and para-gneisses, schists and amphibolites, ii) The Basal Unit (BU) which
140 represents a late Triassic-to-late Cretaceous platform of neritic meta-dolomites and
141 middle Eocene marbles with thin metapelite intercalations overlain by a late Eocene-
142 to-Oligocene metaflysch, iii) The Cycladic Blueschist Unit (CBU) that represents a late
143 Paleozoic-to-Mesozoic continental margin comprising a volcano-sedimentary
144 sequence (Xypolias et al., 2012; Jolivet et al., 2015) and at Paros is composed of
145 intercalated marbles, amphibolites and micaceous schists (Papanikolaou, 1980;
146 Malandri et al., 2016; Laurent et al., 2015), and iv) The structurally higher Upper
147 Cycladic Unit (UCU) comprising Permian to Mesozoic marbles, dismembered
148 ophiolites, late Cretaceous greenschist-to-amphibolite facies and sedimentary rocks
149 (Stouraiti et al., 2017).
150

151 **3. The Panorama and Thapsana granitoids and their contact metamorphic**
152 **aureoles**

153 The Oligocene Panorama pluton intrudes the PU marbles and gneisses, and is
154 composed of two different lithotypes, namely a quartz monzonite laccolith exposed in
155 the north and a granite-to-microgranite apophysis in the south, topped by Quaternary
156 and alluvium sediments (Fig. 1C). The medium-grained, holocrystalline high-K, calc-
157 alkaline quartz monzogranite has been dated at 26.8 ± 0.5 Ma (K-Ar on biotite, Mayer,
158 1968; Jones et al., 1992) and comprises quartz, plagioclase ($An_{\sim 50\text{-}70}$) and alkali feldspar

(orthoclase, $Or_{\sim 70}$). The mafic minerals comprise hornblende (magnesio-hornblende and edenite) and minor biotite and diopside. To a lesser extent, microgranite and granite porphyries are also exposed at Panorama. The granite porphyry consists of alkali feldspars megacrysts ($Or_{\sim 95}$), biotite, and minor spessartine in a groundmass of quartz, alkali feldspar and plagioclase ($An_{\sim 10}$), whereas the microgranite is fine-grained with an aplitic texture and contains ≤ 5 vol. % hornblende and biotite. Apatite, allanite, titanite, zircon and magnetite ± hematite, pyrite, ilmenite and rutile occur as accessory minerals (details in Jones et al., 1992; Ntagkounaki, 1999; Soldatos and Ntagkounaki, 2004; Papaspyrou, 2016).

The Miocene intrusions of Paros are ellipsoidal laccoliths, pipes and apophyses (in the areas of Kolibithres, Kamares, Parikia, Taxiarxes, Logovarda in northern Paros, and Thapsana, Lefkes and Trypiti in central and southern Paros, Fig. 1D). They are classified as porphyritic monzogranites, granites and leucogranites, and have been dated at between 11.5 to 12.4 ± 0.9 Ma and 18.1 ± 0.2 Ma (K-Ar and Rb-Sr on biotite and muscovite respectively, Altherr et al., 1982). The Kolibithres leucogranite was dated by Bargnesi et al. (2013) at 15.5 ± 0.3 to 15.7 ± 0.2 Ma (U-Pb on zircon). The Paros leucogranites comprise quartz, orthoclase, microcline, oligoclase-to-andesine, allanite, zircon, Mg-hornblende, biotite and magnetite. Their peraluminous affinity is displayed by their accessory mineralogy comprising sillimanite, tourmaline, Li-rich muscovite and/or lepidolite, apatite and spessartine (details in McGrath, 1999; Kevrekidis et al., 2015). They are enriched in P, B, F and H_2O (~7 wt. %) and were emplaced at pressures of 1.4 to 4.1 kbar and temperatures of ~660° to ~760°C (Kevrekidis et al., 2015). The Lefkes leucogranite petrographically resembles the Panorama porphyry, whereas the Thapsana leucogranite also contains spessartine.

183 The Panorama and Thapsana granitoids contain dioritic enclaves, and are crosscut
184 by granodioritic, spessartine-tourmaline pegmatites and aplite dikes. They were highly
185 altered by sericitization, kaolinitization and propylitization (Ntagkounaki, 1999;
186 Soldatos and Ntagkounaki, 2004; Kevrekidis et al., 2015). The intrusion of the
187 Panorama and Paros granites and leucogranites produced extensive contact
188 metamorphic aureoles (widths from 100 to 500 m) overprinting the adjacent
189 metamorphic rocks of the PU, and BU and CBU, respectively. At Paros, the hornfelses
190 proximal to meta-bauxites comprise the assemblage sillimanite-kyanite-staurolite-
191 corundum, whereas those of meta-basite and -pelite protoliths contain scapolite-
192 diopside-andradite. More distal from these intrusions, hornblende- and biotite-
193 hornfelses overprinted the PU and CBU lithologies (Papanikolaou, 1980).
194
195 **4. Sampling and analytical methods**
196 Over fifty samples were collected from mine galleries for this study. Six different
197 skarn zones were sampled (i.e., the Rdn, Jhn-Sps and Sps-Cum zones at Thapsana and
198 the Grt-Wo, Grt-Px, Grt-Ep zones at Panorama, ESM Fig. 1A, B) and related Mn-ores
199 and plutonic and host rocks (e.g., marbles, schists and gneisses). We used transmitted-
200 and reflected-light optical microscopy and Scanning Electron Microscopy (SEM) to
201 study the petrography (e.g., mineralogical and textural features) and mineral chemistry
202 of the skarns. Eighteen samples were analyzed for their bulk chemical compositions.
203 These include ten samples from the different intrusive facies, i.e., the Panorama granite
204 and Thapsana leucogranite and eight samples from the different skarn zones. The
205 samples were commercially prepared (using the ES6 code), and then analyzed for their
206 major and trace element contents using ICP-MS and ICP-AES by ActLabs Ancaster,
207 Ontario, Canada.

Fluid inclusions were studied using standard techniques in ≤ 200 mm-thick doubly polished wafers of spessartine (e.g., sample PTS1, cores-to rims, Fig. 2E) from the Jhn-Sps zone of the Thapsana skarn at the Department of Materials Science, University of Patras, Greece. Prior to microthermometric analysis, a subgroup of the fluid inclusions in spessartine were analyzed using Laser Raman spectroscopy at the School of Chemical Engineering, Technical University Athens, Greece. Spectra were treated with the WIRE 3.4 software using the reference catalog of Frezzotti et al. (2012). Additional details of the analytical methodology, probable limitations, and thermodynamic modeling of the physicochemical parameters are reported in ESM Sampling and Analytical Techniques.

Five hundred mg splits of the bulk rock samples of the Panorama granite and Thapsana leucogranite were analysed for their stable and Ca, Mg and Rb/Sr isotope compositions, as well as samples of coarse-grained wollastonite, diopside, grossular and calcite (Panorama), and rhodonite, johannsenite, spessartine and manganoan epidote (Thapsana) from the aforesaid skarn zones. Calcite from the host marble at Panorama and quartz from the gneiss at Thapsana were also analyzed (Table 1). Four granitoid samples from the Panorama granite and Thapsana leucogranite were selected for zircon U-Pb dating (ESM Table 9, Fig. 3 A to C). The isotopic analyses were performed at the Beijing Research Institute of Uranium Geology, China National Nuclear Corporation, the Modern Analysis Center, Nanjing University, Nanjing, China, the State Key Laboratory of Geological Processes and Mineral Resources, and the Chinese Academy of Geological Sciences (CAGS), Beijing, China.

5. Results

5.1. Thapsana and Panorama mangan skarn petrography and paragenesis

The skarns at Panorama and Paros outcrop along the contacts of both the Panorama and Thapsana plutons, their apophyses and aplitic dikes (Figs. 1C, D, 2A, C, ESM Fig. 1A, B). The exoskarns occur as medium-to-coarse grained, granoblastic, structural-controlled lenses, NE- and NW-trending-veins and/or stratabound with irregular forms (with dimensions on 20-meter scale) that are oriented parallel to the foliation of their host rocks. The reserves, at the currently abandoned mines of both Panorama and Thapsana are ≥ 1.5 Mt (based on samples assayed by Paraskevopoulos, 1960; Belardi et al., 2008).

The Panorama exoskarn occurs along the contact of the granite with massive PU calcite marbles that contain dolomite intercalations, or lenses topped by micaceous schists and/or gneisses (Figs. 1C, 2A). Based on field evidence at Panorama, there was an evolution from calcic to mangan exoskarn. Macroscopically, the calcic skarn has two zones (with widths between 5 and 10 m), i.e., a garnet-wollastonite zone (Grt-Wo) adjacent to the PU marble front at the southern contact of the granite, and a later garnet-pyroxene zone (Grt-Px), which is exposed at its northeast contact (Figs. 1C, 2A, ESM Figs. 1A, 2A). The Grt-Wo zone comprises wollastonite (50-60% vol), garnet (20-30% vol), with subordinate pyroxene, plagioclase, calcite, magnetite and locally vesuvianite. The succeeding Grt-Px zone is closer to the Panorama granite-microgranite and composes clinopyroxene, garnet, clinozoisite and scheelite with crystal sizes of ≤ 2 cm (see also Constadinidou et al., 1998; Belardi et al., 2008; Papaspyrou, 2016). At Panorama, the mangan skarn is composed of a garnet-epidote zone (Grt-Ep), a with width of ≤ 30 m, which replaced the latter zones and is located adjacent to the northwestern contact of the Panorama granite. The Grt-Ep zone is enriched in manganese and contains coarse-grained pink epidote, garnet, plagioclase, alkali

feldspar, hornblende, biotite and late-stage, minor pyrite-sphalerite-galena mineralization (Figs. 1C, 2B).

The mangan skarn at Thapsana outcrops along the contacts between apophyses of the muscovite-biotite leucogranite and the BU migmatitized gneisses and the CBU cataclastic marbles intercalated with calcic schists, amphibolites and hornfelses (Fig. 2C, D, ESM Fig. 1A). Skarns are more common, however, where the apophyses intruded the CBU marbles and amphibolites along N- to NNE-trending fault zones. Three metasomatic zones with widths between 10 and 20 m were identified in the Thapsana mine, (Figs. 2C, D, E, F, ESM Fig. 1A). A rhodonite zone (Rdn) comprising rhodonite ± vesuvianite occurs adjacent to the marbles and calcic schists. It passes into a johannsenite-spessartine zone (Jhn-Sps) closer to the Thapsana leucogranite, which. contains subhedral johannsenite and euhedral spessartine ≤ 2 cm in diameter. This zone is associated with Mn^{+2}-Mn^{+3}-oxide ores occurring as massive aggregates, or disseminations (Stage I mineralization). Stage I ore comprises macroscopically subhedral jacobsite ($Mn^{2+}Fe^{3+}{}_2O_4$), hausmannite ($Mn^{2+}Mn^{3+}{}_2O_4$) displaying oriented intergrowths, braunite [$Mn^{2+}Mn^{3+}{}_6(SiO_4)O_8$] and magnetite (with crystals ~2 to 4 cm in diameter) and gangue quartz, albite, rhodochrosite and manganoan epidote. The third, spessartine-cummingtonite zone (Sps-Cum), which is closet to the Thapsana leucogranite, comprises fine- to medium-grained spessartine, hornblende, cummingtonite and phlogopite. This zone is associated with Stage II mineralization, which is dominated by hydrous manganese phases. The manganese minerals occur as massive aggregates in stockworks of E- and WNW-trending veins (with widths ≤ 1.5 m) that display open space filling and boxwork textures. The vein ore assemblage comprises hollandite [$Ba(Mn^{4+}{}_6Mn^{3+}{}_2)O_{16}$], cryptomelane [$K(Mn^{4+}{}_7Mn^{3+})O_{16}$], pyrite and gangue rhodochrosite, calcite and ankerite and supergene pyrolusite ($Mn^{4+}O_2$),

manganite [$Mn^{3+}O(OH)$], vernadite [$(Mn,Fe,Ca,Na)(O,OH)_2 \cdot nH_2O$], manjiroite ($NaMn_8O_{16}$), and Fe-oxides/hydroxides (Fig. 2C, D, ESM Figs. 1B, 2B, see Fitros et al., 2018).

5.2. Skarn and ore mineral chemistry

Garnet from the Grt-Ep zone of the Panorama mangan skarn forms euhedral, isotropic crystals up to 3.5 cm in diameter or is intergrown with epidote and calcite (Fig. 3A). In the Grt-Wo and Grt-Px zones of the calcic skarn, the garnet crystals are ≤ 0.1 mm in diameter and co-precipitated with fibrous wollastonite (≤ 2.5 mm in diameter, $Wo_{\sim 98.5}$) and/or anhedral pyroxene ($Wo_{\sim 50}$, and $Di_{\sim 50}$, respectively, Fig. 3C, ESM Tables 1, 2). They display isotropic cores and oscillatory zoned rims with sector-interpolysynthetic-twinning and chaotic birefringence, and contain inclusions of vesuvianite (Mn = 0.29-0.98, in apfu). There is a progressive trend of Grs and Sps enrichment towards the rims of crystals (e.g., cores-to-rims: $Grs_{\sim 55-65}Adr_{\sim 25-35}Sps_{\sim 5-10}$ to $Grs_{\sim 60-80}Ard_{\sim 15-30}Sps_{\geq 10}$, Grt-Ep; $Grs_{\sim 90-95}Sps_{\sim 5-10}$ to $Grs_{\sim 80-85}Sps_{\sim 10-20}$, Grt-Px and $Grs_{\sim 50}Adr_{\sim 50}Sps_{\sim 1.5}$ and $Grs_{\sim 25-30}Adr_{\sim 65-70}Sps_{\sim 2}$, Grt-Wo zones, respectively, Fig. 3D). Garnet from the Panorama granite is spessartine-almandine in composition (ESM Table 3). The pyroxene close to the granite contact, i.e., in the Grt-Px zone is diopside-to-hedenbergite in composition ($Di_{\sim 45-55}$, Mn substituted for Ca ≥ 0.11 apfu, Fig. 3C, ESM Table 2). Its crystals are intergrown with subhedral clinozoisite (pistacite component P_s% ~1), scheelite, plagioclase ($An_{\sim 50}$) and orthoclase ($Or_{\sim 90}$) and are ≤ 0.2 mm in diameter (ESM Table 4a, b, Bargnesi et al., 2013). In the Grt-Ep zone, epidote-group minerals fill the interstices between plagioclase, hornblende (magnesio-hornblende, ≤ 0.2 mm in diameter, ESM Table 5) and in the Grt-Px zone between pyroxene crystals. The epidote-group assemblage comprises anhedral orthoclase, epidote (~15 vol. %),

307 zoned allanite (~25 vol. % for the cores and ~35 for the rims, containing La, Ce and Nd
308 ≥ 0.23, 0.24 and 0.08 in apfu, respectively, Mn substituting for Ca and Fe ≥ 0.24 apfu,
309 ESM Table 6), and minor rhodochrosite.

310 Rhodonite (with ~7.4 apfu Mn) from the Thapsana mangan skarn occurs in massive
311 aggregates or fills joints with prismatic crystals (up to ~1 cm in diameter) that are
312 intergrown with fine-grained vesuvianite. Clinopyroxene from the Jhn-Sps zone is
313 euhedral, coarse-grained and zoned. It is characterized by cores with elevated
314 manganese contents (e.g., Mn ≥ 0.9 in apfu, Fig. 3C). The cores are composed of
315 johannsenite ($Jhn_{\sim 80\text{-}90}Di_{\sim \leq 13}$) and the rims vary from johannsenite to diopside in
316 composition ($Jhn_{\sim 60\text{-}70}Di_{\sim \leq 30}$). Garnet is present in both the Jhn-Sps and Sps-Cum
317 zones. It is isotropic, homogeneous (core-to-rim) and intergrown with johannsenite and
318 cummingtonite. Their composition in the Jhn-Sps zone is $Sps_{\sim 80\text{-}85}Adr_{\leq 10}$, whereas in
319 the Sps-Cum zone it is $Sps_{\sim 75\text{-}80}Grs_{\leq 15}$ (Fig. 3D). The Stage I manganese ore assemblage
320 comprises braunite ($Mn^{+3} \approx 6.1$ apfu), hausmannite ($Mn^{2+}/Mn^{3+} = 0.46$), jacobsite
321 ($Mn^{2+}/Fe^{3+} = 0.58\text{-}0.78$), Mn-magnetite (Mn = 0.2) and ilmenite (Mn = 0.03, ESM
322 Table 7). These minerals were replaced, particularly around their rims and along
323 cleavage planes, by hypidiomorphic magnesio-mangani-hornblende, which grades into
324 manganoan cummingtonite (with ≤ Mn^{3+} 0.6 apfu), epidote (P_s% ~9 to 11, Mn^{3+} ~2.40
325 apfu), plagioclase ($An_{\sim 55\text{-}60}$, Mn ≤ 0.26 apfu), orthoclase ($Or_{\sim 85\text{-}90}$, Mn ≤ 0.05 apfu),
326 quartz, phlogopite (with Mn^{2+} ≤ 0.2 apfu), hydroxylapatite, johnbaumite and
327 manganoan calcite (ESM 1, Tables 4a, b, 5, 6).

328

329 *5.3. Geochemistry of the plutons and skarns and tectonic setting*

330 The rocks of the plutons at Panorama, Thapsana and other locations in the ACM
331 (e.g., Ikaria, Naxos and Tinos) are mostly granites and leucogranites with elevated SiO_2

contents (e.g., av. of ~71 wt. %, st.d. of 4.0 wt. %, Fig. 4A). The SiO_2 contents of the skarns are lower (e.g., av. of ~34 wt. %, st.d. of ~0.7 wt. %) and their MnO content is much higher (e.g., av. of ~0.07 wt. %, st.d. of 0.03 wt. % versus av. of ~16 wt. %, st.d. of 1.0 wt. % and Mn/Fe of av. of ~0.05, st.d. of 0.05 versus av. of ~5.2, st.d. of 6.5, ESM 1, Table 8). The mangan skarns are most probably related to the reduced (or least oxidized, ilmenite-bearing) lithotypes of the Panorama and Thapsana granitoids (Fig. 4B; after Meinert et al., 2005). Additionally, these plutons display an evolutionary trend from metaluminous-to-peraluminous affinity, possibly depicting the alkali loss content (e.g., K/Rb = ~190 to 340, ESM 1, Table 8) during assimilation of a crustal component (Fig. 4C). From the log(Mn/Fe) versus log(Al/Ca) (Fig. 4D) plot it is evident that there was an evolution towards higher manganese contents during skarn formation. Furthermore, the manganese content of the leucogranites overlaps with that of the BU host rocks, i.e., ortho- and para-gneisses at Paros, Naxos and Ikaria, suggesting a close geochemical association and possible assimilation of manganese from the host lithologies (see also Pe-Piper, 2000; Stouraiti et al., 2010). It is also possible that the lower manganese contents of the Panorama skarn (e.g., Mn/Fe = 0.4 to 2.6 versus 3.6 to 18.5) represents a transitional between the mangan and calcic skarns (Fig. 4D). The granites and leucogranites were emplaced in a Syn-Collisional/Volcanic Arc tectonic setting (Syn-COLG and VAG, Fig. 4E).

The total REE content of the granites/leucogranites and skarns is relatively low, up to ~86 ppm. Chondrite-normalized REE profiles for these granitoids and related mangan skarns are essentially sub-parallel with concave-upward shapes, weak negative slopes for the LREE and horizontal HREE segments (Fig. 4G, ΣLREE/ΣHREE = 2.3 to 11.3). These trends reflect the mild enrichment of LREE to MREE (e.g., $0.34 \leq La_N/Sm_N \leq 2.93$) and HREE ($0.96 \leq La_N/Yb_N \leq 10.77$) (ESM 1, Table 8). The profiles

357 also display negative Eu-anomalies (e.g., ≤ ~0.4), however, their Ce-anomalies are
358 variable (ranging from ~0.5 to 0.9 for Panorama and from 0.4 to 1.3 for Thapsana, Fig.
359 4G, ESM 1, Table 8). We propose that the petrochemical features for the mangan skarns
360 indicate that the peraluminous granitoids were one of the sources for the manganese in
361 the skarn-forming fluid. The second source was the surrounding PU, and BU and CBU
362 rocks (Fig. 4B to G).
363
364 *5.4. Fluid inclusion petrography, microthermometry and Raman analysis*
365 Fluid inclusions were studied in spessartine crystals of the Jhn-Sps zone of the
366 Thapsana mangan skarn (Table 1a). This zone was selected because of its almost ideal
367 zoning and spessartine was selected as the host for the inclusions because it represents
368 the major manganoan skarn mineral at Thapsana. The fluid inclusions are mostly ≤ 20
369 μm in diameter but some are up to 80 μm in diameter and they vary in shape from
370 irregular to ellipsoidal; some have negative crystal shapes. They occur along healed
371 fractures or grain boundaries, as clusters and linear arrays in microcracks during the
372 development of the garnet crystals were considered pseudosecondary, whilst those that
373 intercept the crystal boundaries were interpreted as secondary. Only primary inclusions
374 were selected in our microthermometric study. A number of these inclusions show
375 evidence of decrepitation, necking and leakage. Necking is manifested in series of
376 almost empty primary fluid inclusions that occur in planar arrays. Examples of
377 representative FIAs are shown in Figure 5A to D.
378 Fluid inclusions were classified based on phase relationships observed at room
379 temperature (Fig. 5 A to D). Three types of fluid inclusions were recognized:
380 (i) Type I: Aqueous liquid inclusions that contain ≥ 80 vol. % liquid (L-V),

(ii) Type II: Vapor-rich aqueous inclusions (V-L) which homogenize to vapor and contain ~50 to 70 vol. % vapor and CO_2, as well as inclusions comprising ≥ 20 to ≤ 70 vol. % vapor, and

(iii) Type III: Solid-bearing polyphase inclusions (S-L-V, in which the vapor bubble occupies ≤ 40 vol. %).

The S-L-V inclusions, based on their optical properties contain rhodochrosite (S_1, Fig. 5C) with rhombohedral and antarcticite (S_2, $CaCl_2 \cdot 6H_2O$) with rounded crystals, Mn-chlorides (S_3) and calcite (S_4), in addition to halite. From these solids rhodochrosite and antarcticite display consistent volume ratios in the inclusions in respect to the other phases and they were as daughter mineral. Other solids were interpreted as accidentally trapped solids (Fig. 5A to D). The L-V and S-L-V inclusions homogenize to liquid upon heating. The coexistence of L-V and V-L inclusions suggests heterogeneous trapping and fluid immiscibility. Thre temperatures of initial ice melting (T_e) of the L-V and V-L inclusions range from -56° to -20°C suggesting the presence of $MnCl_2 \pm CaCl_2$ in addition to NaCl. Final ice melting temperatures for these inclusions range from -48.2° to -2.5°C (Table 1a).

There are no available data for the ternary system H_2O-NaCl-$MnCl_2$ (see Robelin et al., 2004a, b), and further experimental work should be done for this system. We used the AQSO2c, AQSO3e and Loner 32 software (Bakker, 2003) for the ternary system H_2O-NaCl-$CaCl_2$ due to the presence of antarcticite and its possible similarity to the ternary system H_2O-NaCl-$MnCl_2$. The corresponding salinities range from ~3.0 to ~48.0 wt. % NaCl equiv (Fig. 5E, F, Table 1a). The L-V, V-L and S-L-V fluid inclusions in spessartine homogenize to liquid and vapor between 305° and 565°C (Fig. 5E, F, Table 1a). The L-V, V-L and S-L-V fluid inclusions in spessartine homogenize to liquid and vapor between 305° and 565°C (av. of ~435ºC, st.d. of 67), 305º to 565ºC

406 for the cores and 320º to 470ºC for the rims). Fluid densities of the inclusions range
407 from 0.53 to 0.91 g/cm^3 and trapping pressures from ~80 to ~150 MPa (av. of ~110
408 MPa, st.d. of 1.8), ~80 to ~150 MPa for the cores and ~70 to ~120 MPa for the rims
409 (Fig. 5E, F, Table 1a).

410 Laser Raman spectroscopic analyses were conducted on ten L-V, V-L and S-L-V
411 fluid inclusions hosted in spessartine. The results of the Raman analyses show that the
412 vapor contains CO_2 and traces of N_2 and H_2 (~5.6 to ~12.3 CO_2, in mol fraction %,
413 Table 1b). Raman spectra and solubility calculations of the liquid phase indicated that
414 CO_3^{2-} (~5010 ppm), Cl^- (~4390 ppm) and HCO_3^- were the dominant anions in solution,
415 although F^- and SO_4^{2-} were also present. The dominant cations in the skarn-forming
416 fluid were Mn^{2+} and Mn^{3+} (total of ~4390 ppm) and Si^{4+}, although Na^+, K^+, Mg^{2+}, Ca^{2+}
417 and Pb^{+2} and traces of Fe^{2+}, Ba^{2+}, B^{3+} and Li^{2+} were detected (Table 1b).

418

419 *5.5. Independent estimation of physicochemical parameters*

420 The pressure at the time of formation of the Panorama and Thapsana mangan skarns
421 and the associated granites was estimated using the Al-in-hornblende- and ^{T}Al biotite-
422 geobarometers. This pressure is estimated to have been between 100 and 190 MPa for
423 the skarns (estimated for the Panorama Grt-Px zone and Thapsana Sps-Cum), and ~
424 300 Mpa for the granites. Temperatures were determined from Raman analyses of the
425 gaseous and liquid phase of fluid inclusions employing the CO_2- and Na-K-, Na-K-Ca-
426 and K-Mg-geothermometers, the johannsenite-spessartine and spessartine-epidote
427 isotopic pairs (Jhn-Sps and Sps-Cum zones, respectively), and the garnet-
428 clinopyroxene, garnet-biotite and two-feldspar geothermometers. The temperatures
429 obtained ranged between ~330º and ~525ºC. Accessory spessartine from the
430 peraluminous granites-to-leucogranites in the ACM yielded temperatures of ~585º for

Parorama and ~670ºC for Paros. Independent calculation of the skarn-forming fluid salinity was based on solubility Raman data using the method of Wang and Wang (2011). The calculated salinities range between 27.7 and 42.9 wt. % NaCl equiv, with a standard error of ± 2.8%. Details about the application, limitations and assumptions of the various geothermo-oxygen-barometers are given in Tables 1b, 2, ESM Tables 2, 3, 4b, 5 and 6.

5.6. Stable isotopes

Stable isotope compositions including those of oxygen, hydrogen, carbon, calcium and magnesium were determined for the Panorama and Thapsana granite-to-leucogranite and their host rocks, i.e., the marbles at Panorama and the gneisses at Thapsana (Table 2). For the Panorama granite, the $\delta^{18}O_{V\text{-}SMOW}$ and δD values range between +9.3 and +11.2 per mil and -58 and -75 per mil, respectively. The calculated $\delta^{18}O_{H2O}$ values of the metasomatic fluid range from +3.7 to +7.7 per mil (Fig. 6A). The $\delta^{44}Ca_{BSE}$ and $\delta^{26}Mg_{DSM\text{-}3}$ isotopic compositions are +1.3 and -0.2 per mil, respectively (Fig. 6B). For the host marbles, the measured $\delta^{18}O_{V\text{-}SMOW}$, δD, $\delta^{44}Ca_{BSE}$, $\delta^{26}Mg_{DSM\text{-}3}$ and $\delta^{13}C_{V\text{-}PDB}$ values are +16.3, -42, +0.3, -0.6 and -2.2 (on calcite) per mil respectively. For the Panorama skarn minerals the $\delta^{18}O_{V\text{-}SMOW}$ and δD values lay between those of the leucogranite and the PU marbles (e.g., +8.5 and +14.6 and -67 and -71 per mil). The calculated $\delta^{18}O_{H2O}$ values of the skarn-forming fluid range from +10.4 to +11.9 per mil (Fig. 6A). The same trend occurs for the $\delta^{44}Ca_{BSE}$ and $\delta^{26}Mg_{DSM\text{-}3}$ values (e.g., +0.5 to +0.8 and -1.3 to -1.7), although these are plotted closer to the Panorama granite (Fig. 6B).

For the Thapsana leucogranite, the $\delta^{18}O_{V\text{-}SMOW}$ and δD values range between +9.8 and +10.5 per mil and -82 and -64 per mil. The $\delta^{18}O_{H2O}$ values of the metasomatic fluid

456 range from +8.0 to +10.5 per mil (Fig. 6A). The $\delta^{44}Ca_{BSE}$ and $\delta^{26}Mg_{DSM-3}$ isotopic
457 compositions are +1.6 and -0.2 per mil, respectively (Fig. 6B). For the BU gneisses, the
458 measured $\delta^{18}O_{V-SMOW}$, δD, $\delta^{44}Ca_{BSE}$ and $\delta^{26}Mg_{DSM-3}$ values on quartz are +17.4, -48,
459 +0.5 and -0.6 per mil respectively (Fig. 6B). For the Thapsana skarn minerals the $\delta^{18}O_{V-SMOW}$ and δD values are also between those of Thapsana leucogranite and the BU
461 gneisses (e.g., +8.3 and +12.5 and -80 and -42 per mil). The $\delta^{18}O_{H2O}$ values of the skarn-
462 forming fluid are approximately 3.0 per mil higher (e.g., +11.2 to +13.6 per mil, Fig.
463 6A), and plot closer to the gneisses. The same pattern is obtained for the $\delta^{44}Ca_{BSE}$
464 $\delta^{26}Mg_{DSM-3}$ isotopic compositions (i.e., +0.6 to +1.1 and -1.4 to -1.9 per mil,
465 respectively, Fig. 6B). The measured $\delta^{18}O_{V-SMOW}$, δD, $\delta^{44}Ca_{BSE}$ and $\delta^{26}Mg_{DSM-3}$ values
466 of stage-I jacobsite are +7.2, -83, +1.6 and -1.1 per mil, respectively (Fig. 6B). The
467 $\delta^{18}O_{H2O}$ value of the ore-forming fluid is +10.0 per mil (Fig. 6A). The above calculated
468 $\delta^{18}O_{H2O}$ and measured δD, $\delta^{44}Ca_{BSE}$ and $\delta^{26}Mg_{DSM-3}$ values suggest the peraluminous
469 Panorama granite and Thapsana leucogranite, as one of the sources for the mangan
470 metasomatic fluids. The skarn-forming fluids have also interacted and isotopically
471 equilibrated to various degrees with the host PU marbles (Panorama), and BU gneisses
472 (Thapsana) (Figs. 6A, B) thus providing isotopic skarn signatures between the
473 endmembers, i.e., peraluminous granitoids and host rocks.
474
475 *5.7. Radiogenic isotopes*
476 Analyses of the Rb-Sr and U-Pb isotope ratios were performed on the Panorama and
477 Thapsana mangan skarns to determine their temporal evolution and origin. The $^{87}Sr/^{86}Sr$
478 values for the Panorama granite and host marbles, range between 0.7134 and 0.7144
479 and 0.7169, respectively. Their initial $^{87}Sr/^{86}Sr_{(i)}$ values range from 0.7116 to 0.7127
480 and 0.7131 (Fig. 6C, Table 2). Those ($^{87}Sr/^{86}Sr$ and $^{87}Sr/^{86}Sr_{(i)}$) for the Panorama skarn

481 zones are between those from the Panorama granite and the PU marbles (i.e.., 0.7128
482 to 0.7145 and 0.7111 and 0.7128, respectively, assuming an age of 26.8 ± 0.5 after
483 Mayer, 1968, Fig. 6C, Table 2). This implies interaction between the Panorama granite-
484 derived fluids and the PU marbles during skarn formation. Isochron, Rb-Sr dating of
485 the Panorama granite and mangan skarn yielded ages of 25.79 ± 0.24 Ma (MSWD =
486 0.93) and 24.92 ± 0.22 Ma (MSWD = 0.89) respectively (Table 2, ESM Fig. 3A).
487 The $^{87}Sr/^{86}Sr$ and $^{87}Sr/^{86}Sr_{(i)}$ values for the Thapsana leucogranite and its host
488 gneisses, are higher than those of the Panorama granite (e.g., between 0.7149 and
489 0.7156, and 0.7176, and 0.7144 and 0.7152, and 0.7171, respectively, Fig. 6C, Table
490 2). The $^{87}Sr/^{86}Sr$ and $^{87}Sr/^{86}Sr_{(i)}$ isotopic compositions for the Thapsana mangan skarn
491 plot between those from Thapsana leucogranite and host BU gneisses (i.e., 0.7149 to
492 0.7169 and 0.7146 to 0.7165, using an age of 7.5 ± 0.6 Ma after Bargnesi et al., 2013,
493 Fig. 6C, Table 2) also suggesting possible interaction during skarn formation. Jacobsite
494 from Stage I manganese ore displays even higher $^{87}Sr/^{86}Sr$ and $^{87}Sr/^{86}Sr_{(i)}$ values (i.e.,
495 0.7176 and 0.7171, Fig. 6C, Table 2). The Rb-Sr isochron for the Thapsana leucogranite
496 and mangan skarn yielded ages of 7.38 ± 0.13 Ma (MSWD = 0.96), 6.29 ± 0.12 Ma
497 (MSWD = 1.09, Jhn-Sps zone) and 6.11 ± 0.15 Ma (MSWD = 1.17, Sps-Cum zone)
498 (ESM Fig. 3B).
499 Uranium-lead isotopic ages were obtained for zircon crystals from the Panorama
500 granite and the Panorama Grt-Ep and Thapsana Sps-Cum zones. The zircon crystals are
501 mostly colorless, small-to-medium-sized (≤ 1 mm), euhedral and zoned (ESM Fig. 3C).
502 They have low U and Th contents and high Th/U ratios (i.e., 9 to 55, 3 to 37 ppm, and
503 0.40 to 0.88, ESM 1 Table 9). Data regression (with a 90% confidence level) yielded a
504 weighted mean age of 26.03 ± 0.24 (MSWD = 1.07, n = 4) for the Panorama granite.
505 The ages for the mangan skarns are 24.76 ± 0.25 (Panorama, Grt-Ep zone, MSWD =

506 0.89, n = 5) and 5.97 ± 0.26 (Thapsana, Sps-Cum zone, MSWD = 0.96, n = 5) (ESM
507 Table 9, Fig. 3C). Our chronological data suggest that the mangan skarns formed within
508 1.0 Ma of the emplacement of the peraluminous granitoids.
509
510 **6. Modeling of mangan skarn formation**
511 *6.1. Physicochemical conditions*
512 Phase equilibria in the system CaO-MnO-Al_2O_3-SiO_2-H_2O-CO_2 were used to
513 estimate the stability conditions of the mangan skarn assemblages. We constructed
514 temperature versus logfO_2 and logX_{CO2} versus temperature plots for temperatures of
515 550º, 500º and 380ºC and a pressure of ~150 MPa (Fig. 6D, E,), using the
516 thermodynamic data (ESM Tables 10a, b) of the Geo-Calc (Berman, 1988) and
517 SUPCRT92 software (Johnson et al., 1992, with the extended database of Zimmer et
518 al., 2016). Details regarding the estimation of the physicochemical parameters and
519 related reactions (reactions 1 to 32) during the mangan skarn-formation are given in
520 ESM Tables 10a, b.
521 Deposition of quartz (reactions 1, 9 and 16) occurred at log$\alpha_{SiO2(aq)}$ values ranging
522 between -3.5 and -1.1 (ESM Table 10a). For temperatures of 550º, 500º and 380ºC, the
523 logfO_2 values of the skarn-forming fluid ranged from HM+6.2 to HM-7.8 (e.g.,
524 reactions 3, 4, 6, 8, 10, 12, 13, 15, 18, 20 and 22, ESM Table 10a). The relatively more
525 oxidized Rdn zone is due to oxidation and decarbonation of the CBU marbles and/or
526 the BU gneisses (Abs-Wurmbach and Peters, 1999), while the relatively more reduced
527 are the Sps-Cum and Grt-Ep zones (Fig. 6D, ESM Table 10a). Based on the equation
528 of Zen (1985), the calculated logfO_2 values of the residual melts of the above discussed
529 peraluminous granitoids range between HM-4.9 and HM-2.0 (for Ikaria, Tinos and
530 Naxos), whereas for Panorama and Paros they are HM-3.9 and HM-3.3 (where HM is

531 the Hematite-Magnetite buffer, Fig. 6D, ESM Table 10a), implying a reduced (to
532 slightly oxidizing) redox state of some of these peraluminous magmas. Moreover, the
533 $\log X_{CO2}$ values, in both skarns, range from -3.5 to -0.7 (e.g., reactions 2, 5, 7, 10, 11,
534 14, 17, 19, Fig. 6E, ESM Table 10a). The highest $\log X_{CO2}$ values are for the Rdn zone
535 and the lowest for the Sps-Cum zone (Fig. 6E, ESM Table 10a).
536
537 *6.2. Thermodynamic modeling*
538 Manganese is a mobile transitional metal which tends to concentrate in the liquid
539 phase of the metasomatic fluids as chloride complexes in two oxidation states, i.e., Mn^{+2}
540 and Mn^{+3} (Uchida et al., 2003), and its mobility and solubility are dominantly controlled
541 by temperature, pH and oxidation potential of the skarn-forming fluid. Thermodynamic
542 modeling was carried out using the program React included in Geochemist's
543 Workbench® software (Bethke, 1998; Bethke and Yeakel, 2016) using the FreeGs and
544 SUPCRT92 databases (Bastrakov, 2004; Zimmer et al., 2016) for the aqueous and
545 gaseous phases and manganoan-silicates and -carbonates. The thermodynamic datasets
546 were for temperatures of 550º, 500º and 380ºC (using microthermometrical data, Table
547 1a) and a pressure of 150 MPa. Individual ion activity coefficients of dissolved species
548 were calculated using the B-gamma extension of Helgeson et al. (1981) and Henley et
549 al. (1984) for an ionic strength (I) of 0.35.
550 The Thapsana and Panorama (although we have modeled only the Grt-Ep zone)
551 skarn-forming fluid was considered as a dilute aqueous solution and all Mn-bearing
552 minerals to have end member compositions. The initial composition of the fluid is
553 reported in ESM Table 10a. The thermodynamic data in ESM Tables 10a, b were
554 obtained from the experimental data of Baker et al. (2004) and Tian et al. (2014). We
555 have used this skarn-forming fluid composition to ensure that ≥ 95 vol. % of the

precipitated mineral assemblages are manganoan, corresponding to the assemblages observed in the Thapsana, and partly in the Panorama mangan skarns. The $\log[\alpha_{Mn}{}^{2+}/(\alpha_{H}{}^{+})^2]$ and $\log[\alpha_{Mn}{}^{3+}/(\alpha_{H}{}^{+})^3]$ values of the metasomatic fluid as a function of temperature, were modelled using reactions 23 to 32 listed in ESM Table 10b.

Our model evaluates the effect of a temperature drop from 600° to 250°C through a series of 50°C steps, with equilibrium attained in each step. It also evaluates the reaction of the metasomatic fluid with the host marble and gneiss and represents a titration, in which 100 g of host rock (gneiss or marble) is progressively added to the initial skarn-forming fluid. For our simulation we used 1000 g of gneiss and/or marble reacting with ~1056 g of the mangan metasomatic fluid. The Panorama PU marble is composed of 90 vol. % calcite-dolomite, 5 vol. % quartz and 5 vol. % muscovite and 0.02 wt. % MnO (Soldatos and Ntagkounaki, 2004), whereas the Thapsana BU gneiss comprises 30 vol. % quartz, 30 vol. % alkali feldspar, 20 vol. % plagioclase, 10 vol. % biotite, 5 vol. % calcite and 5 vol. % muscovite and 0.06 w.t. % MnO (Pe-Piper, 2000; Stouraiti et al., 2010).

In our simulation, which involved concurrent cooling and reaction of the skarn-forming fluid with gneiss or marble, the mangan skarn assemblages predicted to form are: (i) Rhodonite, ± tephroite, and spessartine (T ≈ 550ºC), (ii) Spessartine, diopside, johannsenite and cummingtonite (T ≈ 500ºC) and (iii) Piemontite, spessartine, cummingtonite and phlogopite (T ≈ 380ºC). Quartz, calcite and rhodochrosite, as well as minor pyroxmangite, jacobsite, bixbyite and braunite, hausmannite, magnetite and grossular (T ≈ 550º to 500ºC) and pyrolusite (T ≈ 380ºC) were also predicted to form. As temperature drops from T ≈ 600º to 550ºC only the anhydrous manganoan silicates, i.e., rhodonite ± tephroite crystallise. Spessartine and johannsenite were the major minerals to be deposited from ~550º to ~380ºC and ~500º to ~400ºC, respectively. At

581 temperatures lower than 400ºC, hydrous manganoan minerals precipitate. Below T ≈
582 400ºC and as additional amount of the host rock reacts with the metasomatic fluid,
583 garnet (spessartine and grossular) and pyroxene (johannsenite and diopside) were
584 consumed and replaced by piemontite, or manganoan epidote, phlogopite, quartz,
585 calcite and rhodochrosite. The oxides bixbyite, jacobsite and braunite were the first
586 minerals to precipitate, followed by magnetite and hausmannite and then pyrolusite
587 (Fig. 7A).

588 Changes in the composition of the mangan metasomatic fluid, as temperature drops,
589 comprise an increase of the $\log\alpha_{SiO2(aq)}$ values (e.g., from -3.5 to -1.1, Fig. 7B). The
590 $\log fO_2$ values of the skarn-forming fluid in the Rdn (± Tep) zone remained roughly
591 constant at T = 550º and 500ºC and then decreased at T = 380ºC (Fig. 7B). For all the
592 other zones the $\log fO_2$ values decreased from T = 550º and down to 380ºC (Fig. 5E, F,
593 G), as the metasomatic fluid becomes more reducing due to wall-rock interaction with
594 the marbles and gneisses (Figs. 5G, 6A, B, C). The precipitation of manganoan-
595 silicates, -carbonates and -oxides was also promoted by increase of pH (e.g., from pH
596 = 3.5 to 5.5, Fig. 7B). pH neutralization of the skarn-forming fluid was more intense
597 for the cumulative reaction of ~20% of the total mass of the host rock (from ~3.5 to
598 ~4.7). At the same time the $\log fO_2$ values decreased by ~1 order of magnitude due to
599 ongoing buffering (Fig. 7B). A sudden drop of the $Mn^{2+}_{(aq)}$ content is recorded for the
600 same cumulative reaction of ~20% of the host rock with the metasomatic fluid. The
601 $Mn^{3+}_{(aq)}$, $Ca^{2+}_{(aq)}$ and $\Sigma Fe_{(aq)}$ contents were decreased substantially for a cumulative
602 reaction of ≥ ~80% of the total mass of the host rock. The $\log X_{CO2}$ values decreased
603 from -0.6 to -4.0, and their reduction was more intense for a cumulative reaction of ≥
604 ~70% of the total mass of the host rock. The chlorinity of the metasomatic fluid has
605 increased in this interval (Fig. 7C).

606 Buffering was accomplished when the carbonates, i.e., calcite and rhodochrosite
607 were equilibrated with the metasomatic fluid, and possibly after the oxidation of Mn^{2+}
608 and Mn^{3+} to Mn^{4+}. At these conditions the skarn-forming fluid was depleted by ≤ 5
609 orders of magnitude in iron, calcium and manganese. Moreover, piemontite continues
610 to precipitate (Fig. 7B, C). At temperatures below 380ºC a decrease of the manganese
611 content was caused due to the precipitation of piemontite and pyrolusite (Fig. 7A, C).
612 The $\log[\alpha_{Mn}{}^{2+}/(\alpha_{H}{}^{+})^2]$ values were decreased from 7.2 to 1.6. With decreasing
613 $\log[\alpha_{Mn}{}^{2+}/(\alpha_{H}{}^{+})^2]$ values the anhydrous manganoan silicates (e.g., rhodonite ± tephroite,
614 spessartine and johannsenite) become unstable, as their stability fields are reduced in
615 size in respect to the hydrous manganoan silicates (e.g., cummingtonite and phlogopite)
616 and so they were replaced by the latter. The $\log[\alpha_{Mn}{}^{3+}/(\alpha_{H}{}^{+})^3]$ values during the
617 deposition of piemontite, or manganoan epidote were ranging between 2.7 and 4.8 (Fig.
618 7D) and increased at T ≤ 380ºC. At these $\log[\alpha_{Mn}{}^{3+}/(\alpha_{H}{}^{+})^3]$ values the majority of all
619 the mangan skarn minerals are progressively replaced by piemontite, or manganoan
620 epidote, as its stability field was enlarged (Fig. 7D). Precipitation of the above minerals
621 was provoked by the removal of Mn^{+2} from the mangan skarn-forming fluid and its
622 incorporation in Mn^{+2}-silicates; favoring its precipitation due to the enrichment of Mn^{+3}
623 and Mn^{4+} in the residual solution.

624 Our simulation of the manganese-enriched metasomatic fluid through fluid-rock
625 interaction and simple cooling predicts the relative abundance of the assemblages
626 observed at Thapsana and Panorama mangan skarns, although tephroite, pyroxmangite
627 and bixbyite are absent. It is suggested that fluid-rock interaction and simple cooling as
628 precipitation mechanisms produce a mangan skarn paragenesis that evolves from early
629 anhydrous manganoan silicates and Mn^{2+}-oxides/hydroxides (Fig. 7A, C, e.g.,

630 rhodonite, spessartine, johannsenite, jacobsite, ± tephroite and pyroxmangite, T ≈
631 550ºC) to later hydrous manganoan silicates and oxides and/or carbonates (Fig. 6A,
632 e.g., cummingtonite, T ≈ 500ºC and piemontite ± phlogopite, T ≈ 380ºC). Our modeling
633 suggests that the primary parameters that control the solubility of manganoan minerals
634 precipitated from the metasomatic fluid due to the simple cooling and fluid-rock
635 interaction were: (i) The variation of pH and logfO_2 values which is more intense at
636 lower pH values, (ii) Reducing conditions (Figs. 3I, K, 5G) in which oxidation of
637 manganese did occur (ESM Table 10a, reaction 13), and (iii) The manganese redox
638 state, i.e., Mn (II)- versus Mn (III)-chlorine ligands (Fig. 7 C, D).

639 **7. Discussion**

640 *7.1. Conditions and mechanisms of mangan skarn formation and source of*
641 *manganese*

642 Our results indicate that there is a decrease in the Grs and Jhn components (core-to-
643 rims, garnets and pyroxenes, Grt-Px and Grt-Ep zones, respectively) at Panorama
644 coupled with an increase of the Sps component (garnets, Grt-Px zone). For Thapsana,
645 they indicate there is an increase of the Jhn component of pyroxene of the Sps-Jhn zone
646 (Fig. 3I, K). These compositional changes most likely reflect fluctuations of the
647 chemistry, i.e., manganese and calcium contents and oxidation state of the skarn-
648 forming fluid during mangan skarn formation. The changes of the Grs and Jhn
649 components, as well as the deposition of jacobsite, hausmannite, braunite and magnetite
650 (stage I, Thapsana) are attributed to the oxidation of manganese from Mn^{+2} to Mn^{+3}
651 (Zaw and Singoui, 2000). Additionally, they may reflect a decrease in the availability
652 of Mn^{+2} in the metasomatic fluid, as the mangan skarn evolved (from T ~550º to
653 ~380ºC), or partitioning of calcium (± magnesium) and manganese between

manganoan garnets and epidote and/or pyroxene during their growth resulting in variations of the calcium and manganese content of the metasomatic fluid. These fluctuations may have also provoked the formation of manganoan epidote in Panorama and cummingtonite in Thapsana mangan skarns. At Thapsana, as temperature dropped, deposition of late Stage II hydrous manganese oxides of was favored, demonstrating the gradual evolution of skarn-forming fluids towards near-neutral and reducing conditions (Brookins, 1988).

Fluid inclusion data for spessartine from the intermediate Jhn-Sps zone of the Thapsana mangan skarn provides crucial information regarding the development and evolution of the Mn-ore-forming fluids. In particular, early stage skarn zoning and spessartine deposition occurred due to boiling, and changes of the metal solubility, redox state and chlorinity/carbonate ratio of hydrothermal fluids at temperatures between ~400° and ~550°C and pressure ~100 to ~190 MPa (Fig. 5E, F, G), mainly due to low lithostatic pressure of magma emplacement (e.g., ~300 MPa). As the system evolved, mixing of fluids, wall-rock interaction, buffering and cooling (temperatures ranging between 350° and 450°C) were the major parameters controlling the evolution of mangan skarn zones and ore formation (e.g., Stage I).

We have only indirect isotopic evidence for the source of the manganese. For the Thapsana skarn system, manganese was the predominant cation of the ore-forming fluids (up to 4390 ppm, Table 1a). From the hydrogen versus oxygen isotope plot (Fig. 6A) it is evident that most of the $\delta^{18}O_{H2O}$ and δD values of Thapsana peraluminous granitoid (as well as Tinos, Ikaria and Naxos) and the mangan skarn-forming fluids are genetically associated. A trend towards higher $\delta^{18}O_{H2O}$ values with nearly equal δD values as temperature dropped from 480º to 380ºC is depicted for the Panorama skarn-forming fluid when compared to the granite (T = 585ºC), suggesting that it has also

679 equilibrated with the host PU gneisses and/or marbles. The Thapsana leucogranite
680 shows slightly lower $\delta^{18}O_{H2O}$ and δD values (T = 670ºC), however, the same trends for
681 the $\delta^{18}O_{H2O}$ and δD values indicate isotopic equilibrium with the host BU gneisses. The
682 above is in accordance with the REE patterns presented in Figure 4G. Possibly,
683 manganese was part of both primary magmatic and skarn-forming fluids (even after
684 assimilation of country rocks during magma ascend) but also part of later hydrothermal
685 fluids after mixing due to wall-rock interaction with early stage fluids.

686 Calcium and magnesium in the skarn-forming fluid have an initial magmatic
687 signature (T = 670º and 585ºC, Fig. 5B). The increasing trends of $\delta^{44}Ca_{BSE}$ and
688 $\delta^{26}Mg_{DSM-3}$ values towards the host gneisses and marbles on the $\delta^{44}Ca_{BSE}$ versus
689 $\delta^{26}Mg_{DSM-3}$ plot suggest that (e.g., T ~500º and 380ºC) there was a greater contribution
690 from the host rocks of Ca, Mg and Mn during the evolution of the mangan skarns, that
691 resulted in enrichment in manganese of the skarn-forming fluid (Fig. 6B). The
692 Panorama mangan skarn displays a decreasing trend of $\delta^{18}O_{H2O}$ and $^{87}Sr/^{86}Sr$ values
693 (Fig. 6C). This trend is most probably related to fluid-rock interaction due to the
694 increased influence and isotopic equilibration of the PU marbles, rather than the PU
695 gneisses, with the skarn-forming fluid (see Fig. 4G and Tornos and Spiro, 2000, c.f.,
696 Fig. 8). However, the Thapsana mangan skarn displays the opposite trend as
697 temperature decreases (from the Jhn-Sps zone to the Sps-Cum zone), i.e.,., towards
698 increasing $\delta^{18}O$ and $^{87}Sr/^{86}Sr$ values (Fig. 5C) which is interpreted as predominant fluid-
699 rock interaction and isotopic equilibrium with the BU gneisses.

700 The temporal evolution of the mangan skarns (i.e., from the ~26 Ma Panorama
701 granite to the ~ 24.8 Ma skarns and from ~7.4 Ma Thapsana leucogranite to the ~6.0
702 Ma skarns) and simple cooling (from T = 585º or 670º down to 480º and 380ºC),
703 coupled with the observed trends on Figures 5A, B and C, indicate that the mangan

skarn-forming fluids tend to equilibrate with their host rocks, at progressively higher water-to-rock ratios. Fluid-rock interaction is also indicated by our petrochemical results (e.g., log(Mn/Fe) versus log(Al/Ca) and Rb/Sr versus Rb/Ba plots, Figs. 4D, F). The Thapsana leucogranite is characterized by relatively elevated $\delta^{18}O_{H2O}$, δD and $^{87}Sr/^{86}Sr_{(i)}$ values, which are suggestive of its peraluminous affinity (Fig. 5C). Additionally, for the Panorama granite the above values are lower, and so the calcic skarn may be related to its metaluminous lithophases. At Panorama, fluid-rock metasomatism and buffering with the PU marbles was probably more intense and at higher temperature, which could explain why the Panorama skarn is a transitional phase between a mangan and a calcic skarn (e.g., formation of the Grt-Wo, Grt-Px zones).

Based on our fluid inclusion and isotopic results we propose two different sources for manganese. At Thapsana mangan skarn (e.g., Rdn and Jhn-Sps zones), the source for manganese was partly the Thapsana leucogranite due to its peraluminous affinity. The main process responsible for the enrichment of manganese in the skarn-forming fluid for both the Panorama and Thapsana late mangan zones (e.g., Grt-Ep and Sps-Cum zones) was its remobilization from both the peraluminous granitoids and the host PU marbles and BU gneisses due to fluid-rock interaction (Fig. 6A, B, C).

7.2. Tectono-metallogenic model of mangan skarn formation

The Panorama and ACM granitoids are commonly peraluminous granites-to-leucogranites in composition. These comprise higher silica and water contents (e.g., 7-8 wt. % H_2O), oxygen and strontium isotopic compositions and low iron, sodium and potassium contents. Their magmas were initially mildly oxidizing. Furthermore, they were emplaced at relatively low temperature (e.g., T ≤ ~700°C) and mid-crustal depths (e.g., P ~300 MPa). During their fractionation and under mildly oxidizing conditions,

729 the moderately incompatible manganese was released through anatexis of the CBU-
730 enriched meta-volcanosedimentary rocks (reported from the islands of Andros, Tinos,
731 Evia, Kythnos, Syros, Ikaria and Naxos and Varnavas, Attica, with ≤ 13.10 wt. % MnO,
732 Stouraiti et al., 2022). Our geochemical data for these peraluminous granitoids are
733 consistent with derivation from ~50 to 60% anatexis (Panorama granite) and ~35 to
734 45% (Thapsana leucogranite) of a plagioclase-rich metasedimentary source (as their
735 CaO/Na_2O ratios are ≥ 0.3, Fig. 4F, ESM 1, Table 8, Sylvester, 1998; Stouraiti et al.,
736 2010, 2022), i.e., metagreywacke (Stouraiti et al., 2010) which is most probably
737 represented by the BU gneisses (Fig. 4F).

738 It is proposed that manganese was enriched in the residual melts as they evolved to
739 more peraluminous compositions due to cooling (as shown experimentally by Maner et
740 al., 2019). The Panorama, Paros, Ikaria, Naxos and Tinos peraluminous granites-to-
741 leucogranites (emplaced at T ≈ 670º to 585ºC, at $\log fO_2$ values between HM-4.9 and
742 HM-2.0) contain Mn-enriched-amphibole (≤ 0.63 apfu), -biotite (≤ 0.33 apfu) and -
743 muscovite (≤ 0.05 apfu), as well as -magnetite (≤ 0.10 apfu) and ilmenite, -tourmaline
744 (schorl or Mn-schorl, ≤ 0.15 apfu) and spessartine ($Sps_{\sim 40\text{-}60}$), cordierite, sillimanite
745 and apatite (Mn ≤ 0.1 apfu) as accessory minerals (Meyer, 1968; Jones et al., 1992; Pe-
746 Piper, 2000; Mastrakas and Seymour, 2001; Hezel et al., 2011; Kevrekidis et al., 2015).
747 The formation of the Greek mangan skarns is linked to magmas relatively enriched in
748 volatiles (e.g., in boron, Pe-Piper, 2000; Kevrekidis et al., 2015, Table 1a), as the
749 crystallization of biotite helped manganese to be fixed in manganoan tourmaline, and
750 so to be enriched in the residual melts.

751 Volatiles and incompatible manganese tend to concentrate even further in the skarn-
752 forming fluid. Chemical elements driving skarn metasomatism, e.g., Na, K, Ca, Fe, Cl
753 and Mn (Table 1) are dominantly partitioned into the circulating fluid phase. If such

754 skarn-forming fluid, is enriched in manganese, and then exsolved the Thapsana and
755 Panorama mangan skarns could have been formed (at T ~550º down to ~300ºC and
756 pressure of 150 MPa). Moreover, the skarn-forming fluid is expected to interact (at T ≤
757 400ºC) with this highly differentiated melt (comprising ≤ 0.12 wt. % MnO, Jones et al.,
758 1992; Pe-Piper, 2000; Mastrakas and Seymour, 2001; Kevrekidis et al., 2015), or the
759 surrounding PU and BU rocks that are also relatively enriched in manganese (≤ 13.10
760 wt. % MnO, Pe-Piper, 2000; Stouraiti et al., 2010, 2022; Papaspyrou, 2016). The
761 metasomatic phase tends to remobilize part of the initial manganese of these granites-
762 to-leucogranites and/or PU marbles and BU gneiss.
763
764 **8. Conclusions**
765 Our conclusions, based on the synthesis of geological, mineralogical, chronological
766 and isotopic data and thermodynamic modeling of the Greek mangan skarns, are as
767 follows:
768 • The anhydrous manganoan skarn assemblages were deposited at T ≈ 550ºC and
769 were followed by hydrous manganoan assemblages (T ≈ 500ºC and ≈ 380ºC), at
770 pressures of ~150 MPa, during uplift.
771 • Our modeling suggests that the manganoan skarn assemblages were to the
772 products of phase separation (at ~480ºC and ~120 MPa, and ~400ºC and ~100 MPa),
773 mixing, cooling, dilution and fluid-rock interaction, fluctuation of pH and $\log f O_2$ values
774 and manganese redox state of the skarn-forming fluid.
775 • Two different sources are proposed for manganese, the peraluminous
776 granitoids, which are enriched in manganese, and the host PU marbles and BU gneisses.

- Manganese is enriched in reduced skarns related to peraluminous granites-to-leucogranites produced by the anatexis of ~60 to 35% of a meta-volcanosedimentary manganese-enriched source.

This study addresses two main issues. The first is why the Ikaria, Tinos and Naxos leucogranites do not seem to be associated with mangan skarn formation, and the second is why the Panorama and Paros mangan skarns do not comprise any Pb-Zn (±Ag) deposits. The proposed answer to the first issue is that the metasomatic fluids in Panorama and Paros were liquid-like fluids that have the capacity to store elevated amounts of manganese, in contrast to those at Tinos (Tombros and Fitros, 2019), Naxos and Ikaria which were vapor-like skarn forming fluids. The second issue most probably relates with the distance from their parental leucogranite. As manganese, lead and zing have the capacity to travel longer distances, using as an example the Paros leucogranite, it is expected that manganoan-oxide skarn ores will develop closer to the leucogranite (e.g., at Thapsana, Lakos Angerias, Paraga and Tripiti mineralizations). At greater distances Pb-Zn (±Ag) sulfide mineralizations may occur in "fluid escape structures" (following Meinert et al., 2005, e.g., the Monastiria, Agios Georgios, Prasovounia, Kaki skala, Lioria, Grafia, Bougouka and Skarvaneli in Despotico isle, vein-type mineralization comprising galena, sphalerite, chalcopyrite and pyrite) in the neighboring Island of Antiparos. Even further from the Paros leucogranite the hydrothermal, supergene manganese (±iron) oxides/hydroxides (e.g., Xatzovounia, Manganies in Antiparos) may occur (Fig. 8).

Acknowledgments: We kindly thank Mr. A.K. Seferlis from the Laboratory of Electron Microscopy and Microanalysis for the SEM microanalyses, and V. Stamoulis

from the Department of Material Science, University of Patras for the Infrared spectroscopy analyses.

References

Altherr, R., and Siebel, W., 2002, I-type plutonism in a continental back-arc setting, Miocene granitoids and monzonites from the central Aegean Sea, Greece: Contribution to Mineralogy and Petrology, v. 143, p. 397-415.

Altherr, R., Henjes-Kunst, F., Mathews, A., Friedrichsen, H., and Hansen, B.T., 1988, O-Sr isotopic variations in Miocene granitoids from the Aegean: evidence for an origin by combined assimilation and fractional crystallization: Contribution to Mineralogy and Petrology, v. 100, p. 528-541.

Altherr, R., Kreuzer, H., Wendt, I., Lenz, H., Wagner, G.A., Keller, J., Harre, W., and Hohndorf, A., 1982, A late Oligocene/Early Miocene high temperature belt in the Attico-Cycladic crystalline complex (SE Pelagonia, Greece): Geologisches Jahrbuch, v. 23, p. 97-164.

Abs-Wurmbach, I., and Peters, T., 1999, The Mn-Al-Si-O system: An experimental study of phase relations applied to paragenesis in manganese-rich ores and rocks: European Journal of Mineralogy, v. 11, p. 45-68, 10.1127/ejm/11/1/0045.

Baker, T., van Achterberg, E., Ryan, C.G., and Lang, J.R., 2004, Composition and evolution of ore fluids in a magmatic-hydrothermal skarn deposit: Geology, v. 32, p. 117-120.

Bargnesi, E.A., Stockli, D.F., Mancktelow, N., and Soukis, K., 2013, Miocene core complex development and coeval supradetatchment basin of Paros, Greece, insights from (U-Th)/He thermochronometry: Tectonophysics, v. 595-596, p. 165-182.

Bastrakov, E.N., Shvarov, Y.V., Girvan, S., Cleverley, J.S., and Wyborn, L., 2004, FreeGs: web-enabled thermodynamic database for modeling of geochemical processes, in, McPhie, J., and McGoldrick, P., eds., Dynamic Earth: Past, Present and Future. Abstracts of the 17th Australian Geological Convention, Hobart, Tasmania, Australia, p. 52.

Belardi, G., Spaziani, E., and Passeri, L., 2008, Beneficiation of wollastonite ores from Swedish, Greek and Spanish deposits: Bridging the Gap between Minerals and Materials, Egypt, p. 1-32.

Berman, R.G., Brown, T.H., and Perkins, E.H., 1987, Geo-Calc; a software for calculation and display of P-T-X phase diagrams, American Mineralogist, v. 72, p. 861-862.

Bethke, C., and Yeakel, S., 2016, The Geochemist's Workbench® Release 11 - GWB Essentials Guide, https://www.gwb.com/pdf/GWB11/GWBessentials.pdf.

Bethke, C.M., 1998, Software program version 3.2.2: React, Rxn, Act2, Tact and Gplot. University of Illinois, Illinois.

Bodnar, R.J., 2003, Introduction to aqueous fluid systems, *in* Samson, I., Anderson, A., and Marshall, D., eds., Fluid Inclusions: Analysis and Interpretation: Mineralogical Association of Canada, Short Course, v. 32, p. 81-99.

Bowman, J.R., 1998, Stable-isotope systematics of skarns, in Lentz, D.R. ed., Mineralized intrusion-related skarn systems: Mineralogical Association of Canada Short Course Series, v. 26, p. 99-145.

Bricker, O., 1965. Some stability relations in the system Mn-O_2-H_2O at 25 ^oC and one atmosphere total pressure: American Mineralogist, v. 50, p. 1296-1354.

Bröcker, M., and Franz, L., 1998, Rb-Sr isotope studies on Tinos Island (Cyclades, Greece): Additional time constraints for metamorphism, extent of infiltration-controlled overprinting and deformational activity: Geological Magazine, v. 135, p. 369-382.

Brookins, D.G.,1988, Eh-pH diagrams for geochemistry. Springer-Verlag, Berlin Heidelberg, 287p. doi.org/10.1007/978-3-642-73093-1

Chappell, B.W., and White, A.J.R., 1992. I- and S-type granites in the Lachlan Fold Belt: Transactions of the Royal Society of Edinburgh Earth Sciences, v. 83, p. 1-26.

Constadinidou, H., Patronis, M., Zangalis, K., Economou, G., 1998, Mineralogical characteristics related to the quality and recovery of the Panorama wollastonite, Drama area, Northern Greece: Bulletin of the Geological Society of Greece, v. 32, p. 295-302.

Damman, H.A., 1989, Mn-silicate skarns from the Gasborn area, West Bergslagen, central Sweden: Mineralogical Magazine, v. 53, p. 613-626.

Faryad, S.W., 1994, Mineralogy of the Mn-rich rocks from greenschist facies sequences of the Gemericum, West Carpathians, Slovakia: Neues Jahrbuch für Mineralogie Mineralogie, v. 10, p. 464-480.

Ferry, J.M. and Spear, F.S., (1978), Experimental calibration of the partitioning of Fe and Mg between biotite and garnet: Contributions to Mineralogy and Petrology, v. 66, p. 113-117.

Fitros, M., Tombros, S. F., Simos, X.C., Kokkalas, S., and Hatzipanagiotou, K., 2018, Formation of Mn-skarn ores at Thapsana Mines, Paros Island, Attico-Cycladic Metallogenetic Massif, Greece, in Proceedings of the 1st International Electronic Conference on Mineral Science, p. 16-31, doi:10.3390/IECMS2018-05461.

Goldsmith, J.R., and Graf, D.L., 1957, The system CaO-MnO-CO_2: solid solution and decomposition relations: Geochimica et Cosmochimica Acta, v. 11, p. 310-334.

Huang, J.-C., Peng, J., Yang, J.-H., Bang-Lu, Z., and Xu, C.-X., 2015, Precise zircon U-Pb and molybdenite Re-Os dating of the Shuikoushan granodiorite-related Pb-Zn mineralization, southern Hunan, South China: Ore Geology Reviews, v. 71, p. 305-317, 10.1016/j.oregeorev.2015.06.011.

Hammarstrom, J.M., and Zen, E.-An., 1986, Aluminum in hornblende: an empirical igneous geobarometer: American Mineralogist, v. 71, p. 1297-1313.

Helgeson, H.C., Kirkham, D., and Flowers, G.C., 1981, Thermodynamic behavior of aqueous electrolytes at high pressures and temperatures. IV. Calculation of activity coefficients, osmotic coefficients, and apparent molal and standard and relative partial molal properties to 600 C and 5kb: American Journal of Science, v. 281, p. 1249-1251.

Henley, R.W., Truesdell, A.H., and Barton, P.B. Jr. 1984, Fluid-mineral equilibria in hydrothermal systems: Reviews in Economic Geology, v. 1, p. 267.

Hezel, D.C., Kalt, A., Marschall, H.R., Ludwig, T., and Meyer, H.P., 2011, Major-element and Li, Be compositional evolution of tourmaline in an S-type granite-pegmatite system and its country rocks: An example from Ikaria, Aegean Sea, Greece: The Canadian Mineralogist, v. 49, p. 321-340, doi:10.3749/canmin.49.1.321.

Iliopoulos, I., 2005, Petrogenesis of the metamorphic rocks of Ikaria Island: Unpublished PhD, University of Patras, p. 407.

Johnson, J.W., Oelkers, E.H., and Helgeson, H.C., 1992, SUPCRT92: A software package for calculating the standard molal thermodynamic properties of minerals,

gases, aqueous species and reactions from 1 to 5000 bars and 0° to 1000°C: Computers and Geosciences v. 18, p. 899-947.

Jolivet, L., Menant, A., Sternai, P., Rabillard, A., Arbaret, L., Augier, R., Laurent, V., Beaudoin, A., Grasemann, B., Huet, B., Labrousse, L., and Le Pourhiet, L., 2015, The geological signature of a slab tear below the Aegean: Tectonophysics, v. 659, p. 166-182, doi:10.1016/j.tecto.2015.08.004Get.

Jones, C.E., Tarney, J., Baker J.H., and Gerouki F., 1992, Tertiary granitoids of Rhodope, northern Greece: magmatism related to extensional collapse of the Hellenic Orogen: Tectonophysics, v. 210, p. 295-314.

Kevrekidis E., St. Seymour, K., Tombros, S.F., Zhai, D., Liu, J., and Zouzias, D., 2015, The Agios Georgios argentiferous galena deposit on Antiparos Island, Cyclades, Hellas, and its relationship to the Paros leucogranite: Neues Jahrbuch für Mineralogie Abhandlungen-Journal of Mineralogy and Geochemistry, v. 192, p. 1-23, doi:10.1127/njma/2015/0283.

Kilias, A., 2021, The Hellenides: A multiphase deformed orogenic belt, its structural architecture, kinematics and geotectonic setting during the Alpine orogeny: Compression vs Extension the dynamic peer for the orogen making. A synthesis: Journal of Geology and Geoscience, v. 15, p. 1-56, .

Kilias, S.P., Pozo, M., Bustillo, M., Stamatakis, M.G., and Calvo, J.P., 2006, Origin of the Rubian carbonate-hosted magnesite deposit, Galicia, NW Spain: mineralogical, REE, fluid inclusion and isotopic evidence: Mineralium Deposita, v. 41, p. 713-733.Knight, C.L., and Bodnar, R.I., 1989, Synthetic fluid inclusions. IX. Critical PVTX properties of NaCI-H_2O solutions: Geochimica et Cosmochimica Acta v. 53, p. 3-8.

Kuşcu, I., Yılmazer, E., Güleç, N., Bayır, S., Demirela, G., Gençalioğlu-Kuşcu, G., Gezer, G., Kuru, S., and Kaymakcı, N., 2011, U-Pb and ^{40}Ar-^{39}Ar geochronology and isotopic constraints on the genesis of copper-gold-bearing iron oxide deposits in the Hasançelebi district, Eastern Turkey: Economic Geology, v. 106, p. 261-288.

Laurent, V., Beaudoin, A., Jolivet, L., Arbaret, L., Augier, R., Rabillard, A., 2015, Interactions between extensional shear zones and syn-tectonic granite intrusion: the example of Ikaria island (Cyclades, Greece): Tectonophysics, v. 651-652, p. 152-171. http://dx.doi.org/ 10.1016/j.tecto.2015.1003.1020.

Le Maitre, R.W., Bateman, P., Dudek, A., Keller, J., Lameyre, J., Le Bas, M.J., Sabine, P.A., Schmid, R., Sorensen, H., Streckeisen, A., Wooley, A.R., and Zanettin, B., 1989, A classification of igneous rocks and glossary of terms: Blackwell, Oxford, 193 p.

Liverton, T., 2016, A-type granite plutons and tin skarns in southeast Yukon: Mindy prospect and surrounding granite of 105C/9, in MacFarlane, K.E., and Nordling, M.G., eds., Yukon Exploration and Geology 2015, Yukon Geological Survey, p. 151-164.

Li, W.Y., Teng, F.Z., Ke, S., Rudnick, R.L., Gao, S., Wu, F.-Y., and Chappell, B.W., 2010, Heterogeneous magnesium isotopic composition of the upper continental crust: Geochimica et Cosmochimica Acta, v. 74, p. 6867-6884.

Malandri, C., Soukis, K., Maffione, M., Ozkaptan, M., Vassilakis, E., Lozios, S., and van Hinsbergen, D.J., 2016, Vertical-axis rotations accommodated along the MidCycladic lineament on Paros Island in the extensional heart of the Aegean orocline (Greece): Lithosphere, v. 9, p. 78-99, doi.org/10.1130/L575.1.

945 Maner, L.J., London, D., and Icenhower, J., 2019, Enrichment of manganese to
946 spessartine saturation in granite-pegmatite systems: American Mineralogist, v.
947 104, p. 1625-1637, doi.org/10.2138/am-2019-6938.
948 Maniar, P.D., and Piccoli, P.M., 1989, Tectonic discrimination of granitoids:
949 Geological Society of America Bulletin, v. 101, p. 635-643.
950 Marshall, B.D., and DePaolo, D.J., 1989, Calcium isotopes in igneous rocks and the
951 origin of granite: Geochimica et Cosmochimica Acta, v. 53, p. 917-922,
952 doi.org/10.1016/0016-7037(89)90036-7.
953 Martín, J.D., 1996, EQMIN, a Microsoft® Excel© spreadsheet to perform
954 thermodynamic calculations: A didactic approach: Computers and Geosciences,
955 v. 22, p. 639-650.
956 Mastrakas, N., and St. Seymour, K., 2000, Geochemistry of Tinos granite: A window
957 to the Miocene microplate tectonics of the Aegean region: Neues Jarhbuch für
958 Mineralogie Abhandlungen v. 175, p. 295-315.
959 McDonough, W.F., Sun, S., 1995, The composition of the Earth: Chemical Geology, v.
960 120, p. 223-253.
961 McGrath, A.G., 1999, Structural and geochemical evolution of H-type (Hybrid)
962 granitoids in an extensional metamorphic core complex, Paros, Greece:
963 Unpublished PhD, University of Leicester, p. 170.
964 Megaw, P.K.M., Ruiz, J. and Titley, S.R., 1988, High-temperature, carbonate-hosted
965 Ag-Pb-Zn(Cu) deposits of Northern Mexico: Economic Geology, v.83, p. 1856-
966 1885.
967 Meinert, L.D., 1987. Skarn zonation and fluid evolution in the Groundhog mine,
968 Central mining district, New Mexico: Economic Geology, v. 82, p. 523-545.
969 Meinert, L.D., Dipple, G., and Nicolescu, S., 2005, World skarn deposit: Economic
970 Geology 100th Anniversary Volume, Hedenquist, W.F., Thompson, J., Richard,
971 F.H., Goldfarb, J., and Richards, P.J., eds., Society of Economic Geologists, Inc.
972 Littleton, Colorado, p. 299-336.
973 Meyer, W., 1968, Alterstellung des plutonismus im südteil der Rila-Rhodope-Masse:
974 Geological Paleontology, v. 2, p. 177-192.
975 Moulas, E., Kostopoulos, D., Connolly, J.A.D., and Burg, J.-P., 2013, P-T estimates
976 and timing of the sapphirine-bearing metamorphic overprint in kyanite eclogites
977 from Central Rhodope, Northern Greece: Petrology, v. 21, p. 507-521.
978 Newberry, R.J., Einaudi, T.M., Eastman, H.S., 1991, Zoning and genesis of the Darwin
979 Pb-Zn-Ag skarn deposit, California; a reinterpretation based on new
980 data: Economic Geology, v. 86, p. 960-
981 982, doi.org/10.2113/gsecongeo.86.5.960.
982 Nagel, T.J., Schmidt, S., Janák, M., Froitzheim, N., Jahn-Awe, S., and Georgiev, N.,
983 2011, The exposed base of a collapsing wedge: the Nestos Shear Zone (Rhodope
984 Metamorphic Province, Greece): Tectonics, v. 30, TC4009, p. 1-17,
985 doi:10.1029/2010TC002815.
986 Ntagkounaki, K., 1999, The plutonite of Panorama (Drama, Macedonia, N. Greece).
987 Mineralogy-petrology-geochemistry. Aristotle University of Thessaloniki, MSc
988 thesis, p. 125.
989 Papadopoulos, A.A., 2011, Natural radioactivity in relation to mineralogy,
990 geochemistry of uranium and thorium of magmatic rocks from Greece:
991 contribution to the use of natural building materials: PhD Thesis, Aristotle
992 University of Thessaloniki p. 297.

Papanikolaou, D., 1980, Contribution to the geology of Aegean Sea: The Island of Paros: Annales Geologiques des Pays Helléniques, v. 30, p. 65-96.

Papaspyrou, A.M., 2016, Mineralogical and geochemical study of skarn of Drama pluton, Drama, Greece. Aristotle University of Thessaloniki, MSc thesis, p. 138.

Paraskevopoulos, G., 1960, The Thapsana area manganese ore deposits: Annales Géologiques des Pays Helléniques, v. 11, p. 83-124.

Pattison, D.R.M., and Newton, R.C., 1989, Reversed experimental calibration of the garnet-clinopyroxene Fe-Mg exchange thermometer: Contribution to Mineralogy and Petrology, v. 101, p. 87-103.

Pearce, J., 1996, Sources and settings of granitic rocks: Episodes, v. 19, 120-125.

Pe-Piper, G., and Piper, D.J.W., 2007, Late Miocene igneous rocks of Samos: the role of tectonism in petrogene- sis in the southeastern Aegean: Geological Society of London, Special Publication, v. 291, p. 75-97.

Pe-Piper, G., 2000, Origin of S-type granites coeval with I-type granites in the Hellenic subduction system, Miocene of Naxos, Greece: European Journal of Mineralogy, v. 12, p. 859-875, doi: https://doi.org/10.1127/0935-1221/2000/0012-0859.Pokrovski, G.S., Borisova, A.Y., and Bychkov, A.Y., 2013, Speciation and transport of metals and metalloids in geological vapors: Reviews in Mineralogy and Geochemistry, v. 76, p. 165-218.

Powell, T.S., 2000, A review of exploration gas geothermometry: Proceedings, Twenty-Fifth Workshop on Geothermal Reservoir Engineering Stanford University, Stanford, California, SGP-TR-165.

Robelin, C., Chartrand, P., and Pelton, D.A., 2004a, Thermodynamic evaluation and optimization of the ($MgCl_2$+$CaCl_2$+$MnCl_2$+$FeCl_2$+$CoCl_2$+$NiCl_2$) system: The Journal of Chemical Thermodynamics, v. 36 (9), p. 793-808, doi.org/10.1016/j.jct.2004.05.004.

Robelin, C., Chartrand, P., and Pelton, D.A., 2004b, Thermodynamic evaluation and optimization of the (NaCl+KCl+$MgCl_2$+$CaCl_2$+$MnCl_2$+$FeCl_2$+$CoCl_2$+$NiCl_2$) system: The Journal of Chemical Thermodynamics, v. 36 (9), p. 809-828, doi.org/10.1016/j.jct.2004.05.005.

Shimizu, M., and Iiyama, J.T., 1982, Zinc-leads skarn deposits of Nakatatsu mine, central Japan: Economic Geology, v. 77, p. 1000-1012.

Soldatos, T., and Ntagkounaki, K., 2004, The plutonite of Panorama, Drama. Mineralogy, petrology and geochemistry: Bulletin of the Geological Society of Greece, 10th GSC Congress Thessaloniki, Extended Abstracts, p. 251-252.

Stouraiti, C., Mitropoulos, P., Tarney, J., Barreiro, B., McGrath, A.M., and Baltatzis, E., 2010, Geochemistry and petrogenesis of late Miocene granitoids, Cyclades, southern Aegean: Nature of source components: Lithos, v. 114, p. 337-352, doi.org/10.1016/j.lithos.2009.09.010.

Stouraiti, C., Pantziris, I., Vasilatos, C., Kanellopoulos, C., Mitropoulos, P., Pomonis, P., Moritz, R., and Chiaradia, M., 2017, Ophiolitic remnants from the upper and intermediate structural unit of the Attic-Cycladic crystalline belt (Aegean, Greece): Fingerprinting geochemical affinities of magmatic precursors: Geosciences, doi.org/10.3390/geosciences7010014.

Stouraiti, C., Lozios, S., Soukis, K., Mavrogonatos, C., Tsikos, H., Voudouris, P., Wang, H., Zamparas, C., Kollias, K., 2022, Manganese metallogenesis in the Hellenic arc: case studies from a Triassic rift-related volcaniclastic succession of the Cycladic Blueschist Unit, Greece. Ore Geology Reviews, 104694. https://doi.org/10.1016/j.oregeorev.2022.104694.

Sylvester, P.J., 1998, Post-collisional strongly peraluminous granites: Lithos, v. 45, p. 29-44, doi.org/10.1016/S0024-4937(98)00024-3.

Theye, T., Schreyer, W., and Fransolet, A.M., 1996, Low-temperature, low-pressure metamorphism of Mn-rich rocks in the Lienne Syncline, Venn-Stavelot Massif (Belgian Ardennes), and the role of carpholite: Journal of Petrology, v. 37, p. 767-783.

Tian, Y., Etschmann, B.E., Mei, Y., Grundler, P., Testemale, D., Hazemann, J.-L., Elliott, P., Ngothai, Y., and Brugger J., 2014, Speciation and thermodynamic properties of manganese (II) chloride complexes in hydrothermal fluids: in situ XAS study: Geochimica et Cosmochimica Acta, v. 129, p. 77-95.Tombros, S.F., and Fitros, M., 2019, Evidence for vapor transport of the base and precious metals in the Panormos Bay Ag-Au-Te deposit, Tinos Island, Cyclades: Journal of Geochemical Exploration, v. 199, p. 128-140, doi.org/10.1016/j.gexplo.2019.01.007.

Tornos, F., and Spiro, B.F., 2000, The geology and isotope geochemistry of the talc deposits of Puebla de Lillo (Cantabrian zone, northern Spain): Economic Geology, v. 95, p. 1277-1296, doi.org/10.2113/95.6.1277.

Uchida, E., Endo, S., and Makino, M., 2007, Relationship between solidification depth of granitic rocks and formation of hydrothermal ore deposits: Resource Geology, p. 57, p. 47-56.

Uchida, E., Haitani, T., Suetsugu, T., Kashima, T. and Tsutsui, K., 2003, Experiments on the element distribution between the granodiorite JG-1a and 2M NaCl hydrothermal solution at temperatures of 300 to 800°C and a pressure of 1 kb: Resource Geology, v. 53, 155-161, doi:10.1111/j.1751-3928.2003.tb00166.x.

Wang, Z.G., and Wang, L.L., 2011, Computer program of NET 2.0 C# for calculating physicochemical parameters from compositions of fluid inclusions: Mineral Deposits, v. 30, 754-758, doi: 10.16111/j.0258-7106.2011.04.017.

Whitney, D., and Evans, B., 2010, Abbreviations for names of rock-forming minerals: American Mineralogist, v. 95, p. 185-187.

Xypolias, P., Iliopoulos, I., Chatzaras, V., and Kokkalas, S., 2012, Subduction and exhumation related structures in the Cycladic Blueschists: insights from Evia Island (Aegean region, Greece): Tectonics v. 31, TC2001, doi: 10.1029/2011TC002946.

Yun, S., and Einaudi, T.M., 1982, Zinc-lead skarns of the Yeonhwa-Ulchin District, South Korea: Economic Geology, v. 77, p. 1013-1032, doi:10.2113/gsecongeo.77.4.1013.

Zaw, K., and Singoyi, B., 2000, Formation of magnetite-scheelite skarn mineralisation at Kara, Northwestern Tasmania: evidence from mineral chemistry and stable isotopes: Economic Geology, v. 95, p. 1215-1230, doi.org/10.2113/gsecongeo.95.6.1215.

Zen, E., 1985, Implications of magmatic epidote-bearing plutons on crustal evolution in the accreted terranes of northwestern North America: Geology v. 13, p. 266-269, doi.org/10.1130/0091-7613(1985)13.

Zhao, Y.M., 1991, Manganoan skarn formation, in, Barto-Kyriakidis, A., ed., Skarns-Their Genesis and Metallogeny, Theophrastus Publications S.A., Athens, p. 165-180.

Zhao, Y.M., Dong, Y., Li, D., and Bi, C., 2003, Geology, mineralogy, geochemistry, and zonation of the Bajiazi dolostone-hosted Zn-Pb-Ag skarn deposit, Liaoning

Province, China: Ore Geology Reviews, v. 23, p. 153-182, doi.org/10.1016/S0169-1368(03)00034-9.

Zimmer, K., Zhang, Y., Lu, P., Chen, Y., Zhang, G., Dalkilic, M., and Zhu, C., 2016, SUPCRTBL: A revised and extended thermodynamic dataset and software package of SUPCRT92: Computers and Geosciences, v. 90, p. 97-111.

Figure captions

Fig. 1. (A, B). Simplified geotectonic maps of the geology of the Rhodope and Attico-Cycladic Metallogenetic Massifs (modified after Kilias, 2021; Jolivet et al., 2015); (C, D, E) Simplified map of Panorama in Drama and Paros Island (modified after Ntagkounaki, 1999; Papaspyrou, 2016; Bargnesi et al., 2013; Laurent et al., 2015).

Fig. 2. Field photographs of: (A) The tectono-intrusive contact between the Panorama (Grt), calcic skarn (Ca-Sk) and host marble; (B) Representative hand specimen of the Grt-Ep zone in Panorama composed of epidote (~80 vol. %) and garnet (~20 vol. %); (C) Overview of mangan skarn (Mn-Sk) zonation in relation to the host marble and hornfels, in Thapsana, Paros; (D) Stage I mangan assemblage in relation to the Rdn and Sps-Cum zones comprising jacobsite, hausmannite and braunite crosscut by epidote veinlets; (E, F) Hand specimens of the Rdn and Jhn-Sps zones from Thapsana, Paros (Rdn = Rhodonite, Sps = Spessartine, Jhn = Johannsenite, Jac = Jacobsite, Hsm = Hausmannite and Br = Braunite, Grt = Garnet, Ep = Epidote, in all figures mineral abbreviations are after Whitney and Evans, 2010).

Fig. 3. (A). Representative crossed-polarized thin-section photomicrographs of the Grt-Ep zone in Panorama mangan skarn; (B). X-ray map of Mn (Ka) of the epidote crystal from cores to rims (the reddish and orangish-to-yellowish colors are attributed to represent the Mn^{3+} and Mn^{2+} contents); (C, D). Ternary plots showing compositional variations of pyroxene and garnet from the Panorama and Thapsana mangan skarn

(mauve, cyan, green and red squares, triangles and circles represent the cores, intermediate areas and rims of pyroxenes and garnets from Grt-Wo, Grt-Px, Grt-Ep and Jhn-Sps zones from Panorama and Thapsana, respectively); (E, F, G, H). Representative photomicrographs of the Sps-Cum and Jhn-Sps zones and mangan ores from Thapsana mangan skarn. At the down-right corner the composition of spinels is shown on the ternary Jac-Glx-Mag plot (yellow cycles); (G). Spessartine replaced by jacobsite in which the microprobe traverse method was applied (pink dots, scale bar = 2 mm), (Px = Johannsenite-Diopside series, Cum = Cummingtonite, Sps = Spessartine, Ep = Epidote, Jac = Jacobsite, Hsm = Hausmannite, Br = Braunite, Hol = Hollandite, Glx =Galaxite and Mag = Magnetite).; (I, K). Micro-traverse profiles of the garnet and pyroxene crystals (core-to-rim) displaying the variation of the spessartine (Sps), andradite (Adr), grossular (Grs), diopside (Di), johannsenite (Jhn) and hedenbergite (Hd) components (for both Panorama and Thapsana).

Fig. 4. Major and trace element classification plots demonstrating the petrochemistry of the Panorama and Thapsana pluton lithotypes: (A) SiO_2 versus (K_2O+Na_2O) plot for petrography and geochemical composition (fields are after Le Maitre et al., 1989); (B). SiO_2 versus Fe_2O_3/FeO+Fe_2O_3 plot of Panorama and Thapsana (field boundaries for skarn oxidation state are after Meinert et al., 2005); (C) Al/(Ca+Na+K) versus Al/(Na+K) plot outlining the alkaline, metaluminous and peraluminous, and I- and S-type granitoids (fields are after Maniar and Piccoli, 1989; Chappell and White, 1992); (D) Log(Mn/Fe) versus log(Al/Ca) plot displaying the possible source of manganese in skarns; (E) Log(Y+Nb) versus Rb discrimination plot. The petrotectonic fields are after Pearce (1996); (F) Log(Rb/Sr) versus log(Rb/Ba) ratios for the peraluminous granitoids. The dashed purple line separates granitoids formed by anatexis of clay-poor with higher plagioclase and CaO/Na_2O contents source (C-p) in respect to those

produced from clay-rich with lower plagioclase and CaO/Na_2O contents source (C-r). Modeling of the calculated compositions of pelite (Pe)- and psammite (Ps)-derived peraluminous granitoids, the average compositions of basalt (B), shale (S) and greywacke (G), and the calculated melt mixing curve (black dashed line) is also shown (after Sylvester, 1998); (G) Chondrite-normalized REE patterns (after McDonough and Sun, 1995) of the Panorama and Thapsana granitoids and mangan skarn zones (Panorama granite: solid black-, Grt-Wo, Grt-Px and Grt-Ep zones: dashed black-, Thapsana leucogranite: solid red-, Rdn, Jhn-Sps, Sps-Cum zones: dashed red-, Tinos leucogranite: dashed green-, Naxos leucogranite: dashed blue- and Ikaria leucogranite: light mauve-colored lines). In all the above plots we have used published geochemical data for Panorama, Paros, Ikaria Naxos, Samos and Tinos granites-to-leucogranites (crossed-open symbols) from Jones et al. (1992); Ntagkounaki (1999); Pe-Piper (2000); Mastrakas and Seymour (2001); Altherr and Siebel (2002); Iliopoulos (2005); Pe-Piper and Piper (2007); Stouraiti et al. (2010); Papadopoulos (2011); Kevrekidis et al. (2015).

Fig. 5. Photomicrographs of multiple fluid inclusion assemblages in spessartine host from Thapsana mangan skarn (photographed at + 22.5°C in plane-polarized transmitted light, scale bar = 50, 100, 200 and 250 μm): (A and B) Primary (P), and secondary (S) L-V, V-L and S-L-V inclusions (e.g., sample PTS1, A: Cores, and B: Rims), (C and D) Isolated primary $S_{1,2,3}$-L-V inclusions comprising antarcticite (And), rhodochrosite (Rds), manganese chlorides ($MnCl_x$) and CO_2. The inclusions are best described in the system H_2O-NaCl-$MnCl_2$-$CaCl_2$. (E) Liquid-vapor homogenization temperature versus salinity plot (C: Cores, R: Rims), (F) Temperature versus pressure plot showing trapping conditions of the Thapsana mangan skarn, (G) $Log(Mn^{total}/Ca^{2+}$ versus $logCl^-/HCO_3^-+CO_2^{2-}$) plot of fluid inclusion compositions Temperatures were obtained from gas and liquid-phase geothermometers of fluid inclusions (Table 1b).

1168 **Fig. 6.** (A) Hydrogen versus oxygen isotope plot showing the calculated water
1169 compositions from the Panorama and Thapsana mangan skarn. The "Meteoric Water
1170 and Kaolinite Lines", "Subduction-Related Vapor, Arc and Crystal Felsic Magma", "I-
1171 and S-type magmas", "Sedimentary rocks", "Metamorphic water box", "Formation
1172 waters" and "Primary magmatic water" are after Bowman (1998) and Kuşcu et al.
1173 (2011), (B) $\delta^{44}Ca_{BSE}$ versus $\delta^{26}Mg_{DSM-3}$ isotope plot showing the compositions of garnet
1174 from the Grt-Ep skarn zone. The "Plutonic rocks" and "Host rocks (Gneisses-Marbles)"
1175 fields are after Marshall and DePaolo (1989) and Li et al. (2010); (c). $\delta^{18}O_{H2O}$ versus
1176 $^{87}Sr/^{86}Sr_{(i)}$ plot of the mangan skarn showing their spatial and temporal evolution (ages
1177 are given in ESM Fig. 2, and in all the above plots we have used published isotope data
1178 Naxos, Ikaria and Tinos leucogranites from Altherr et al. (1998) and Bröcker and Franz
1179 (1998); (D, E) Isobaric (P = 150 MPa) temperature versus $\log f_{O2}$ ($X_{CO2} = 0.1$) and X_{CO2}
1180 versus temperature plots in the system $MnO\text{-}CaO\text{-}Al_2O_3\text{-}SiO_2\text{-}H_2O\text{-}CO_2$ displaying the
1181 estimated conditions and evolution of the Thapsana and Panorama mangan skarns
1182 (using thermodynamic theoretical and experimental data from Goldsmith and Graf,
1183 1957; Bricker, 1965; Faryad, 1994; Theye et al., 1996, and the EQMIN spreadsheet,
1184 Martín, 1996). Mineral reactions and abbreviations are listed in ESM Tables 10a, b.
1185 The Hematite-Magnetite (HM) and Jacobsite = Hausmannite + Hematite buffers are
1186 also shown.

1187 **Fig. 6.** Modeling of the metasomatic fluid related to the Thapsana and Panorama
1188 mangan skarns due to its simultaneous cooling (from 600° to 250°C) and fluid-rock
1189 interaction (1000 g of gneiss or marble with 1056.33 g of fluid): (A) Manganoan-
1190 aluminosilicates, -carbonates and -oxides skarn assemblages over cooling; (B) pH and
1191 oxygen fugacity changes (the red, green and black lines represent the Rdn (± Tep), Sps-

1192 Jhn and Sps-Cum zones, respectively); (C) Variation of ion complexes and gas
1193 concentrations of the metasomatic fluid; (D) Activity-temperature plot showing
1194 relationships at pressure of 150 MPa of the system MnO-CaO-Al_2O_3-SiO_2-H_2O-CO_2 as
1195 function of the activity ratios $\log[\alpha_{Mn}{}^{2+}/(\alpha_{H}{}^{+})^2]$ and $\log[\alpha_{Mn}{}^{3+}/(\alpha_{H}{}^{+})^3]$. (The Rdn (± Tep),
1196 Sps-Di-Cum and Pmt-Phl assemblages are conjectural). Mineral reactions and
1197 abbreviations are listed in ESM Tables 10a, b.

1198 **Fig. 7.** Tectono-metallogenic model for the formation of the mangan skarns in
1199 Greece (Horizontal axes is not to scale).

Tombros, S., Kokkalas, S., Triantafyllidis, S., Fitros, M., Tsikos, H., Papadopoulou, L., Voudouris, P., Zhai, D., Skliros, V., Perraki, M., Kappis, K., Spiliopoulou, A., Simos, X., Papavasiliou, J., and Williams-Jones, A. 2023, Genesis of a new type of mangan skarn associated with peraluminous granitoids in Greece: Chemical Geology, v. 623, p. 121369

Table 1a. Primary fluid inclusion microthermometric data from spessartine of the Thapsana mangan skarn.

Sample	Host mineral Spessartine	V/(V+L)%	Type	$T_{f\text{-}ice}$ (˚C)	$T_{m\text{-}ice}$ (˚C)	T_h[1] (˚C)	Salinity[2] (wt.% NaCl equiv)	Pressure (bars)
PTS1[3]	Core	11 to 25	L+V (n = 9)	-46 to -28	-30.7 to -16.3	418 to 502	18 to 30	1087 to 1305
PTS1	Core	50 to 72	V-L (n = 5)	-41 to -27	-7.9 to -2.5	425 to 530	3 to 13	1105 to 1378
PTS1	Core	12 to 37	S-L-V (n = 12)	-42 to -27	-47 to -34.8	305 to 565	28 to 45	832 to 1469
PTS1	Rim	9 to 29	L+V (n = 9)	-33 to -22	-15.2 to -5.2	320 to 423	8 to 15	793 to 1110
PTS1	Rim	49 to 70	V-L (n = 5)	-30 to -20	-8.1 to -3.9	339 to 470	6 to 11	881 to 1222
PTS1	Rim	20 to 39	S-L-V (n = 6)	-56 to -44	-48.2 to -34.7	339 to 438	48 to 33	881 to 1139

[1]Average temperature of homogenization of ~435ºC, st.d. = 67. The homogenization temperatures range from 305º to 565ºC for the cores and from 320º to 470ºC for the rims.

[2]Average salinity of ~24 wt. % NaCl equiv, st.d. = 13.5. Salinity ranges between ~3.0 and ~44.0 wt. % NaCl equiv for the spessartine cores and from ~6.0 to ~48.0 wt. % NaCl equiv for the rims.

[3]Test Run, Abbreviations: $T_{f\text{-}ice}$: First melting of ice, $T_{m\text{-}ice}$: Last melting of ice, T_h= Total fluid homogenization temperature, S= Solid, L= Liquid and V= Vapor.

Samples location: PTS = Thapsana skarn, Sps-Jhn zone.

The fluid inclusions sizes are mostly ≤ 20 to 25 and up to 80 in diameter (μm). The trapped solids were rhodochrosite (S_1), antarcticite (S_2), Mn-chlorides (S_3) and calcite (S_4), in addition to halite (based on their optical properties and Raman analyses in fluid inclusions that the vapor bubble occupies ≤ 40 vol. %, Fig.6). The polyphase L-V and S-L-V inclusions homogenize to liquid.

We have also used the equations of Knight and Bodnar (1989) to estimate the critical P-T-d properties of the Panorama, Thapsana in Paros, Tinos (Tombros and Fitros, 2019), Ikaria and Naxos skarn-forming leucogranite-related fluids. The critical T, P and d of this ore fluid were $T_{critical}$ = 680^{o}C, $P_{critical}$ = 0.01 GPa and $d_{critical}$ = 0.40 cm^3/g, for an average salinity of 24 wt. % NaCl equiv. Under these conditions the Panorama and Thapsana metasomatic fluids most likely were liquid-like fluids, whereas the ones at Tinos, Ikaria and Naxos were vapor-like skarn-forming fluids (see also Tombros and Fitros, 2019 and Pokrovski et al., 2013, cf. Fig. 1).

Table 1b. Primary fluid inclusion gaseous and liquid Raman data from spessartine of the Thapsana mangan skarn.

Gaseous phase					
Sample	Host mineral-Fluid inclusion type	X_{H2O} (Mol %)	X_{CO2} (mol %[A])	X_{H2} (Mol %)	X_{N2} (mol %)
PTS1	Vapour	86.9 to 94.1	5.6 to 8.6	0.0 to 0.5	0.0 to 0.7

Liquid phase								
Sample	Host mineral-Fluid inclusion type	Si^{+2} (ppm[B])	Na^{+} (ppm[C,D])	K^{+} (ppm[B,C,D])	Mg^{2+} (ppm[D])	Ca^{2+} (ppm[C])	Al^{3+} (ppm)	Pb^{2+} (ppm)
PTS1	Liquid	1185.0 to 1598.4	12.8 to 60.4	0.3 to 16.5	3.2 to 224.5	13.8 to 423.2	124.7 to 289.4	34.6 to 134.5
		Mn^{total} (ppm)	CO_3^{2-} (ppm)	HCO_3^{-} (ppm)	SO_4^{2-}(ppm)	Cl^{-} (ppm)	Fe^{2+} (ppm)	Salinity (corresponding wt. % NaCl equiv)[1]
PTS1	Liquid	960.8 to 4455.0	3321.5 to 5009.5	213.5 to 340.4	0.0 to 32.5	3384.5 to 4389.6	0.3 to 102.7	27.7 to 42.9

Temperature estimates based on fluid inclusions gaseous phase data used the $^{A}CO_2$-geothermometer (Henley et al., 1984, Table 3.2). The calculated temperatures range from 413° to 528°C. The average $\log(X_{CO2}/X_{H2O})$ range from -1.2 to -0.9 and -0.4 under a total pressure ranging between ~480 to ~700 bars (The error for all gases analyzed was ± 1%).

Temperature estimates based on fluid inclusions liquid phase data used the Na-K^{B}-, Na-K-Ca^{C}- and K-Mg^{D}-geothermometers (Henley et al., 1984, Table 5.3). The calculated temperatures range from 351° to 565°C. For the Na-K-Ca geothermometer the $\log\sqrt{Ca/Na}+2.06$ values ≥ 0, and T ≥ 100°C and so β = 0.7.

Traces of Ba^{2+} (≤ 7.5), F^{-} (≤ 4.1), B^{3+} (2.1 to 9.3) and Li^{+} (≤ 1.8) were only occasionally detected (in ppm). The average values of the liquid phase are $\log(Mn^{total}/Ca^{2+})$ = 0.9 to 2.4, $\log(Mn^{2+}/Mn^{3+})$ = 0.6 to 0.9, $\log(Cl^{-}/CO_3^{2-}+HCO_3^{-})$ = -0.1 to 0.0 and $\log(HCO_3^{-}/CO_3^{2-})$ = -1.4 to -1.0 (For the cations and anions the error was ±0.01 ppm).

[1]Independent calculation of the skarn-forming fluid salinity was based on solubility Raman data using the method of Wang Z and Wang L (2011). The calculated salinities range between 27.7 and 42.9 wt. % NaCl equiv, with a standard error of ± 2.8%.

Tombros, S., Kokkalas, S., Triantafyllidis, S., Fitros, M., Tsikos, H., Papadopoulou, L., Voudouris, P., Zhai, D., Skliros, V., Perraki, M., Kappis, K., Spiliopoulou, A., Simos, X., Papavasiliou, J., and Williams-Jones, A. 2023, Genesis of a new type of mangan skarn associated with peraluminous granitoids in Greece: Chemical Geology, v. 623, p. 121369

Table 2 Oxygen, carbon, hydrogen, calcium, magnesium, $^{87}Rb/^{86}Sr$ and $^{87}Sr/^{86}Sr$ isotope data obtained from Panorama in Drama, and Thapsana in Paros Island granite-to-leucogranite, skarns, ores and host rocks.

Sample	Mineral[1]	$\delta^{13}C_{V\text{-}PDB}$ (per mil)	$\delta^{18}O_{V\text{-}SMOW}$ (per mil)	δD (per mil)	$\delta^{44}Ca_{BSE}$ (per mil)	$\delta^{26}Mg_{DSM\text{-}3}$ (per mil)	$^{87}Rb/^{86}Sr$	$^{87}Sr/^{86}Sr$	$^{87}Sr/^{86}Sr(i)$[2]	Age
PAN_1 (Granite)	whole rock	-	11.22	-58	1.28	-0.22	2.99	0.7134	0.7116	25.79 ± 0.22 Ma
PAN_2 (Granite)	Qz	-	9.26	-75	-	-	0.53	0.7144	0.7127	
PAN_3 (Wo-Grt)	Wo	-	8.51	-67	0.52	-1.73	1.91	0.7145	0.7128	
PAN_4 (Px-Grt)	Di-Hd	-	8.89	-69	0.79	-1.25	0.47	0.7131	0.7114	24.92 ± 0.24 Ma
PAN_5 (Ep-Grt)	Grs	-	14.56	-71	0.63	-1.47	0.52	0.7128	0.7111	
PAN_5 (Marble)	Cal	-2.18	16.32	-42	0.28	-0.63	0.56	0.7169	0.7131	-
PTHAP_1 (Leucogranite)	whole rock	-	10.46	-64	1.14	-0.16	0.69	0.7156	0.7152	7.38 ± 0.13 Ma
PTHAP_2 (Leucogranite)	Qz	-	9.81	-82	-	-	0.65	0.7149	0.7144	
PTHAP_3 (Rhd)	Rhd	-	10.37	-42	0.59	-1.44	0.59	0.7169	0.7165	
PTHAP_4 (Jhn-Sps)	Jhn[A]	-	9.92	-57	0.94	-1.85	0.61	0.7149	0.7146	
PTHAP_5 (Jhn-Sps)	Sps[A]	-	8.26	-65	0.87	-1.74	0.59	0.7150	0.7146	6.29 ± 0.12 Ma
PTHAP_6	Sps	-	10.34	-69	0.79	-1.68	0.58	0.7155	0.7151	

(Jhn-Sps)										
PTHAP_7 (Sps-Cum)	Sps[B]	-	10.85	-75	1.01	-1.49	0.52	0.7166	0.7161	6.11 ± 0.15 Ma
PTHAP_8 (Sps-Cum)	Mn-Ep[B]	-	12.53	-80	1.06	-1.36	0.67	0.7167	0.7162	
PTHAP_9_ (Gneiss)	Qz	-	17.38	-48	0.51	-0.61	0.58	0.7176	0.7171	-
PTHAP_10_ (Mn ore)	Jab	-	7.15	-83	1.61	-1.07	0.58	0.7176	0.7171	-

[1]Temperatures for the mineral-H_2O calculations were obtained from fluid inclusions microthermometry, the CO_2 and Na-K-, Na-K-Ca- and K-Mg-geothermometers, the [A]johannsenite-spessartine (Jhn-Sps zone) and [B]spessartine-epidote (Sps-Cum zone) isotopic pairs (using the equations of Zhao and Zheng, 2003) and the garnet-clinopyroxene (Pattison and Newton, 1989), garnet-biotite (Ferry and Spear, 1978 as revised by Holdaway et al., 1997) and two-feldspar (Whitney and Stormer, 1977 as modified by Putirka, 2008) geothermometers. The obtained temperatures range from 305° and 565°C (av. ~435ºC). For Panorama mangan skarn the initial temperature of formation was considered to be ~585º (accessory spessartine in granite), the average was ~470º and the minimum was ~380ºC. For Thapsana the initial temperature of formation was ~565º, the average was ~435º and the minimum was ~305ºC (maximum, average and minimum temperatures obtained from fluid inclusion microthermometry).

[2]The initial $^{87}Sr/^{86}Sr$ values were calculated for Panorama using an age of 26.8 ± 0.5 Ma (Mayer, 1968), and for Thapsana an age of 7.5 ± 0.6 Ma (Bargnesi et al., 2013).

Sample location: PAN = Panorama, and PTHAP = Paros, Thapsana.

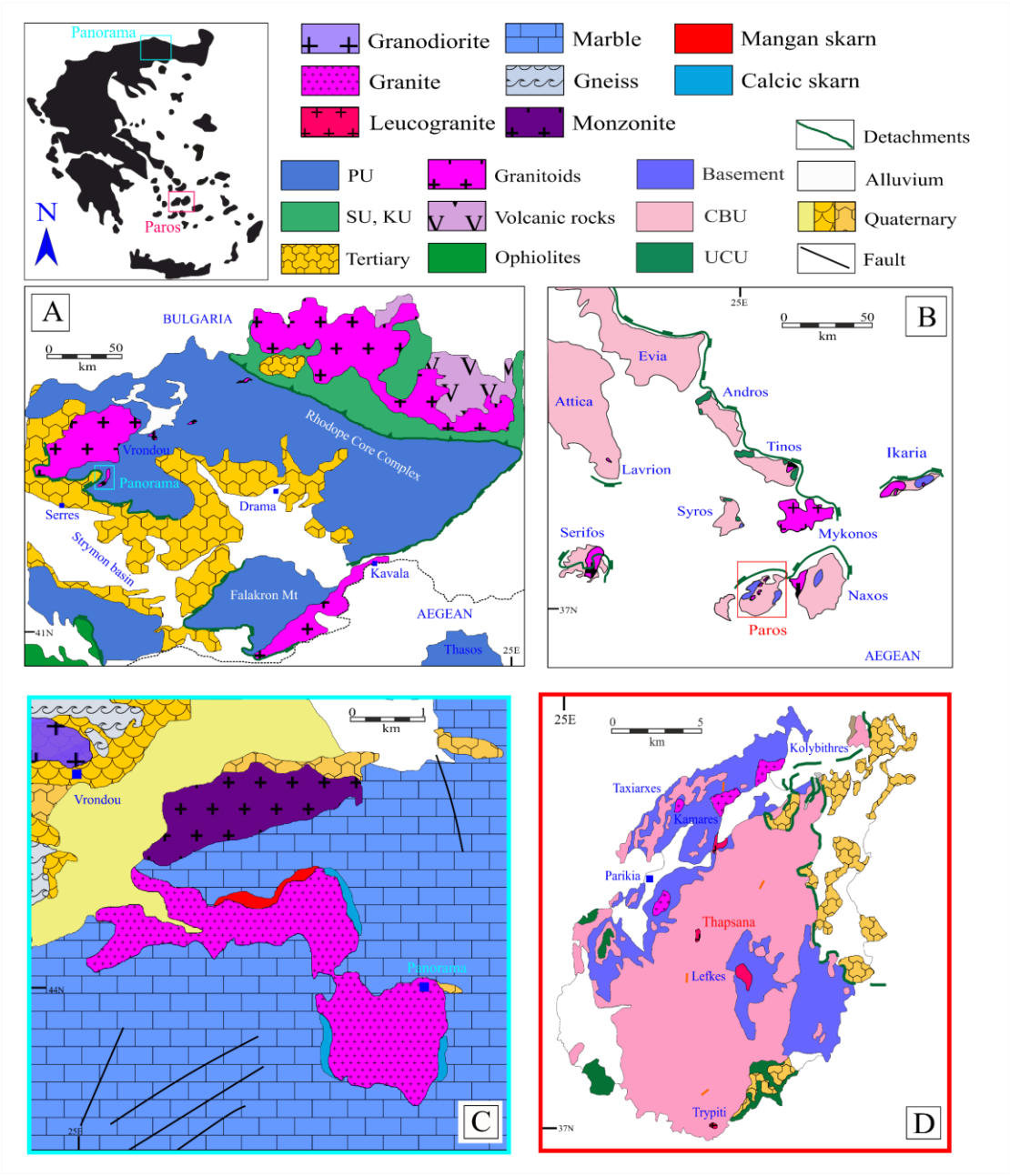

Fig. 1

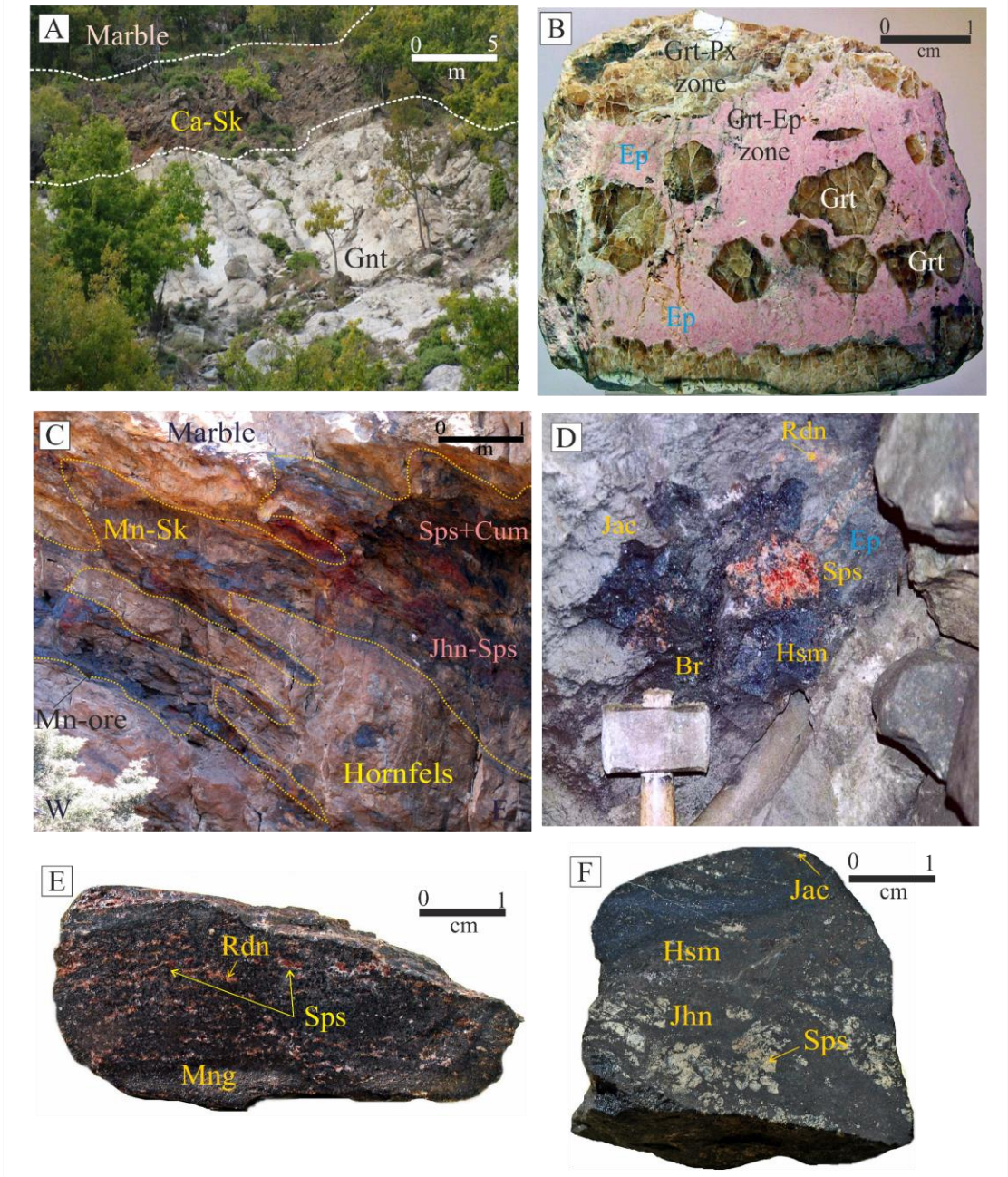

Fig. 2

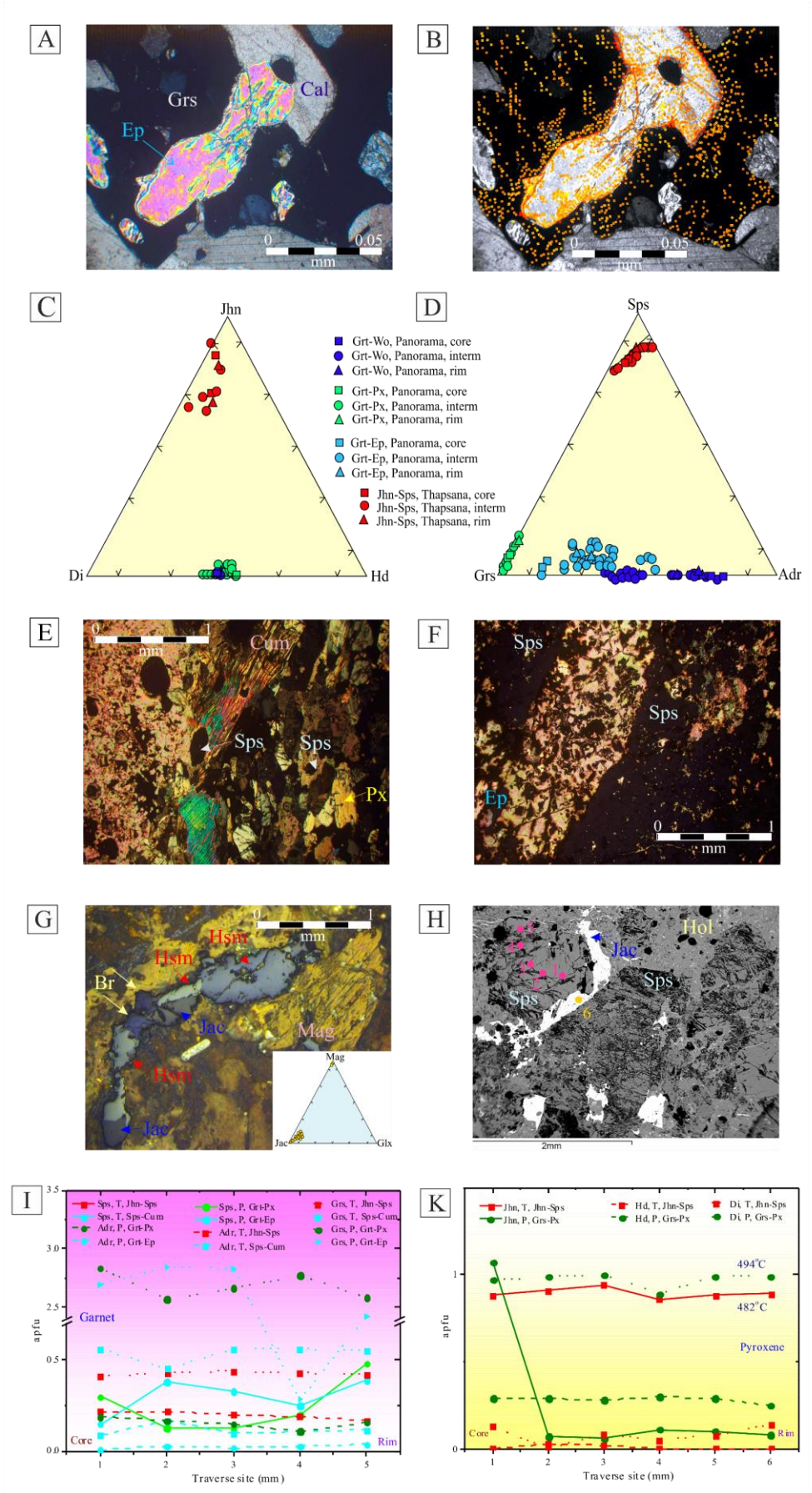

Fig 3

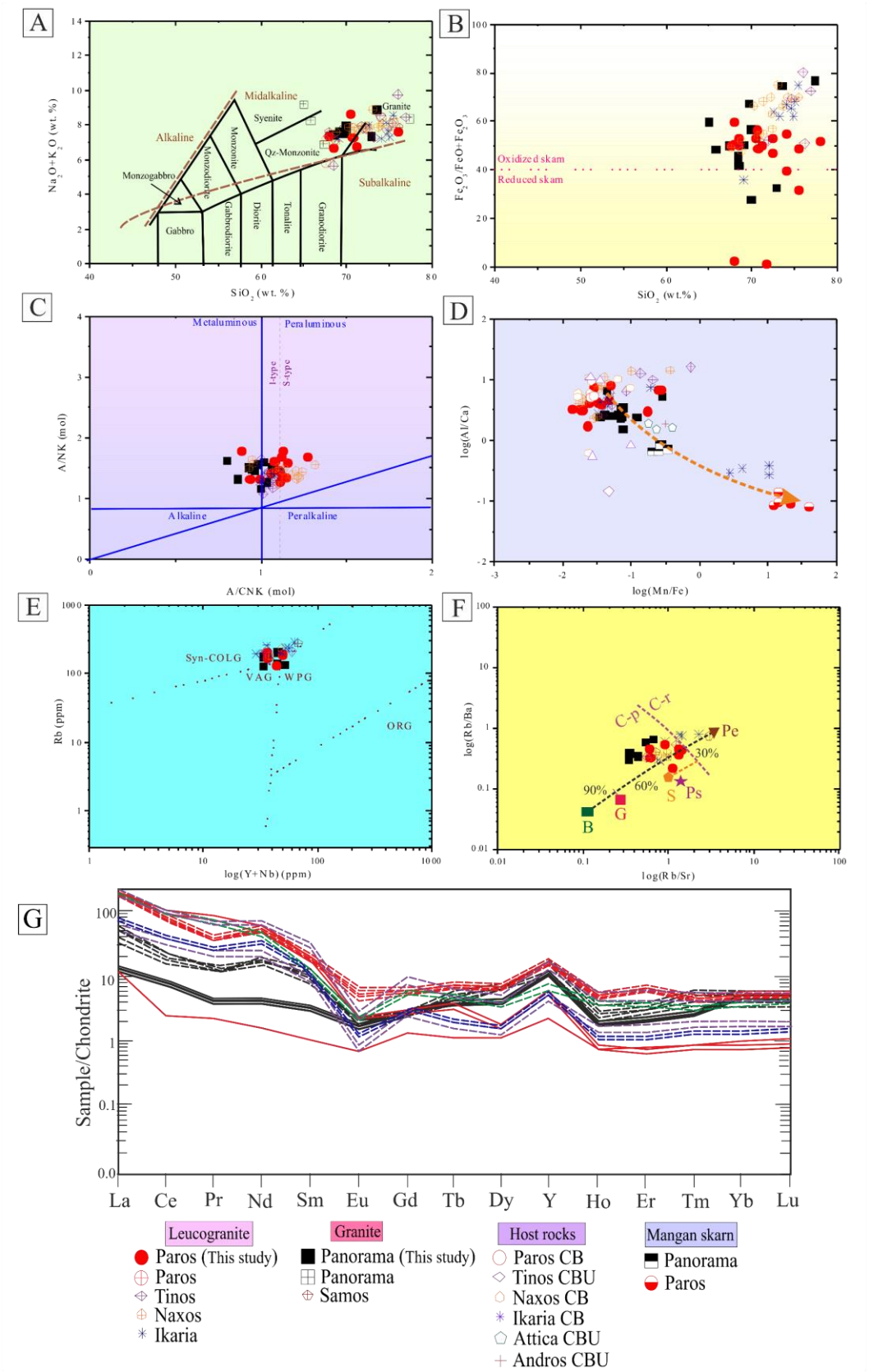

Fig.4

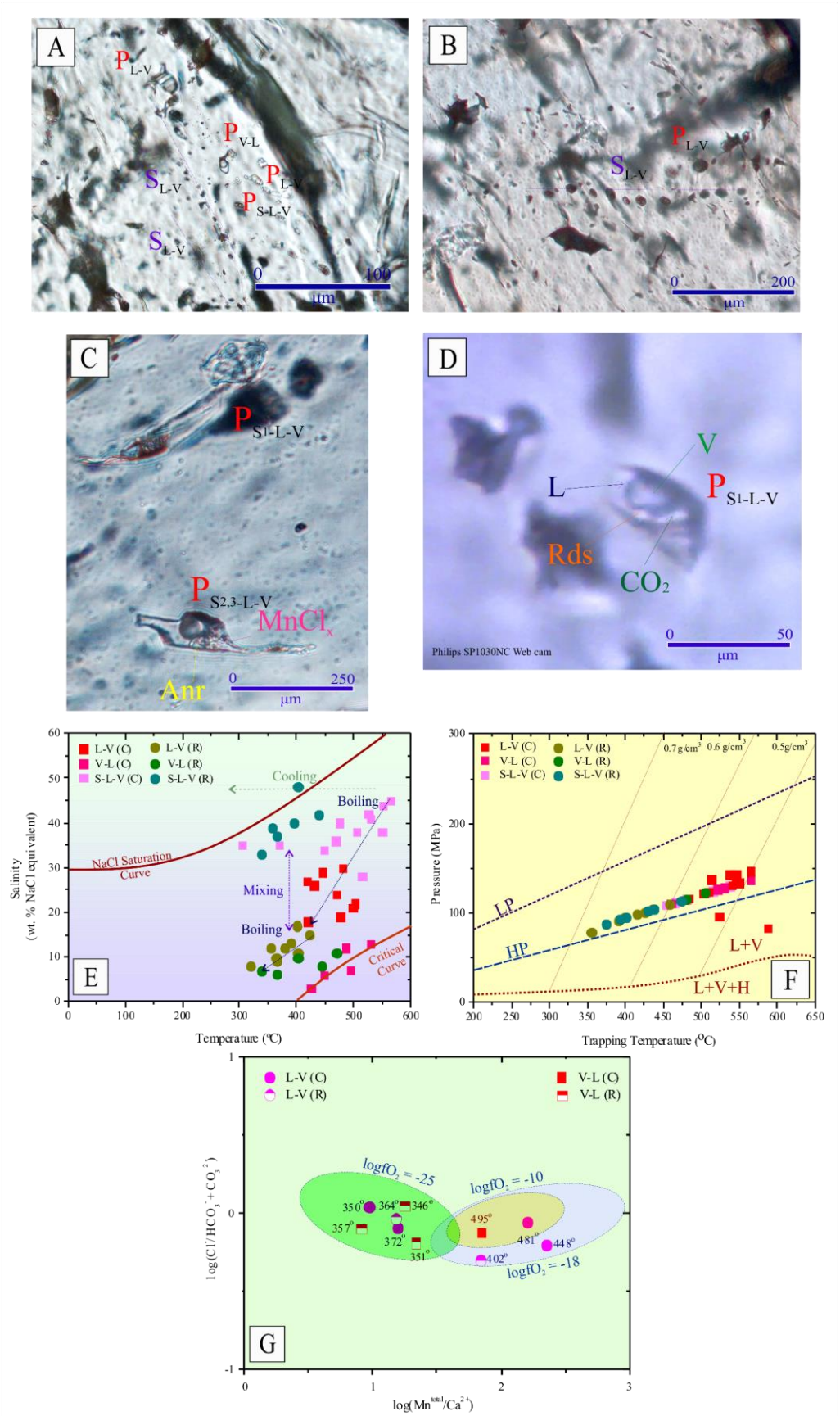

Fig.5

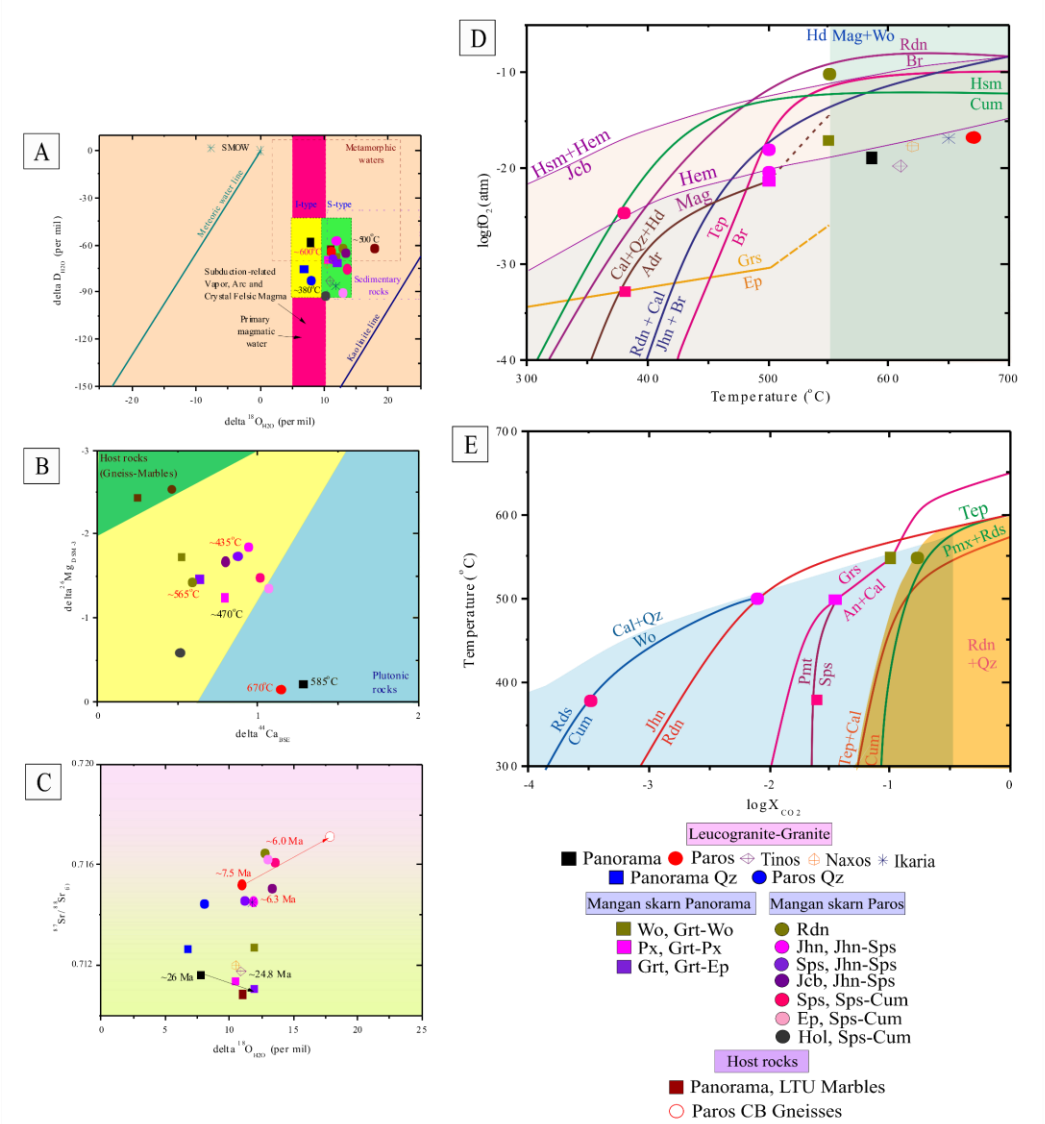

Fig_6

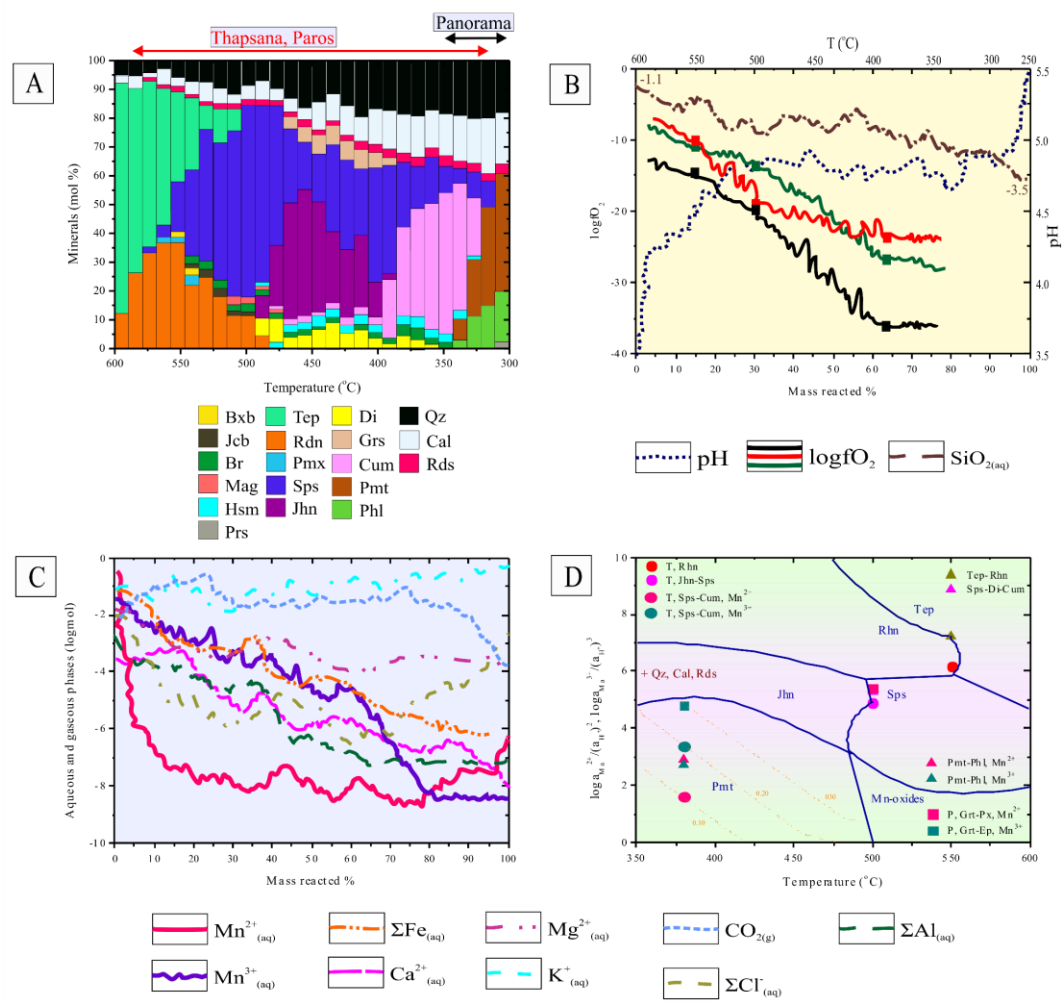

Fig_7

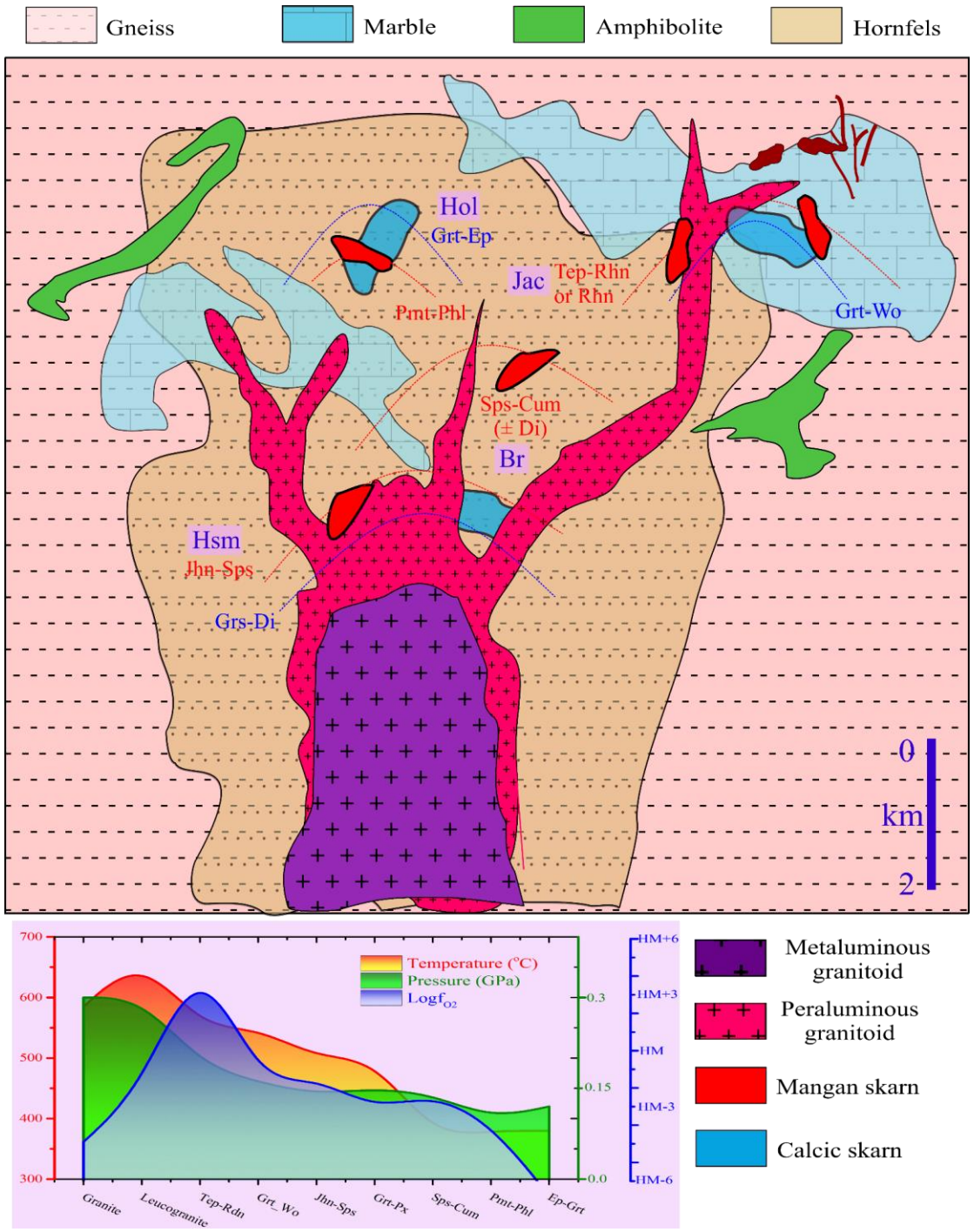

Fig_8

Tombros, S., Kokkalas, S., Triantafyllidis, S., Fitros, M., Tsikos, H., Papadopoulou, L., Voudouris, P., Zhai, D., Skliros, V., Perraki, M., Kappis, K., Spiliopoulou, A., Simos, X., Papavasiliou, J., and Williams-Jones, A. 2023, Genesis of a new type of mangan skarn associated with peraluminous granitoids in Greece: Chemical Geology, v. 623, p. 121369

Electronic Supplementary Material

Tombros, F.S., Triantafyllidis, S., Fitros, M., Kokkalas, S., Papaspyrou, A.M., Tsikos, H., Simos, C.X., Papadopoulou, L., Voudouris, C.P., Zhai, D., Skiros, V., Perraki, M., Kappis, K., Papavasiliou, J., Anthony Williams-Jones and Hatzipanagiotou, K., "Modeling mangan skarn formation related to leucogranites in Greece". Corresponding author e-mail: tombrosfs@gmail.com/, stel@upatras.gr/, Tel.: +302610432500, +326100996349.

ESM Sampling and analytical techniques

Skarns and related Mn-ores were sampled from the mine galleries of Panorama in Drama and Thapsana in Paros Island. For this study, over fifty samples were collected (e.g., PPS1-32, and PTS1-20, e.g., Fig. 2B, E, F) from seven sites representing the different skarn zones (e.g., Grt-Wo, Grt-Px, Grt-Ep zones at Panorama, and Rdn, Jhn-Sps and Sps-Cum zones at Thapsana). The mineralogical and textural features of the skarns were studied in polished thin sections under polarizing optical and scanning electron microscopes (SEM). Mineral microanalyses were performed using a JEOL JSM-6300 SEM equipped with energy dispersive and wavelength spectrometers (EDS and WDS) and INCA software at the Laboratory of Electron Microscopy and Microanalysis, University of Patras, Greece. Operating conditions were accelerating voltage 25 kV and beam current 3.3 nA, with a 4-μm beam diameter. The total counting time was 60 s and dead-time 40%. Standards used for gangue and ore minerals were natural marialite (Cl), tourmaline (B, F), orthoclase (K), diopside (Ca, Si), ilmenite (Ti), rhodonite (Mn), fayalite (Fe), jadeite (Na), forsterite (Mg), corundum (Al), chlorite, epidote, plagioclase and muscovite, natural chalcopyrite, tetrahedrite, tennantite, stibnite, pyrite, sphalerite, galena, hausmannite (Mn^{2+}), manganite (Mn^{3+}), pyrolusite (Mn^{4+}) and synthetic CoNiAs, SnO_2 and CdTe, as well as the native metals Ag, Au, Te and Se. Detection limits are ~ 0.01% and accuracy better that 5% was obtained.

Major and trace element analyses were obtained from a total of eighteen samples, which include ten samples from the different intrusive facies, i.e., Panorama granite and Thapsana leucogranite and eight from the different skarn zones. The geochemical analyses were performed at the ActLabs Ancaster, Ontario. FeO and loss on ignition (LOI) were analyzed by the wet chemical method whereas the other

major element compositions were obtained by FUS-ICP analysis following the method of Taggart et al. (1987). Trace element compositions were measured by inductively coupled plasma mass spectrometry (ICP-MS) techniques of Meier et al. (1994). Detection limits were 0.001 wt. % for MnO and TiO_2 and 0.01 wt. % for the rest of the major elements; 2 ppb for Au; 0.01 ppm for Lu, 0.05 ppm for Pr, Eu and Tm; 0.1 ppm for La, Ce, Nd, Sm, Gd, Tb, Dy, Ho, Er, Yb, Ta, Tl, Th and U; 0.2 ppm for Hf; 0.4 for Bi; 0.5 ppm for Ag, Cs and Sb; 1 ppm for Sc, Be, Co, Ga, Nb, W and Y; 2 ppm for Ba, Sr, Zr and Rb; 5 ppm for Pb, As and V; 10 ppm for Cu; 20 ppm for Cr and Ni, and 30 ppm for Zn. To quantify the Ce and Eu anomalies we have used the equations of Bau et al. (1996) and the normalizing values of McDonough and Sun (1995). In the log(Mn/Fe) versus log(Al/Ca) plot (Fig. 4D) we have added the geochemical data obtained from the mangan skarns (half-filled symbols) in order to illustrate possible differences between parental plutons and skarns.

Microthermometric measurements were performed on 5 doubly polished 50-100 μm thick wafers, on samples containing spessartine from Thapsana (e.g., Jhn-Sps zone), using a LINKAM TMSG600 heating-freezing stage coupled to a ZEISS microscope at the Department of Materials Science, University of Patras, Greece. The stage was calibrated with commercially available standards, e.g., with synthetic inclusions at -56.6ºC (triple point of CO_2), 0.0ºC (melting point of ice) and +374.1ºC (critical point of H_2O). Fluid inclusion assemblages (FIAs) including randomly distributed, primary irregular-shaped, negative-formed inclusions were analyzed, focusing on less deformed crystals. Temperatures were measured with an alumel-chromel thermocouple and freezing-heating rates were maintained between 0.2º and 5ºC/min. Measurements were accurate to ± 0.2°C for T < 100°C, and ± 2°C for T > 100°C. Microthermometric data were reduced using the Q_2, AQSO3e and Bulk software (Bakker, 2003). Prior microthermometric analysis, a subgroup of the fluid inclusions in spessartine were analyzed using Laser Raman spectroscopy. Confocal Raman spectra were obtained with a Renishaw inVia Reflex micro-Raman at the School of Chemical Engineering, Technical University Athens, Greece. Spectra were excited at ambient conditions with the 532 nm line of an Ar^+ laser through an OLYMPUS ×100 short

distance objective, in the spectral range 100 to 4000 cm^{-1}. Two accumulations of 10s each were made to provide the best signal-to-noise ratio. The inclusions were analyzed for the common minerals, gases, mono- and poly-atomic ions and molecules. Spectra were treated with the WIRE 3.4 software using the reference catalog of Frezzotti et al. (2012). The relative concentrations (in mol %) of these species were calculated from the equations of Frezzotti et al. (2012) using the LabSpec software. Temperatures were determined independently based on Raman analyses of the gaseous and liquid phase of fluid inclusions employing the CO_2 and Na-K-, Na-K-Ca- and K-Mg-geothermometers (details in Henley et al., 1984, Tables 3.2 and 5.3), the johannsenite-spessartine (Jhn-Sps zone) and spessartine-epidote (Sps-Cum zone) isotopic pairs (Table 1) using the equations of Zhao et al. (2003), and the garnet-clinopyroxene (Pattison and Newton, 1989), garnet-biotite (Ferry and Spear, 1978 as revised by Holdaway et al., 1997) and two-feldspar (Whitney and Stormer, 1977 as modified by Putirka, 2008) geothermometers.

Qualitative analyses and subsequent solubility calculations included the cations Mn^{2+}, Mg^{3+}, Si^{4+}, Na^{+}, K^{+}, Mg^{2+}, Ca^{2+}, Pb^{+2}, Fe^{2+}, Ba^{2+} B^{3+} and Li^{2+} and the anions CO_3^{2-}, Cl^{-}, HCO_3^{-}, F^{-} and SO_4^{2-} (Table 1b). Only the most suitable trace elements were used. Limitations include certain elements with abundances close to detection limits, concentration ranges, inclusion geometry and homogeneity of the host quartz crystals. The average $\log\Sigma(Na^{+}+K^{+}+Ca^{2+}+Mg^{2+}+Mn^{2+}+Mn^{3+})/Cl^{-}+CO_3^{2-})$ values which represent the ratio of total cationic to anionic charge of the ions contained in the mineralized fluid solution are ~ 1.2. Deviation from the ideal value of 1.0 suggests possible oxidation, the presence of ions that have not been measured (e.g., Mn^{4-}, HS^{-}) and analytical errors. The $\log\Sigma cations/\Sigma anions$ values of all the analyzed spessartine crystals are positive suggesting deficiency of anions. The analytical precision for the analyzed gases was ± 0.1%, whist for the cations and anions the analytical precision was ± 0.01 ppm.

Material of 500-mg splits for stable and Ca, Mg and Rb/Sr isotope studies were obtained from Panorama granite and Thapsana leucogranite (whole rock), as well as coarse-grained pyroxenoids, garnet, pyroxene, epidote, quartz, jacobsite and hollandite (from the Grt-Wo, Grt-Px and Grt-Ep zones in Panorama and Rdn, Jhn-Sps and Sps-Cum zones in Thapsana). Calcite from the host marble in

Panorama and quartz from the gneiss in Thapsana were also analyzed for stable and radiogenic isotopes. All minerals selected were handpicked and checked under a binocular microscope to ensure a purity of > 95%. Isotopic analyses were performed at the Beijing Research Institute of Uranium Geology, China National Nuclear Corporation (CNNC), the Modern Analysis Center, Nanjing University, Nanjing, China, the State Key Laboratory of Geological Processes and Mineral Resources, as well as the Chinese Academy of Geological Sciences (CAGS), Beijing, China. Isotopic compositions of oxygen, hydrogen and carbon were analyzed using a MAT-253 stable isotope ratio mass spectrometer. Oxygen and hydrogen were released using the BrF_5 extraction technique of Friedman and O' Neil (1977), whereas carbon was liberated as CO_2 after Clayton et al. (1972). Hydrogen was released from fluid inclusions by thermal decrepitation. The samples were pre-heated at ⩾ 200 ° C, and then re-heated at ⩾ 500 ° C, and reacted with zinc powder at ~ 400 ° C to generate hydrogen, and by this treatment we have largely eliminated the effects of the secondary fluid inclusions to the hydrogen isotope composition as most of them were decrepitated. The isotopic ratios are reported in standard δ notation per mil relative to SMOW for oxygen and hydrogen and PDB belemnite for carbon. Analytical precision was better than ± 0.2 ‰ for $\delta^{18}O$ and $\delta^{13}C$ and ± 2 ‰ for δD. The AlphaDelta software of Beaudoin and Therrien (2009) was used to compute the isotopic fractionation factors and equilibrium temperatures.

Ca and Mg isotope analyses were performed using a Thermo-Fisher Triton multicollector thermal ionization mass spectrometer, following the method of Husson et al., (2015). Measurements were made yielding a ^{44}Ca beam intensity which was typically between 3.5 and 4.0 V. Mass 43.5 was measured, which records doubly charged ^{87}Sr to correct for Sr interference. Every sample is bracketed by measurements of an in-house high-purity ICP Ca standard. Typical uncertainties $^{44}Ca/^{42}Ca$, $^{44}Ca/^{43}Ca$ and $^{43}Ca/^{42}Ca$ ratios range between 0.01 and 0.02 per mil (all errors are reported at ± 2σ) where $^{40}Ca/^{44}Ca$ = 47.162 and $^{42}Ca/^{44}Ca$ = 0.31221. Similar to Ca, precision of Mg isotope measurements is assessed also by synthetic dolomite standard. For both the Ca and Mg isotopes the analytical accuracy was better than

± 0.01 per mil. Reproducibility for $\delta^{44/42}$Ca was 0.09 per mil (± 2σ) and $\delta^{44/40}$Ca values are reported relative to Bulk Silicate Earth (BSE), while for δ^{26}Mg was 0.1 per mil (± 2σ) relative to DSM-3 (Deep Sea Magnesium).

The same samples were analyzed for their Rb and Sr isotopic compositions using a VG-354 ionization mass spectrometer and the methodology described by Papanastassiou et al. (1978) and DePaolo (1980). The total procedure blanks for Rb and Sr were 20 pg and 50 pg, respectively. The standard used for $^{87}Sr/^{86}Sr$ ratios was NBS987, and so the analytical precision was better than 0.00001 (all errors are reported at ± 1σ). The normalizing factors used to correct for isotopic fractionation of Sr was $^{86}Sr/^{88}Sr$=0.1194. Four granitoid samples were also obtained for zircon U-Pb dating. These comprise the Panorama granite and Thapsana leucogranite (Fig. 1C, D). Zircon crystals were separated using standard heavy-liquid and magnetic techniques, followed by hand-picking under a binocular stereoscope. Prior to LA-ICP-MS analysis, the zircon crystals were imaged by cathodoluminescence. The U-Pb age determinations were carried out using a LA-ICP-MS and the zircon crystals were ablated using an excimer laser ablation system (UP193SS). A laser spot size of 35 μm, laser energy density of 8.5 J/cm^2 and a repetition rate of 10 Hz were applied during analysis. Uranium, Th and Pb concentrations were calibrated by using ^{29}Si as an internal standard and NIST 610 glass as the reference standard. The $^{207}Pb/^{206}Pb$, $^{206}Pb/^{238}U$, $^{207}Pb/^{235}U$ and $^{208}Pb/^{232}Th$ ratios were calculated using the GLITTER 4.4.1 software and corrected for both instrumental mass bias and depth-dependent elemental and isotopic fractionation using Harvard zircon 91500. The zircon standard, TEMORA, was used as a secondary standard to monitor the deviation of the age measurement/calculation (Black et al., 2003). The Rb-Sr isochron and U-Pb Concordia ages were calculated using IsoplotR (Vermeesch, 2018).

ESM References

Anderson J.L., and Smith. D.R., 1995, The effects of temperature and fO2 on the Al-in-hornblende barometer: American Mineralogist, v. 80, p. 549-559.

Armbruster, T., Bonazzi, P., Akasaka, M., Bermanec, V., Chopin, C., Giere, R., Heuss-Assbichler, S., Liebscher, A., Menchetti, S., Pan, Y., and Pasero, M., 2006, Recommended nomenclature of epidote-group minerals: European Journal of Mineralogy, v. 18, p. 551-567.

Bakker, R.J., 2003, Package FLUIDS 1. Computer programs for analysis of fluid inclusion data and for modelling bulk fluid properties: Chemical Geology, v. 194, p. 3-23.

Bau, M., Koschinsky, A., Dulski, P., and Heinz, J., 1996, Comparison of the partitioning behaviours of yttrium, rare-earth elements and titanium between hydrogenic marine ferromanganese crusts and seawater: Geochimica et Cosmochimica Acta v. 60, p. 1709-1725.

Beaudoin, G., and Therrien, P., 2009. Handbook of stable isotope analytical techniques. NY: Elsevier, 2, 1120-1122.

Black, L.P., Kamo, S.L., Allen, C.M., Aleinikoff, J.N., Davis, D.W., Korsch, R.J., and Foudoulis, C., 2003, TEMORA 1: a new zircon standard for Phanerozoic U-Pb geochronology: Chemical Geology, v. 200, p. 155-170.

Clayton, R.N., Muffler, L.J.P., and White, D.E., 1972, Oxygen isotope fractionation study of calcite and silicates of the River Ranch, California: American Journal of Science, v. 266, p. 968-979.

DePaolo, D.J., 1980, Crustal growth and mantle evolution: Inferences from models of element transport and Nd and Sr isotopes: Geochimica et Cosmochimica Acta, v. 44, p. 1185-1196, doi.org/10.1016/0016-7037(80)90072-1.

Ferry, J.M. and Spear, F.S., (1978), Experimental calibration of the partitioning of Fe and Mg between biotite and garnet: Contributions to Mineralogy and Petrology, v. 66, p. 113-117.

Frezzotti, M.L., Tecce, F., and Casagli, A., 2012, Raman spectroscopy for fluid inclusion analysis: Journal of Geochemical Exploration, v. 112, p. 1-20.

Friedman, I., and O' Neil, J.R, 1977, Compilation of stable isotope fractionation factors of geochemical interest: U.S. Geological Survey Professional Paper 440-KK, p. 1-12.

Gnos, E, and Armbruster, T., 2006, Relationship among metamorphic grade, vesuvianite "rod polytypism," and vesuvianite composition: American Mineralogist, v, 91, p. 862-870, doi: https://doi.org/10.2138/am.2006.1973.

Hammarstrom, J.M., and Zen, E-A., 1986, Aluminum in hornblende: an empirical igneous geobarometer: American Mineralogist, v. 71, p. 1297-1313.

Hawthorne, F.C., Oberti, R., Harlow, G.E., Maresch, W.V., Martin, R.F., Schumacher, J.C., and Welch, M.D., 2012. IMA report: Nomenclature of the amphibole supergroup: American Mineralogist, v. 97, p. 2031-2048, doi: 10.2138/am.2012.4276.

Henley, R.W., Truesdell, A.H., and Barton, P.B. Jr. 1984, Fluid-mineral equilibria in hydrothermal systems: Reviews in Economic Geology, v. 1, p. 267.

Hezel, D.C., Kalt, A., Marschall, H.R., Ludwig, T., and Meyer, H.P., 2011, Major-element and Li, Be compositional evolution of tourmaline in an S-type granite-pegmatite system and its country rocks: An example from Ikaria, Aegean Sea, Greece: The Canadian Mineralogist, v. 49, p. 321-340, doi:10.3749/canmin.49.1.321.

Holdaway, M.J., Mukhopadhyay, B., Dyar, M.D., Guidotti, C.V., and Dutrow, B.L., 1997, Garnet-biotite geothermometry revised: New Margules parameters and a natural specimen data set from Maine: American Mineralogist, v. 82, p. 582-595.

Husson, J. M., Higgins, J.A., Maloof, A.C., and Schoene, B., 2015, Ca and Mg isotope constraints on the origin of Earth's deepest d13C excursion: Geochimica et Cosmochimica Acta, v. 160, p. 243-266, doi:10.1016/j.gca.2015.03.012.

Johnson, M.C., and Rutherford, M.J., 1989, Experimental calibration of the aluminum-in-hornblende geobarometer with application to Long Valley caldera (California) volcanic rocks: Geology, v. 17 (9), p. 837-841.

Jones, C.E., Tarney, J., Baker J.H., and Gerouki F., 1992, Tertiary granitoids of Rhodope, northern Greece: magmatism related to extensional collapse of the Hellenic Orogen: Tectonophysics, v. 210, p. 295-314.

Kevrekidis E., St. Seymour, K., Tombros, S.F., Zhai, D., Liu, J., and Zouzias, D., 2015, The Agios Georgios argentiferous galena deposit on Antiparos Island, Cyclades, Hellas, and its relationship

to the Paros leucogranite: Neues Jahrbuch für Mineralogie Abhandlungen-Journal of Mineralogy and Geochemistry, v. 192, p. 1-23, doi:10.1127/njma/2015/0283.

Krogh Ravna, E., 2000, The garnet–clinopyroxene Fe^{2+}-Mg geothermometer: an updated calibration: Journal of Metamorphic Geology, v. 18, p. 211-219.

Mastrakas, N., and St. Seymour, K., 2000, Geochemistry of Tinos granite: A window to the Miocene microplate tectonics of the Aegean region: Neues Jarhbuch für Mineralogie Abhandlungen v. 175, p. 295-315.

McDonough, W.F., and Sun, S.S., 1995. The composition of the Earth: Chemical Geology, v. 120, p. 223-253, https://doi.org/10.1016/0009-2541(94)00140-4.

Meier, A.L., Grimes, D.J., and Ficklin, W.H., 1994, Inductively coupled plasma mass spectrometry - a powerful analytical tool for mineral resource and environmental studies: U.S. Geological Survey Circular 1103-A, p. 67-68.

Morimoto, N., 1989, Nomenclature of pyroxenes: Canadian Mineralogist, v. 27, p. 143-156, https://doi.org/10.2465/minerj.14.198.

Papanastassiou, D.A., De Paolo, D.J., and Wasserburg, G.J., 1977, Rb-Sr and Sm-Nd chronology and genealogy of mare basalts from the Sea of Tranquility: Lunar and Planetary Science Conference Proceedings, v. 8, p. 1639-1672, https://ui.adsabs.harvard.edu/abs/1977LPSC.8.1639P.

Pattison, D.R.M., and Newton, R.C., 1989, Reversed experimental calibration of the garnet-clinopyroxene Fe-Mg exchange thermometer: Contribution to Mineralogy and Petrology, v. 101, p. 87-103.

Pe-Piper, G., 2000, Origin of S-type granites coeval with I-type granites in the Hellenic subduction system, Miocene of Naxos, Greece: European Journal of Mineralogy, v. 12, p. 859-875, doi: https://doi.org/10.1127/0935-1221/2000/0012-0859.

Putirka, K.D., 2008, Thermometers and barometers for volcanic systems: Reviews in Mineralogy and Geochemistry, v. 69, p. 61-120, doi.org/10.2138/rmg.2008.69.3.

Schmidt, M.W., 1992, Amphibole composition in tonalite as a function of pressure: An experimental calibration of the Al-in-hornblende barometer: Contributions to Mineralogy and Petrology, v. 110, p. 304-310.

Spencer, K.J., and Lindsley, D.H., 1981, A solution model for coexisting iron-titanium oxides: American Mineralogist v. 66, p. 1189-1201.

Taggart, J.E., Jr., Lindsey, J.R., Scott, B.A., Vivit, D.V., Bartel, A.J., and Stewart, K.C., 1987, Analysis of geological materials by wavelength-dispersive X-ray fluorescence spectrometry: U.S. Geological Survey Professional Paper 1770, p. 1-19.

Thompson, R.M., Yang, H., and Downs, R.T., 2016, Ideal wollastonite and the structural relationship between the pyroxenoids and pyroxenes: American Mineralogist, v. 101, p. 2544-2553, https://doi.org/10.2138/am-2016-5683.

Tian, Y., Etschmann, B.E., Mei, Y., Grundler, P., Testemale, D., Hazemann, J.-L., Elliott, P., Ngothai, Y., and Brugger J., 2014, Speciation and thermodynamic properties of Manganese (II) chloride complexes in hydrothermal fluids: in situ XAS study: Geochimica et Cosmochimica Acta, v. 129, p. 77-95.

Uchida, E., Endo, S., and Makino, M., 2007, Relationship between solidification depth of granitic rocks and formation of hydrothermal ore deposits: Resource Geology, p. 57, p. 47-56.

Whitney, D., and Evans, B., 2010, Abbreviations for names of rock-forming minerals: American Mineralogist, v. 95, p. 185-187.

Whitney, J.A., and Stormer, J.C., 1977, Two-feldspar geothermometry, geobarometry in mesozonal granitic intrusions: Three examples from the Piedmont of Georgia: Contribution to Mineralogy and Petrology v. 63, p. 51-64, https://doi.org/10.1007/BF00371675.

Zen, E., 1985, Implications of magmatic epidote-bearing plutons on crustal evolution in the accreted terranes of northwestern North America: Geology v. 13, p. 266-269, doi.org/10.1130/0091-7613(1985)13.

Zhao, Y.M., Dong, Y., Li, D., and Bi, C., 2003, Geology, mineralogy, geochemistry, and zonation of the Bajiazi dolostone-hosted Zn-Pb-Ag skarn deposit, Liaoning Province, China: Ore Geology Reviews, v. 23, p. 153-182, doi.org/10.1016/S0169-1368(03)00034-9.

Vermeesch, P., 2018, IsoplotR: a free and open toolbox for geochronology: Geoscience Frontiers, v. 9, p.1479-1493, doi: 10.1016/j.gsf.2018.04.001.

ESM Tables

Electronic Supplementary Material, Table 1. Representative electron microprobe analyses of pyroxenoids from the skarn of Panorama, Drama and Thapsana, Paros (all results in wt. %).

Mineral: Wollastonite[1], Vessuvianite[2], Rhodonite [3]						
Locality and exoskarn-type	Panorama calcic				Thapsana mangan	
Mineralogical Zone	Wo - Grt				Rhd (± Ves)	
Analyzed Spots	Core[1]	Rim[1]	Core[2]	Rim[2]	Rhd[3]	Ves[2]
SiO_2	51.16	51.63	35.76	36.87	48.00	34.39
TiO_2	0.00	0.00	0.05	0.00	0.22	0.00
Al_2O_3	0.00	0.00	14.92	9.45	0.00	14.52
FeO	0.00	0.00	8.11	16.54	0.89	9.98
MnO	0.00	0.00	2.38	0.95	41.23	7.33
MgO	0.87	1.06	0.26	0.21	2.72	0.00
CaO	47.42	47.34	35.28	36.41	5.36	33.58
Na_2O	0.00	0.00	0.35	0.00	0.00	0.00
K_2O	0.00	0.00	0.10	0.00	0.00	0.00
Total	99.45	100.03	97.21	100.43	98.42	99.80
	Nº of atoms based on					
Si^{total}	5.99	6.04	19.32	19.91	10.14	17.27
Ti	0.00	0.00	0.02	0.00	0.03	0.00
Fe^{3+}	0.00	0.00	0.00	0.00	0.14	0.00
Fe^{2+}	0.00	0.00	3.66	7.47	0.00	4.19
Al^{total}	0.00	0.00	9.50	6.02	0.00	8.59
Mn^{2+}	0.09	0.11	0.21	0.03	7.11	0.11
Mn^{3+}	0.00	0.00	0.98	0.39	0.27	3.07
Mg	0.00	0.00	0.21	0.17	0.86	0.00
Ca	5.94	5.93	20.42	21.07	1.21	18.06
Na	0.00	0.00	0.37	0.00	0.00	0.00
K	0.00	0.00	0.07	0.00	0.00	0.00
Total	12.02	12.08	54.65	55.08	19.75	51.23
O (normalized)	18.00	18.00	78.00	78.00	30.00	78.00
	Solid solution classification (%)					
Wo	98.57	98.26	-	-	-	-
En	0.00	0.00	-	-	-	-
Fs	1.43	1.74	-	-	-	-
$MnSiO_3$	0.00	0.00	-	-	76.96	-
$CaSiO_3$	0.00	0.00	-	-	12.61	-
$MgSiO_3$	0.00	0.00	-	-	8.97	-
$FeSiO_3$	1.43	1.74	-	-	1.46	-

[1]Wollastonite and [3]rhodonite formulae have been calculated normalized on 18 and 30 oxygens respectively, based on the formula MXO_3 (M = Mg, Ca, and Mn, X = Si, Al^{IV}, C, Ge and B) after Thompson et al. (2016).

[2]Vessuvianite formula has been calculated normalized on 78 oxygens, based on the formula $X_{19}Y_{13}Z_{18}T_{0\text{-}5}O_{68}W_{11}$ (X = Ca, REE, U, Th, Pb, Sb, K, Na, Ba and Sr, Y = Al, Mg, Fe^{3+}, Fe^{2+}, MnO^{2+}, MnO^{3+}, Ti, Zn, Cr and Cu^{2+} , T = B, Al, Fe^{3+}, MnO^{3+} and Mg, Z = Si and W = OH, F, O and Cl) after Gnos and Armbruster (2006). Vesuvianite from Thapsana belongs to the manganvesuvianite variety (see Gnos and Armbruster, 2006). Abbreviations are after Whitney and Evans (2010).

Electronic Supplementary Material, Table 2. Representative electron microprobe analyses of pyroxene from the skarn of Panorama, Drama and Thapsana, Paros (all results in wt. %).

Mineral: Pyroxenes[1]								
Locality and exoskarn-type	Panorama calcic						Thapsana mangan	
Mineralogical Zone	Wo - Grt		Grt - Px				Jhn - Sps	
Analyzed Spots	Core	Rim[A]	Core	Rim[A]	Core	Rim[A]	Core	Rim[A]
SiO_2	54.67	52.53	52.57	51.96	51.72	52.54	48.80	50.97
Al_2O_3	1.12	0.54	0.75	0.51	0.32	0.28	11.90	12.92
FeO	4.06	4.87	8.91	9.61	9.35	8.80	0.98	0.00
MnO	0.33	1.02	2.15	2.59	3.31	2.21	27.06	26.41
MgO	15.06	15.30	11.18	11.02	11.23	11.80	0.96	2.60
CaO	24.77	25.14	24.33	24.33	23.85	24.49	0.00	3.17
Na_2O	0.38	0.14	0.10	0.07	0.16	0.17	0.85	0.00
K_2O	0.11	0.00	0.13	0.08	0.16	0.00	8.94	3.56
Total	100.50	99.61	100.12	100.17	100.10	100.29	100.00	99.63
	Nº of atoms based on							
Si^{total}	1.99	1.94	2.00	1.98	1.97	2.00	1.94	2.02
Fe^{total}	0.12	0.15	0.28	0.30	0.30	0.28	0.03	0.00
Al^{total}	0.05	0.02	0.03	0.02	0.01	0.01	0.56	0.61
Mn^{2+}	0.01	0.02	0.07	0.08	0.11	0.07	0.91	0.89
Mn^{3+}	0.00	0.01	0.00	0.00	0.00	0.00	0.00	0.00
Mg	0.82	0.84	0.64	0.63	0.64	0.67	0.06	0.15
Ca	0.97	0.99	0.99	0.99	0.97	1.00	0.00	0.13
Na	0.03	0.01	0.01	0.01	0.01	0.01	0.06	0.00
K	0.01	0.00	0.01	0.00	0.01	0.00	0.45	0.18
O (normalized)	6.00	6.00	6.00	6.00	6.00	6.00	6.00	6.00
	Solid solution classification (%)							
En/Hd	42.63	41.66	50.15	49.47	48.32	49.48	0.00	11.46
Fs/Di	6.98	9.12	48.11	46.77	47.49	49.76	11.38	26.16
Wo/Jhn	50.40	49.22	1.74	3.75	4.19	0.76	88.62	62.39
	Temperature estimate							
T^A (ºC)	-	524	-	-	-	494	-	482

[1]Pyroxene formulae have been calculated normalized on 6 oxygens, based on the formula $M_2M_1Z_2O_6$ (M_2 = Na, Ca, Fe^{2+}, Mn and Mg, M_1 = Mn, Fe^{2+}, Fe^{3+}, Mg, Cr, Al^{IV}, and Ti and Z = Si and Al^{VI}, where $M_2>M_1$) after Morimoto (1989) and Thompson et al. (2016). Abbreviations are after Whitney and Evans (2010).

[A]Application on the garnet-**clino**pyroxene geothermometer of Pattison and Newton (1989) which fits best for skarns. **The calcium, magnesium and manganese** distribution between clinopyroxene and garnet has been calibrated by Krogh Ravna (2000). In their calibration, ferric iron in the garnet has been calculated on a stoichiometric basis assuming Z = Si = 3.0, and recalculating ΣXY = 5.0, with ΣX = (Ca + Mn + Fe^{2+}+ Mg) = 3.0 and ΣY = (Fe^{3+} + Al + Cr) = 2.0. For the co-existing clinopyroxene, which all are Na- and Al-poor, Fe^{2+}/Fe^{3+} has been estimated by assuming no jadeite component. Thus, Al has been distributed equally on the four and six coordination sites and Fe^{3+} = Na. The solid solution model for clinopyroxene assumes equal partitioning of Fe and Mg atoms between M_2 and M_1 sites and ignores possible cross-site interactions. Also, Mg# is supposed to be equal in both M_1 and M_2, and mixing on the tetrahedral site of cpx is assumed to be ideal and coupled to octahedral site substitutions. The main limitations of the pyroxene-garnet geothermometer are that **the clinopyroxene and garnet crystals (herein their rims) are in equilibrium and** minimum compositional uncertainties must be considerably greater than 0.01Mg# values of analytical error. The number of Ca cations in the structural formulae of garnet and clinopyroxene was normalized on 12 and 6 oxygens, respectively, and $Fe_{total} = Fe^{2+}$. For Panorama, the X^{Grt}_{Ca}, X^{Grt}_{Fe} and X^{Grt}_{Mg} values for garnet range from 0.98-1.00, 0.05-0.10 and 0.00-0.01 and X^{Px}_{Ca}, X^{Px}_{Fe} and X^{Px}_{Mg} values for clinopyroxene range from 0.51-0.52, 0.14-0.16, and 0.32-0.35, respectively and the $\ln K_D$ values are 100. Application on the clinopyroxene-garnet geothermometer of Pattison and Newton (1989) as re-calibrated by Krogh Ravna (2000) using an average calculated pressure of ~150 MPa gave temperatures ranging from ~ 470º to ~ 500ºC for the Wo-Grt and Grt-Pyx zones in Panorama (524ºC and average of 499ºC and st.d. of 5.6ºC). For Thapsana, the X^{Grt}_{Ca}, X^{Grt}_{Fe} and X^{Grt}_{Mg} values for garnet range from 0.50-0.52, 0.79-0.80 and 0.21-0.23 and X^{Px}_{Ca}, X^{Px}_{Fe} and X^{Px}_{Mg} values for clinopyroxene are 1.00 and 0.00, respectively for the same $\ln K_D$ values. Using an average calculated pressure of ~150 MPa the obtained temperatures range between ~ **440º to ~ 510ºC**

for the Jhn-Sps zone (average of 501ºC and st.d. of 18.3ºC). For our calculations we have used the GrtCpxThermoV5 excel sheet utilizing the equation of Krogh Ravna (2000).

Electronic Supplementary Material, Table 3. Representative electron microprobe analyses of garnet from the skarn of Panorama, Drama and Thapsana, Paros (all results in wt. %).

Mineral: Garnet[1]											
Locality and exoskarn-type Mineralogical Zone		Panorama calcic						Thapsana mangan			
		Wo - Grt		Grt - Px		Grt - Ep		Jhn - Sps		Sps - Cum	
Analyzed Spots	Granite[B]	Core	Rim	Core	Rim[A]	Core	Rim	Core	Rim	Core	Rim[A]
SiO_2	35.69	37.49	37.29	38.74	38.82	37.91	37.58	38.88	38.64	38.84	38.49
TiO_2	0.07	0.04	0.23	0.17	1.12	1.31	1.51	0.00	0.00	0.00	0.00
Al_2O_3	19.56	9.82	5.91	22.55	21.72	12.04	12.64	17.99	18.77	19.93	18.76
FeO	22.82	16.87	21.55	0.00	0.53	12.77	11.45	3.20	2.49	1.38	1.72
MnO	17.96	0.59	0.56	4.65	7.43	2.24	3.10	33.61	34.16	31.61	33.37
MgO	0.41	0.23	0.24	0.00	0.23	0.00	0.28	1.59	1.12	1.67	1.26
CaO	2.84	34.68	34.52	32.86	29.54	33.54	32.29	4.73	4.82	6.56	6.38
Na_2O	0.00	0.00	0.00	0.15	0.00	0.00	0.35	0.00	0.00	0.00	0.00
Cr_2O_3	0.00	0.00	0.00	0.00	0.00	0.44	0.76	0.00	0.00	0.00	0.00
Total	99.35	99.72	100.30	99.12	99.39	100.25	99.96	100	100	99.99	99.98
						Nº of atoms based on					
Si^{total}	2.96	3.00	3.01	2.96	2.98	2.99	2.97	3.13	3.12	3.10	3.10
Ti	0.04	0.00	0.01	0.01	0.06	0.08	0.09	0.00	0.00	0.00	0.00
Fe^{total}	2.17	1.13	1.46	0.01	0.04	0.84	0.76	0.21	0.16	0.10	0.11
Al^{total}	1.93	0.93	0.56	2.03	1.96	1.12	1.18	1.71	1.78	1.87	1.78
Mn^{2+}	1.13	0.00	0.04	0.00	0.00	0.00	0.00	2.27	2.29	2.11	2.21
Mn^{3+}	0.12	0.00	0.00	0.00	0.00	0.00	0.00	0.02	0.04	0.02	0.06
Mg	0.05	0.03	0.00	0.00	0.03	0.00	0.03	0.19	0.13	0.20	0.15
Ca	0.24	2.97	2.99	2.69	2.43	2.83	2.74	0.41	0.42	0.56	0.55
O	12.00	12.00	12.00	12.00	12.00	12.00	12.00	12.00	12.00	12.00	12.00
						Solid solution classification (%)					
Alm	38.99	0.00	0.00	0.00	0.30	0.00	0.00	0.00	0.00	0.00	0.00
Adr	4.49	49.00	67.40	0.00	0.00	36.30	32.30	7.20	4.50	1.30	5.60
Grs	5.11	48.50	30.00	89.80	82.40	56.60	56.20	2.80	7.40	16.70	8.60
Prp	0.79	1.00	1.10	0.00	0.90	0.00	1.20	6.90	4.80	7.0	5.30
Sps	50.62	1.50	1.50	10.20	16.40	5.50	7.60	83.10	83.30	75.0	80.50
Uv	0.00	0.00	0.00	0.00	0.00	1.50	2.60	0.00	0.00	0.00	0.00
T^B (ºC)	585	-	-	-	-	-	-	-	-	-	369

[1]Garnet formulae have been calculated normalized on 12 oxygens and 8 cations, based on the formula $X_3Y_2Z_3O_{12}$ (X = Ca^{2+}, Mn^{2+}, Fe^{2+}, Mg^{2+}, Na^{1+}, Y = Al^{IV}, Fe^{3+}, Ti and Cr^{3+}, and Z = Si and Al^{VI}, where X > Y, with Fe^{2+}/Fe^{3+} calculated assuming full site occupancy, and for high Cr and Mn contents MnO corrected for Cr interference). For our calculations we have used the excel sheet GNTCALC provided by GabbroSoft. Abbreviations are after Whitney and Evans (2010).

[A]Application on the garnet-**clino**pyroxene geothermometer of Pattison and Newton (1989).

[B]Application on the garnet-biotite Fe-Mg exchange thermometer of Ferry and Spear (1978) as revised by Holdaway et al. (1997). The Fe^{2+} and Mg^{2+} ions partitioning in the garnet-biotite geothermometer is depended on the temperature and pressure changes. It is assumed that mixing and substitution in garnet and biotite between Fe-Mg is ideal or nearly ideal, $Al^{Bt} = 0.5 \cdot (Al - 1)$ and Fe^{3+} in biotite occurs in the octahedral site. The main limitation is that pressure ranges from 1 to 4.5 kbar. Application on the garnet-biotite geothermometer of Ferry and Spear (1978) using a calculated pressure of ~300 MPa gave temperatures ~ 585º for the Panorama granite. For Thapsana. Using an average calculated pressure of ~150 MPa the obtained temperatures for the Sps-Cum zone are ~ 370**ºC. W**e have calculated the temperature of formation of the accessory spessartine from the peraluminous granites-to-leucogranites. The estimated temperatures are 585**º (Panorama granite),** 610**º (Tinos),** 620**º (Naxos),** 650**º (Ikaria) and** 670**ºC (Paros) at pressure of 200** MPa **using our mineralogical data, as well as the**

already published from Jones et al. (1992); Mastrakas and Seymour (2001); Pe-Piper (2000); Hezel et al. (2011); Kevrekidis et al. (2015)**.**

Electronic Supplementary Material, Table 4a. Representative electron microprobe analyses of plagioclase from the skarn of Panorama, Drama and Thapsana, Paros (all results in wt. %).

Mineral: Plagioclase[1]									
Locality and exoskarn-type	Panorama calcic						Thapsana mangan		
Mineralogical zone	Grt - Px						Sps - Cum		
Analyzed Spots	Rim[C]	Int	Int	Int	Int	Core	Rim[C]	Int	Core
SiO_2	55.12	56.02	56.19	55.67	56.05	56.37	64.45	64.38	64.02
Al_2O_3	28.39	27.76	27.77	27.93	27.64	27.43	23.47	22.61	22.47
FeO	0.32	0.23	0.12	0.39	0.00	0.08	0.00	0.00	0.00
MnO	0.00	0.00	0.00	0.00	0.00	0.00	2.67	5.12	6.79
CaO	10.83	10.07	10.03	10.44	9.77	9.61	4.94	3.77	3.72
Na_2O	5.45	5.60	5.55	5.64	5.52	5.72	2.38	2.79	2.01
K_2O	0.00	0.10	0.00	0.00	0.43	0.03	1.09	0.13	0.00
BaO	0.00	0.00	0.00	0.00	0.00	0.00	0.00	0.00	0.00
Total	100.11	99.78	99.66	100.07	99.41	99.24	99.00	98.80	99.01
	Nº of atoms based on								
Si	2.48	2.52	2.53	2.51	2.53	2.55	2.85	2.86	2.85
Al	1.51	1.47	1.47	1.48	1.47	1.46	1.22	1.19	1.18
Fe^{3+}	0.01	0.01	0.01	0.02	0.00	0.00	0.00	0.00	0.00
Mn	0.00	0.00	0.00	0.00	0.00	0.00	0.10	0.19	0.26
Ca	0.52	0.49	0.49	0.50	0.47	0.46	0.23	0.18	0.18
Na	0.40	0.49	0.48	0.49	0.48	0.50	0.20	0.24	0.17
K	0.00	0.01	0.00	0.00	0.03	0.00	0.06	0.01	0.00
Ba	0.00	0.00	0.00	0.00	0.00	0.00	0.00	0.00	0.00
O	8.00	8.00	8.00	8.00	8.00	8.00	8.00	8.00	8.00
	Solid solution classification (%)								
Or	0.0	0.6	0.0	0.0	2.5	0.2	10.3	1.2	0.0
Ab	47.7	49.9	50.0	49.4	49.3	51.8	34.0	38.8	28.6
An	52.3	49.5	50.0	50.6	48.2	48.1	55.7	60.0	71.4
Cn	0.0	0.0	0.0	0.0	0.0	0.0	0.0	0.0	0.0
	Temperature estimate								
T (ºC)	375	-	-	-	-	-	376	-	-

Electronic Supplementary Material, Table 4b. Representative electron microprobe analyses of alkali feldspar from the skarn of Panorama, Drama and Thapsana, Paros (all results in wt. %).

Mineral: alkali feldspar[2]										
Locality and exoskarn-type	Panorama calcic						Thapsana mangan			
Mineralogical zone	Grt - Px						Sps - Cum			
Analyzed Spot	Rim[C]	Int	Int	Int	Int	Core	Rim[C]	Int	Int	Core
SiO_2	63.82	63.97	64.52	64.65	64.96	64.93	63.69	63.39	63.38	64.00
Al_2O_3	18.22	18.38	18.71	18.35	18.28	18.55	18.29	18.33	18.59	18.29
FeO	0.34	0.38	0.00	0.03	0.13	0.00	0.00	0.00	0.00	0.00
MnO	0.00	0.00	0.00	0.00	0.00	0.00	1.21	0.86	0.95	1.03
CaO	0.14	0.33	0.33	0.21	0.00	0.25	0.27	0.48	0.03	0.28
Na_2O	0.22	0.57	1.11	0.69	0.71	0.6	0.77	0.26	0.59	0.83
K_2O	16.00	15.48	14.8	15.66	15.75	15.89	15.62	15.68	15.69	15.19
BaO	0.98	0.76	0.61	0.04	0.33	0.02	0.17	0.92	0.74	0.39
Total	99.72	99.87	100.08	99.63	100.16	100.24	100.02	99.92	99.97	100.01
	Nº of atoms based on									
Si	2.98	2.98	2.98	2.99	3.00	2.99	2.97	2.97	2.96	2.98
Al	1.00	1.01	1.02	1.00	0.99	1.01	1.00	1.01	1.02	1.00
Fe^{3+}	0.01	0.02	0.00	0.00	0.01	0.00	0.00	0.00	0.00	0.00
Mn	0.00	0.00	0.00	0.00	0.00	0.00	0.05	0.03	0.04	0.04
Ca	0.01	0.02	0.02	0.01	0.00	0.01	0.01	0.02	0.00	0.01
Na	0.02	0.05	0.10	0.06	0.06	0.05	0.07	0.02	0.05	0.08
K	0.95	0.92	0.87	0.93	0.93	0.93	0.93	0.94	0.94	0.90
Ba	0.02	0.01	0.01	0.00	0.01	0.00	0.00	0.04	0.01	0.01
O	8.00	8.00	0.01	0.00	0.01	0.00	0.00	0.02	0.01	0.01
	Solid solution classification (%)									
Or	95.5	91.8	87.3	92.7	93.0	93.4	87.4	90.5	89.8	86.8
Ab	2.0	5.1	10	6.2	6.4	5.4	6.5	2.3	5.1	7.2
An	0.7	1.6	1.6	1.0	0.0	1.2	5.8	5.6	3.8	5.3
Cn	1.8	1.4	1.1	0.1	0.6	0.0	0.3	1.6	1.3	0.7

[1,2]Plagioclase and alkali feldspar formulae were calculated normalized on 8 oxygens, based on the formula XZ_4O_8 (X = Na and Ca, and Z = Si and Al).

[C]Application on the two-feldspar geothermometer of Whitney and Stormer (1977) as modified by Putirka (2008). The two-feldspar geothermometer is based on the distribution of the albite component between plagioclase and alkali feldspar crystals during crystallization from a liquid or vapor. It can be expressed by the reaction: $NaAlSi_3O_{8(alkali\text{-}feldspars)} = NaAlSi_3O_{8(plagioclase)}$. The basic limitations in using the two-feldspar geothermometer are that chemical equilibrium between alkali

feldspars and plagioclases must be attained and the presence of other mineral phases (e.g., feldspathoids) is negligible. There is a serious discrepancy at very high-albite contents, and lastly, the vapor phase pressure ranges from 2 to 10 kbars (Whitney and Stormer, 1977). The basic assumptions of the two-feldspar geothermometer are that assumption that the inter-crystalline coupled CaAl-(Na,K)Si exchange was slow and potassium component has no effect on the plagioclase and the calcium component on the alkali feldspar (Whitney and Stormer, 1977; Putirka, 2008). For Panorama the analyzed Ab contents in the plagioclase rims in equilibrium with orthoclase are $Ab_{47.7}$ and $Ab_{2.0}$, respectively. The obtained temperature based on the application on the two-feldspar geothermometer of Whitney and Stormer (1977) is 383.3º ± 10ºC. For Thapsana the analyzed Ab contents in the plagioclase rims in equilibrium with orthoclase are $Ab_{34.0}$ and $Ab_{6.5}$, respectively, and the obtained is estimated at 372.6º ± 5ºC. For our calculations we have used the excel sheet two-feldspar geothermometer of Putirka (2008).

Tombros, S., Kokkalas, S., Triantafyllidis, S., Fitros, M., Tsikos, H., Papadopoulou, L., Voudouris, P., Zhai, D., Skliros, V., Perraki, M., Kappis, K., Spiliopoulou, A., Simos, X., Papavasiliou, J., and Williams-Jones, A. 2023, Genesis of a new type of mangan skarn associated with peraluminous granitoids in Greece: Chemical Geology, v. 623, p. 121369

Electronic Supplementary Material, Table 5. Representative electron microprobe analyses of biotite/phlogopite and amphibole from the skarn of Panorama, Drama and Thapsana, Paros (all results in wt. %).

Mineral: Biotite[1], Ampibole[2]									
Locality and exo-skarn type				Panorama calcic			Thapsana mangan		
Mineralogical Zone				Grt - Ep			Sps - Cum		
Analyzed Spots	Granite[1,B]	Core[2,D]	Int[2,D]	Int[2,D]	Rim[2,D]	Core[2,B]	Rim[2,D]	Core[1, E]	Rim[1, E]
SiO_2	46.41	47.64	45.44	47.72	45.25	51.62	50.22	50.63	48.80
TiO_2	0.99	1.36	1.3	1.38	1.77	0.00	0.00	0.00	0.51
Al_2O_3	11.82	8.14	7.37	6.75	7.85	12.57	15.00	13.24	11.90
MnO	2.11	0.61	0.91	0.89	1.24	1.99	2.84	1.28	1.81
Mn_2O_3	0.00	0.00	0.00	0.00	0.85	0.00	0.00	0.00	0.00
FeO	22.99	14.97	18.28	16.42	17.56	0.88	0.00	0.61	0.98
MgO	6.39	12.03	11.14	10.93	9.80	27.92	25.07	28.20	27.06
CaO	0.11	11.27	12.51	11.97	12.21	1.89	3.75	0.00	0.00
Na_2O	0.36	1.67	0.60	1.19	0.91	0.00	0.00	0.00	0.00
K2O	9.32	0.72	0.76	0.66	1.16	2.91	2.74	6.05	8.94
H_2O	0.00	0.00	0.00	0.00	0.00	0.00	0.00	0.00	0.00
F	0.00	0.00	0.00	0.00	0.00	0.00	0.00	0.00	0.00
Cl	0.00	0.00	0.00	0.00	0.00	0.00	0.00	0.00	0.00
$O=F,Cl^{calc}$	0.00	0.00	0.00	0.00	0.00	0.00	0.00	0.00	0.00
Total	100.00	98.41	98.31	97.91	97.75	99.78	99.62	100.01	100.00
				Nº of atoms based on					
Si	6.53	6.70	7.49	7.65	7.43	6.85	6.70	6.47	6.40
Ti	0.11	0.00	0.00	0.00	0.00	0.00	0.00	0.00	0.05
Al^{IV}	1.36	1.30	0.51	0.35	0.57	1.15	1.30	1.53	1.60
Z^{total} (1), T^{total}(2)	8.00	8.00	8.00	8.00	8.00	8.00	8.00	8.00	8.00
Al^{VI}	0.74	0.05	0.25	0.11	0.01	0.08	0.05	0.00	0.00
Fe^{2+}(1), Fe^{3+}(2)	2.78	0.00	0.11	0.13	0.13	0.00	0.00	0.07	0.11
Mn^{3+}	0.23	0.00	0.43	0.29	0.60	0.00	0.00	0.00	0.00
Mg	1.25	3.95	4.22	4.11	4.26	4.19	3.95	5.37	5.29
Y^{total} (1), C^{total}(2)	5.00	5.00	5.00	5.00	5.00	5.00	5.00	6.04	5.88
Mn^{2+}	0.01	0.32	0.27	0.42	0.38	0.22	0.32	0.14	0.20
Mg	0.00	1.04	0.28	0.00	0.04	1.33	1.04	0.00	0.00
Ca	0.02	0.54	1.01	1.19	1.24	0.27	0.54	0.00	0.00
Na	0.09	0.00	0.44	0.39	0.34	0.00	0.00	0.00	0.00
B^{total}	0.00	1.89	2.00	1.99	2.00	1.93	1.89	0.00	0.00
K	1.56	0.47	0.00	0.07	0.00	0.49	0.47	0.97	0.95
Na	0.00	0.00	0.18	0.14	0.17	0.00	0.00	0.00	0.00
X^{total} (1), A^{total}(2)	1.56	0.47	0.18	0.21	0.17	0.49	0.47	0.97	0.95
H_2O	1.00	1.00	1.00	1.00	1.00	1.00	1.00	1.00	1.00
OH	2.00	2.00	2.00	2.00	2.00	2.00	2.00	2.00	2.00
Total	15.09	15.36	15.18	15.21	15.17	15.42	15.36	15.01	14.84

O	22.00	22.00	22.00	22.00	22.00	22.00	22.00	22.00	22.00
Species	Bt	Cum	Mg-Mn-Hlb	Mg-Mn-Hlb	Mg-Mn-Hlb	Cum	Cum	Phl	Phl
$Mg/(Mg+Fe^2)$	0.33	-	-	-	-	-	-	0.99	0.98
P (MPa) based on Anderson and Smith (1995); Uchida et al. (2007).	302		131	112	124	189	99	139	122

[1]Biotite formulae were calculated normalized on 22 oxygens, based on the formula $IM_{2\text{-}3}\square_{1\text{-}0}T_4O_{10}A_2$ (I = Cs, K, Na, NH_4, Rb, Ba and Ca, M = Li, Fe^{2+}, Fe^{3+}, Mg, Mn^{2+}, Mn^{3+}, Zn, Al^{VI}, Cr, V and Ti, □ = Vacancy, T = Be, Al^{IV}, B, Fe^{3+} and Si, and A = Cl, F, OH, O and S, Rieder et al., 1998).

[2]Amphibole formulae were calculated normalized on 23 oxygens, based on the formula $AB_2{}^{VI}C_5{}^{IV}T_8O_{22}W_2$ (A = Ca, Li, Na, Pb and K, and B = Fe^{2+}, Mn^{2+}, Mg, Li, Ca, Sr and Na, C = Ti^{4+}, Cr, Al^{VI}, Sc, V, Mn^{3+}, Fe^{3+}, Co, Ni, Zn, Mn^{2+}, Fe^{2+}, Mg and Li, T = Si, P, Be, Al^{IV}, Ti^{4+} and Fe^{3+} and W = OH, F, Cl and O^{-2}, Hawthorne et al., 2012). Amphiboles from the Sps-Cum zone form hypidiomorphic crystals showing intensive pleochroism in shades of green.

[D]For the estimation of pressure of the Grt-Ep zone in Panorama and Grt-Cum zone in Thapsana, we have employed on the Al-in-hornblende geobarometer of Hammarstrom and Zen (1986). In the magmatic hornblende the Al^{tot} content correlates linearly with crystallization pressure. The Al-in-hornblende geobarometer was re-evaluated by Johnson and Rutherford (1989) and Schmidt, (1992). The calibration studies have emphasized that the Al-in-hornblende geobarometer should be applied for the assemblage hornblende + biotite + plagioclase + K-feldspar + quartz + titanite + Fe-Ti oxides. The analyzed hornblendes from Panorama and Thapsana have Al^{total} values that range from 0.90 to 1.14 and 0.77 to 1.44, respectively. We have used the equation of Anderson and Smith (1995) as it suits better for skarns. For our calculations we have used the excel sheet Pmeter-Al-in-HbBt). The estimated pressure during the emplacement of Panorama granite was ~300 MPa, while for the formation of the Grt-Px zone at Panorama ranged from ~120 to ~160 MPa (cores to rims, average of ~150 MPa, st.d. = 20). Likewise, for the Sps-Cum zone at Paros pressure ranged from ~100 to ~190 MPa (cores to rims, average of ~140 MPa, st.d. = 40 MPa).

[E]For the estimation of pressure of the Grt-Cum zone in Thapsana, we have also employed on the ^{T}Al biotite geothermometer of Uchida et al. (2007). The analyzed biotites from Panorama Thapsana have Al^{total} values that range from 1.60 to 1.71. For our calculations we have used the excel sheet Pmeter-Al-in-HbBt. The estimated pressure during the formation of the Grt-Cum zone at Thapsana ranged from~120 to ~140 MPa (cores to rims, average of ~120 Mpa, st.d. = 10).

Electronic Supplementary Material, Table 6. Representative electron microprobe analyses of epidote from the skarn of Panorama, Drama and Thapsana, Paros (all results in wt. %).

Mineral: Epidote[1]						
Locality and exo-skarn type	Panorama calcic				Thapsana mangan	
Mineralogical Zone	Grt - Ep				Sps - Cum	
Analyzed Spots	Core	Rim	Core	Rim	Core	Rim
SiO_2	37.24	37.28	33.79	36.04	38.88	38.28
TiO_2	0.00	0.00	0.29	0.00	0.00	0.00
Al_2O_3	32.58	32.27	19.98	21.78	17.99	17.77
Fe_2O_3	0.61	1.26	13.11	12.54	3.2	3.22
MnO	2.37	2.41	0.67	0.05	33.61	34.36
MgO	0.25	0.00	0.00	0.38	1.59	1.42
CaO	24.52	24.28	16.62	18.76	4.73	4.96
Na_2O	0.00	0.07	0.17	0.52	0.00	0.00
K_2O	0.00	0.04	0.00	0.25	0.00	0.00
H_2O	0.00	0.00	0.00	0.00	0.00	0.00
La_2O_3	0.00	0.00	6.26	1.82	0.00	0.00
Ce_2O_3	0.00	0.00	5.51	4.64	0.00	0.00
Nd_2O_3	0.00	0.00	0.98	1.42	0.00	0.00
HfO_2	0.00	0.00	1.11	0.00	0.00	0.00
Total	97.57	97.61	98.49	98.2	100	100.01
			Nº of atoms based on			
Si	3.12	3.13	2.83	3.02	3.26	3.21
Ti	0.00	0.00	0.02	0.00	0.00	0.00
Al	3.22	3.19	1.97	2.15	1.78	1.76
Fe^{3+}	0.04	0.09	0.92	0.88	0.22	0.23
$Mn^{3+(calculated)}$	0.17	0.17	0.05	0.00	2.39	2.44
Mg	0.03	0.00	0.00	0.05	0.19	0.18
Ca	2.20	2.18	1.49	1.69	0.43	0.45
Na	0.00	0.01	0.03	0.09	0.00	0.00
K	0.00	0.00	0.00	0.03	0.00	0.00
H_2O	1.00	1.00	1.00	1.00	1.00	1.00
La	0.00	0.00	0.19	0.06	0.00	0.00
Ce	0.00	0.00	0.17	0.14	0.00	0.00
Nd	0.00	0.00	0.03	0.04	0.00	0.00
Hf	0.00	0.00	0.03	0.00	0.00	0.00
Total	9.79	9.77	8.74	9.14	9.27	9.25
O	12.5	12.5	12.5	12.5	12.5	12.5
Ps	1.31	2.69	31.77	29.00	8.67	11.39
$Ca/Al+Fe^{3+}$	67.52	66.55	55.59	51.59	21.22	22.48
ΣREE	0.00	0.00	0.24	0.42	0.00	0.00
$\Sigma REE/Ca^{2+}+Al+Fe^{3+}$	0.00	0.00	9.64	5.11	0.00	0.00
Ce/ΣREE	0.00	0.00	39.98	59.08	0.00	0.00
La/ΣREE	0.00	0.00	45.76	23.35	0.00	0.00
Nd/ΣREE	0.00	0.00	6.94	17.64	0.00	0.00
Hf/ΣREE	0.00	0.00	6.94	0.00	0.00	0.00

[1]Epidote formulae were calculated normalized on 12.5 oxygens, based on the generalized formula $A_2M_3[T_2O_7][TO_4](O.F)(OH.O)$ (A = Ca, Mn^{2+}, Sr, Pb, REE, Th and U, M = Al, Fe^{3+}, Fe^{+2}, Mn^{3+}, Cr and V, and T = Si, Armbruster et al., 2006). The epidote-group minerals are divided into three subgroups: The clinozoisite subgroup where A = Ca, M = Al and T = Si, the allanite and the dollaseite subgroups. In these subgroups which are considered as clinozoisite derivatives there is one or two heterovalent substitutions of the higher charge REE^{3+} replacing Ca^{2+} in the M_3 and M_3 and M_1 site and O_4 by O^{2-} and F^- site, respectively. To assign minerals either to the REE-rich clinozoisite (with a simplified formula of $(Ca, REE)_2Al_2Fe^{3+}[Si_2O_7][SiO_4]O(OH)$), or the allanite $[(Ca, REE)Al_2Fe^{2+}[Si_2O_7][SiO_4]O(OH)]$ subgroup the recommended chemical criterion is that REE + ACT (actinides) ≥ 0.5 apfu. The FeO, MnO and K_2O contents are ≤ 0.01.

Electronic Supplementary Material, Table 7. Representative electron microprobe analyses of stage I Mn-ores from Thapsana, Paros (all results in wt. %).

Stage I	Br[1]	Br[1]	Hsm[1]	Jac[1]	Jac[1]	Mag[1]	Mn-Mag[1]	Ilm[1]
Locality and exo-skarn type				Thapsana mangan				
Mineralogical Zone				Jhn - Sps				
Analyzed Spots	Core	Rim		Core	Rim	Core	Rim	
SiO_2	10.41	15.50	0.00	0.19	0.00	0.00	0.00	0.02
TiO_2	0.16	0.50	0.00	0.01	0.82	2.39	6.82	55.86
Fe_2O_3	4.23	0.00	0.43	67.84	54.83	0.00	0.00	0.00
FeO	0.00	0.00	0.00	0.00	0.00	95.02	86.92	42.07
Al_2O_3	0.63	1.57	0.00	6.72	0.00	0.00	0.00	1.17
CaO	1.02	4.51	0.00	0.00	0.00	0.00	0.00	0.00
MgO	0.00	4.29	0.21	0.44	3.42	0.00	0.00	0.00
Mn_2O_3	79.16	65.25	62.7	1.06	3.81	0.00	0.00	0.00
MnO	5.16	6.11	32.7	30.07	37.09	2.61	6.26	1.40
Na_2O	0.00	0.08	0.00	0.00	0.00	0.00	0.00	0.00
Total	100.87	100.01	99.91	99.89	99.97	100.02	100.33	100.52
			Nº of atoms based on					
Si	0.84	1.15	0.00	0.00	0.00	0.00	0.00	0.00
Ti	0.01	0.04	0.00	0.00	0.16	0.07	0.19	0.92
Fe^{3+}	0.38	0.00	0.01	1.76	1.38	1.87	1.63	0.12
$Fe^{+2(calculated)}$	0.00	0.00	0.00	0.00	0.00	0.96	0.99	0.90
Al^{IV}	0.09	0.21	0.00	0.07	0.00	0.00	0.00	0.03
Mg	0.00	0.31	0.02	0.10	0.26	0.00	0.00	0.00
$Mn^{3+(calculated)}$	6.11	6.07	1.98	0.05	0.08	0.00	0.00	0.00
$Mn^{2+(calculated)}$	0.61	0.67	0.91	1.02	1.07	0.08	0.19	0.03
Ca	0.10	0.24	0.00	0.00	0.00	0.00	0.00	0.00
Na	0.00	0.02	0.00	0.00	0.00	0.00	0.00	0.00
Total	8.15	8.71	3.00	3.00	2.95	3.00	3.00	2.00
O	12.00	12.00	4.00	4.00	4.00	4.00	4.00	4.00

[1]Braunite (Br) formula has been calculated normalized on 9 cations and 12 oxygens, whereas hausmanite (Hsm), jacobsite (Jac) magnetite (Mag) and ilmenite (Ilm) formulae have been calculated normalized on 3 cations and 4 oxygens based on the formula XY_2O_4 (X = Mg, Mn^{2+} and Fe^{+2} and Y = Cr, Al, Mn^{3+} and Fe^{3+}). The ulvospinel (Usp) mol % range from 9.9 to 18.5%. The ilmenite (Ilm) mol % is 93.5%. Based on the magnetite-ilmenite geothermo-oxygen-barometer (Spencer and Lindsley, 1981) using ILMAT the estimated temperature for the Mag-Ilm pair is T = 555ºC and logfO2 = -17.9.

Electronic Supplementary Material, Table 8. Whole-rock geochemistry of the granitoids and skarns and representative major (wt. %), trace and REE (ppm; Au in ppb) analyses from Panorama, Drama and Thapsana, Paros.

	Panorama granite					Panorama mangan skarns				
						Grt-Wo zone	Grt-Px zone	Grt-Px zone	Grt-Ep zone	Grt-Ep zone
Sample	PAG_1	PAG_2	PAG_3	PAG_4	PAG_5	PAS_1	PAS_2	PAS_3	PAS_4	PAS_5
SiO_2	67.37	68.36	72.92	73.47	75.40	37.15	37.21	40.83	41.06	39.50
TiO_2	0.17	0.39	0.20	0.18	0.15	0.20	0.20	0.28	0.28	0.24
Al_2O_3	14.44	15.37	14.56	14.83	13.20	28.93	28.95	29.56	29.56	27.40
Fe_2O_3	1.37	3.07	1.64	0.51	1.13	0.79	0.81	1.46	1.51	3.18
MnO	0.10	0.12	0.07	0.08	0.03	2.04	2.02	1.75	1.69	1.36
MgO	1.21	0.93	0.46	0.11	0.10	0.23	0.21	0.34	0.35	0.65
CaO	5.10	3.63	2.28	1.53	1.10	23.45	23.51	18.83	18.77	20.44
Na_2O	2.51	3.51	2.87	3.49	3.80	0.08	0.07	0.55	0.56	0.47
K_2O	4.37	3.93	4.49	5.41	4.60	0.04	0.04	0.75	0.81	0.56
P_2O_5	0.06	0.13	0.08	0.04	0.04	0.06	0.06	0.10	0.12	0.09
LOI	3.30	0.54	0.42	0.33	0.41	6.93	6.59	5.55	5.26	6.00
Total	100.00	99.98	99.99	99.98	99.96	99.9	99.96	100.00	99.97	99.89
Cu	10	16	21	12	17	11	15	21	45	37
Pb	29	32	25	30	31	12	19	25	38	42
Au	2	2	2	2	2	3	2	2	2	2
Ag	0.5	0.5	0.5	0.6	0.5	0.6	0.5	0.6	0.9	0.9
Zn	11	7	10	12	15	24	35	42	17	26
As	10	9	12	11	8	17	19	21	47	48
Sb	13	8	9	14	12	27	16	24	33	42
Be	1	2	2	2	1	3	3	4	3	4
V	34	23	29	21	17	12	10	9	9	11
Co	6	4	3	4	2	14	12	9	7	10
Ni	25	23	29	32	27	31	26	26	23	29
Cr	20	20	20	20	21	25	28	20	21	20
Mo	3	5	6	4	11	14	12	13	10	9
W	3	6	12	7	9	17	12	16	8	11
Nb	14.2	18.7	15.3	16.6	20.2	1.3	1.5	2.2	3.1	3.3
Th	17.9	18.3	13.9	15.1	22.0	7.8	3.4	2.7	6.3	5.6
U	2.8	2.7	2.2	3.1	3.3	0.5	0.7	1.1	2.1	0.7
Bi	3.2	2.5	2.2	2.9	3.1	0.5	0.3	0.8	1.1	1.4
Ga	14	15	18	11	14	2	4	2	3	11
Ta	1.4	1.3	1.2	1.5	1.1	1.9	2.0	2.2	2.7	1.8
Zr	154	167	136	221	196	54	45	38	21	34
Cs	2.2	2.7	1.9	1.6	2.3	0.5	0.4	0.9	1.1	1.3
Rb	129	140	178	205	136	17	12	21	19	8
Sr	299	413	335	312	399	217	302	287	243	226
Ba	361	445	299	307	348	145	189	95	112	167

Sc	3.1	6.2	4.3	5.8	5.2	6.7	5.8	4.9	7.5	6.1
Tl	0.24	0.43	0.37	0.33	0.28	0.36	0.20	0.39	0.41	0.50
Hf	1.02	0.95	0.77	0.82	0.90	0.23	0.27	0.45	0.46	0.87
La	8.9	7.8	11.3	10.4	9.3	2.9	2.5	3.2	4.1	3.8
Ce	10.6	12.5	10.7	11.5	12.1	4.7	3.8	5.2	4.9	7.2
Pr	1.3	1.4	2.2	0.7	0.9	0.8	0.9	1.2	1.1	1.8
Nd	15.6	17.8	16.1	12.5	19.2	1.93	1.74	2.37	2.81	3.16
Sm	2.42	2.18	3.03	1.89	2.24	0.86	0.75	0.56	0.89	0.94
Eu	0.64	0.73	0.82	0.79	0.65	0.24	0.19	0.29	0.33	0.30
Gd	1.03	0.96	0.88	1.12	1.19	0.67	0.72	0.97	1.04	1.19
Tb	0.17	0.14	0.24	0.31	0.22	0.18	0.19	0.24	0.28	0.31
Dy	1.15	1.45	1.36	1.52	1.69	0.75	0.69	0.97	1.05	1.16
Ho	0.18	0.22	0.24	0.33	0.29	0.19	0.24	0.29	0.35	0.39
Er	0.36	0.48	0.42	0.39	0.51	0.24	0.21	0.46	0.55	0.89
Tm	0.19	0.17	0.25	0.33	0.29	0.09	0.16	0.15	0.17	0.21
Yb	0.9	1.7	2.1	1.6	1.8	1.5	1.4	1.8	2.1	2.6
Lu	0.13	0.22	0.18	0.21	0.14	0.33	0.26	0.29	0.32	0.44
Y	19	25	18	28	31	15	17	22	29	25
ASI	0.80	0.93	1.07	1.05	1.00	-	-	-	-	-
Mn/Fe	0.07	0.04	0.03	0.16	0.03	2.58	2.49	1.20	1.12	0.43
CaO/Na_2O	2.03	1.03	0.79	0.44	0.29	-	-	-	-	-
ΣREE	43.57	47.75	49.82	43.59	50.52	15.38	13.75	17.99	19.99	24.39
LREE/HREE	9.60	7.94	7.79	6.50	7.24	2.89	2.55	2.48	2.41	2.39
Nb/Ta	10.14	14.38	12.75	11.07	18.36	0.68	0.75	1.01	1.15	1.83
Zr/Hf	150.98	175.79	176.62	269.51	217.78	234.78	166.67	84.44	45.65	39.08
Th/U	6.39	6.78	6.32	4.87	6.67	15.60	4.86	2.45	3.02	8.01
K/Rb	339	281	252	264	338	24	33	357	426	699
Rb/Sr	0.43	0.34	0.53	0.66	0.34	0.08	0.04	0.07	0.08	0.04
Rb/Ba	0.36	0.31	0.60	0.67	0.39	0.12	0.06	0.22	0.17	0.05
Rb/Zr	0.84	0.84	1.31	0.93	0.69	0.31	0.27	0.55	0.9	0.24
$(La/Yb)_N$	6.72	3.12	3.66	4.42	3.51	1.31	1.21	1.21	1.33	0.99
$(Gd/Yb)_N$	1.55	0.76	0.57	0.95	0.89	0.61	0.69	0.73	0.67	0.62
$(La/Sm)_N$	2.93	1.39	1.57	1.29	1.35	0.62	0.58	0.34	0.46	0.39
Ce/Ce*	0.67	0.85	0.49	0.73	0.81	0.74	0.61	0.64	0.55	0.66
Eu/Eu*	0.25	0.32	0.28	0.36	0.26	0.22	0.18	0.28	0.25	0.21
Y/Ho	105.56	113.64	75.01	84.85	106.92	78.95	70.83	75.86	82.86	64.11

Electronic Supplementary Material, Table 8 (continued)

	Thapsana leucogranite					Thapsana mangan skarns		
						Rhn zone	Jhn-Sps zone	Sps-Cum zone
Sample	PTG_1	PTG_2	PTG_3	PTG_4	PTG_5	PTS_1	PTS_2	PTS_3
SiO_2	75.21	73.99	72.56	70.85	71.35	64.30	9.63	12.79
TiO_2	0.02	0.03	0.03	0.05	0.03	0.00	0.13	0.05
Al_2O_3	14.83	14.57	14.99	15.05	15.33	0.32	1.63	6.75
Fe_2O_3	0.56	0.59	1.69	2.07	2.19	1.43	2.74	1.53
MnO	0.08	0.03	0.05	0.07	0.10	17.01	9.78	28.37
MgO	0.07	0.09	0.19	0.69	0.65	0.13	4.55	1.18
CaO	1.19	1.06	1.86	2.34	1.99	4.88	39.44	26.46
Na_2O	4.06	3.58	3.45	2.99	4.12	0.05	0.55	0.17
K_2O	3.92	5.04	4.04	4.13	2.47	0.11	0.17	0.12
P_2O_5	0.02	0.06	0.04	0.08	0.07	0.01	0.07	0.01
LOI	0.04	0.96	1.11	1.68	1.69	8.94	29.86	20.64
Total	99.96	99.04	98.89	98.32	98.31	97.18	98.55	98.07
Cu	15	13	15	16	12	130	80	30
Pb	13	6	8	12	7	134	6	12
Au	2	2	3	2	2	2	2	2
Ag	0.5	0.7	0.7	1.8	0.9	20	5.6	4.6
Zn	40	30	55	110	67	1970	80	40
As	12	14	13	25	41	189	752	396
Sb	7	12	6	4	6	69	24	43
Be	1	2	1	1	3	3	3	1
V	9	12	15	13	17	15	5	17
Co	1	1	2	2	4	174	242	224
Ni	20	21	22	20	20	20	21	24
Cr	20	20	20	20	20	20	20	60
Mo	7	4	12	6	11	43	2	4
W	234	167	196	265	289	1710	189	390
Nb	22.4	19.6	14.9	17.3	20.6	1.5	1.2	1.9
Th	12.1	15.2	15.9	16.8	19.3	0.4	0.2	0.1
U	2.5	2.7	1.4	1.3	0.9	2.2	0.7	1.1
Bi	2.1	2.2	2.6	1.9	1.7	1.5	1.6	1.4
Ga	17	18	21	16	20	6	5	10
Ta	2.5	3.4	1.8	1.9	2.3	1.4	0.3	0.3
Zr	113	146	299	175	178	43	35	18
Cs	1.2	1.7	0.5	1.1	0.9	0.5	0.5	1.8
Rb	199	187	203	169	133	15	22	21
Sr	59	145	189	289	222	346	382	466
Ba	440	512	894	367	399	22810	393	158
Sc	3.1	6.2	7.3	4.5	3.2	3.4	9.1	6.3
Tl	0.39	0.65	0.54	0.33	0.28	0.41	0.78	0.24
Hf	0.35	0.47	0.87	0.77	0.95	0.21	0.99	0.61
La	12.1	9.2	15.3	22.2	18.7	3.1	1.7	7.3

Ce	20.3	22.7	27.2	33.4	26.5	5.3	2.9	5.7
Pr	1.1	1.7	0.6	0.7	0.9	0.6	0.5	1.5
Nd	11.1	12.4	19.3	20.2	17.6	2.3	2.5	5.9
Sm	3.15	3.32	2.79	1.88	1.94	0.61	2.53	1.64
Eu	0.91	0.78	0.65	0.57	0.34	0.14	0.18	0.45
Gd	0.79	1.36	1.68	1.99	0.88	0.81	0.78	2.14
Tb	0.19	0.17	0.33	0.29	0.24	0.21	0.18	0.40
Dy	1.02	0.89	1.75	1.68	2.17	1.11	0.93	2.36
Ho	0.27	0.28	0.26	0.38	0.46	0.31	0.22	0.49
Er	1.43	1.58	0.94	0.85	1.25	0.41	0.88	1.52
Tm	0.11	0.17	0.25	0.13	0.26	0.21	0.14	0.24
Yb	1.2	2.3	1.5	1.4	0.9	1.6	1.2	1.8
Lu	0.25	0.32	0.27	0.24	0.19	0.27	0.24	0.31
Y	26	29	21	19	23	47	29	18
ASI	1.12	1.15	1.11	1.14	1.09	-	-	-
Mn/Fe	0.14	0.05	0.03	0.02	0.05	11.90	3.57	18.54
CaO/Na_2O	0.29	0.31	0.54	0.78	0.48	-	-	-
ΣREE	53.92	57.17	72.82	85.91	72.33	16.98	14.88	31.75
LREE/HREE	9.25	7.09	9.43	11.34	10.39	2.44	2.26	2.43
Nb/Ta	8.96	5.76	8.28	9.11	8.96	1.07	4.03	6.33
Zr/Hf	322.86	310.64	343.68	227.27	187.37	204.76	35.35	29.51
Th/U	4.84	5.63	11.36	12.92	21.44	0.18	0.29	0.09
K/Rb	197	270	199	244	186	73	77	57
Rb/Sr	0.43	0.34	0.53	0.66	0.34	0.08	0.04	0.07
Rb/Ba	0.45	0.37	0.23	0.46	0.33	0.01	0.06	0.13
Rb/Zr	1.76	1.28	0.68	0.97	0.75	0.35	0.63	1.17
$(La/Yb)_N$	6.85	2.72	6.93	10.77	7.11	1.32	0.96	2.76
$(Gd/Yb)_N$	0.89	0.81	1.52	1.92	1.32	0.68	0.88	1.61
$(La/Sm)_N$	2.86	1.57	2.02	1.46	2.34	0.41	2.29	0.99
Ce/Ce*	1.05	1.32	1.25	1.08	0.98	0.88	0.75	0.41
Eu/Eu*	0.30	0.22	0.20	0.21	0.16	0.14	0.07	0.17
Y/Ho	96.3	103.57	80.77	50.04	49.99	151.61	131.82	36.73

Electronic Supplementary Material, Table 9. Zircon U-Pb data of the Panorama granite and Panorama, Drama (Grt-Ep zone) and Thapsana, Paros (Sps-Cum zone) mangan skarns.

Sample	Isotopic compositions											
	U (ppm)	Th (ppm)	Th/U	f^*_{206} (%)	$^{207}Pb/^{206}Pb$	1σ (%)	$^{207}Pb/^{235}U$	1σ (%)	$^{206}Pb/^{238}U$	1σ (%)	$^{208}Pb/^{232}Th$	1σ (%)
Panorama granite												
PPG_1_1	55	28	0.51	0.11	0.032	0.007	0.093	0.003	0.014	0.001	0.005	0.003
PPG_1_2	42	37	0.88	0.18	0.035	0.006	0.095	0.004	0.013	0.005	0.004	0.004
PPG_1_3	38	29	0.76	0.06	0.036	0.005	0.105	0.001	0.015	0.002	0.005	0.005
PPG_1_4	49	27	0.55	0.12	0.035	0.001	0.100	0.008	0.014	0.004	0.005	0.003
Panorama mangan skarn (Grt-Ep zone)												
PPSK_17_1	34	14	0.41	0.21	0.035	0.003	0.104	0.001	0.013	0.002	0.005	0.002
PPSK_17_2	47	19	0.40	0.18	0.034	0.008	0.098	0.009	0.012	0.003	0.004	0.003
PPSK_17_3	50	22	0.44	0.26	0.045	0.005	0.107	0.007	0.012	0.002	0.007	0.004
PPSK_17_4	39	28	0.72	0.33	0.041	0.008	0.108	0.006	0.013	0.002	0.008	0.003
PPSK_17_5	43	32	0.74	0.16	0.036	0.002	0.106	0.008	0.014	0.004	0.005	0.001
Paros mangan skarn (Sps-Cum zone)												
PTS_1_1	11	6	0.55	0.24	0.009	0.003	0.028	0.007	0.004	0.007	0.001	0.004
PTS_1_1	17	11	0.65	0.35	0.008	0.002	0.024	0.005	0.004	0.003	0.001	0.005
PTS_1_1	20	7	0.35	0.19	0.008	0.004	0.025	0.005	0.004	0.005	0.001	0.006
PTS_1_1	9	3	0.33	0.31	0.009	0.007	0.026	0.006	0.004	0.002	0.001	0.004
PTS_1_1	15	12	0.80	0.27	0.010	0.002	0.027	0.003	0.004	0.006	0.001	0.002

Electronic Supplementary Material, Table 9 (continued).

Sample	Ages (Ma)							
	$t_{207/206}$	1σ (%)	$t_{207/235}$	1σ (%)	$t_{206/238}$	1σ (%)	$t_{208/232}$	1σ (%)
Panorama granite								

PPG_1_1	25.97	0.023	25.18	0.025	26.05	0.027	25.64	0.014
PPG_1_2	25.52	0.029	25.84	0.028	25.59	0.017	25.89	0.024
PPG_1_3	25.82	0.024	26.66	0.013	26.17	0.024	27.01	0.017
PPG_1_4	25.57	0.046	25.63	0.026	26.30	0.028	26.56	0.024
Panorama mangan skarn (Grt-Ep zone)								
PPSK_17_1	24.72	0.023	24.94	0.019	24.74	0.029	25.87	0.033
PPSK_17_2	24.28	0.032	23.45	0.029	24.89	0.019	25.13	0.023
PPSK_17_3	25.20	0.026	24.49	0.022	24.68	0.022	24.91	0.019
PPSK_17_4	23.31	0.040	23.42	0.031	24.75	0.026	23.31	0.014
PPSK_17_5	24.83	0.018	25.23	0.012	24.73	0.028	24.52	0.012
Paros mangan skarn (Sps-Cum zone)								
PTS_1_1	6.28	0.008	6.10	0.002	6.17	0.004	6.11	0.001
PTS_1_1	6.19	0.005	6.25	0.006	6.16	0.003	5.88	0.006
PTS_1_1	6.01	0.003	5.64	0.001	5.77	0.004	6.66	0.005
PTS_1_1	6.13	0.009	6.03	0.008	5.91	0.006	6.20	0.004
PTS_1_1	5.92	0.005	6.39	0.005	5.88	0.009	5.90	0.007

Note: The uncertainty correlation factor (rho) is applied to assess the degree of correlation between $^{207}Pb/^{235}U$ and $^{206}Pb/^{238}U$ ratios.

Electronic Supplementary Material, Table 10a Calculated physicochemical parameters of the metasomatic fluids* from Panorama, Drama and Thapsana, Paros mangan skarns and thermodynamic data used in simulation modeling.

	Reaction	Zone	Calculated activity-fugacity
	Mangan skarn		
1	$SiO_{2(s)} + 2H_2O_{(l)} = 2H_2O_{(l)} + SiO_{2(aq)} = H_4SiO_{4(aq)}$	Tep-Rhn[1], Sps-Di-Cum[2], Pmt-Phl[3]	$\log\alpha_{SiO2(aq)}$ = -2.9, -2.6, -2.3
2	$Mn_2SiO_{4(s)} + CO_{2(g)} = 2MnSiO_{3(s)} + MnCO_{3(s)}$ (Tep = Rhn/Pxm+Rds)	Tep-Rhn	$\log X_{CO2(g)}$ = -0.69
3	$6Mn_2SiO_{4(s)} + 4O_{2(g)} = 2Mn^{2+}Mn^{3+}{}_6SiO_{12(s)} + 4SiO_{2(aq)}$ (Tep-Br)	Tep-Rhn	$\log fO_2$ = -10.9 = HM+5.7
4	$12MnSiO_{3(s)} + 4O_{2(g)} = 2Mn^{2+}Mn^{3+}{}_6SiO_{12(s)} + 10SiO_{2(aq)}$ (Rhn-Br)	Tep-Rhn	$\log fO_2$ = -11.0 = HM+5.6
5	$Mn^{2+}{}_2SiO_{4(s)} + 7[(Mn^{2+},Fe,Mg)]CO_{3(s)} + 4H^+ + 10.5O_{2(g)} = (Mg,Fe,Mn^{2+})_7Si_8O_{22}(OH)_{2(s)} + 7CO_{2(g)} + 2Mn^{2+}{}_{(aq)}$ (Tep + Cal = Cum)	Sps-Di-Cum	$\log X_{CO2(g)}$ = -0.86
6	$14Mn^{2+}Mn^{3+}{}_2O_{4(s)} + 32SiO_{2(aq)} + 4H_2O_{(l)} = 4Mn_7Si_8O_{22}(OH)_{2(s)} + 14O_{2(g)}$ (Hsm-Cum)	Sps-Di-Cum	$\log fO_2$ = -13.2 = HM+6.2
7	$MnCO_{3(s)} + 2H^+{}_{(aq)} = Mn^{2+}{}_{(aq)} + CO_{2(g)} + H_2O_{(l)}$ (Rhd)	Sps-Di-Cum, Pmt-Phl	$\log X_{CO2(g)}$ = -1.12
8	$Mn^{2+}Mn^{3+}{}_6SiO_{12(s)} + 18H^+{}_{(aq)} = Mn^{2+} + 6Mn^{3+} + SiO_{2(aq)} + 9H_2O_{(l)} + 0.5O_{2(g)}$ (Br)	Pmt-Phl	$\log fO_2$ = -26.8 = HM-3.9
9	$SiO_{2(s)} + 2H_2O_{(l)} = 2H_2O_{(l)} + SiO_{2(aq)} = H_4SiO_{4(aq)}$	Rhn[1], Jhn-Sps[2], Sps-Cum[3]	$\log\alpha_{SiO2(aq)}$ = -1.5, -1.3, -1.1
10	$CaCO_{3(s)} + Mn^{+2}{}_{(aq)} + SiO_{2(s)} = MnSiO_{3(s)} + CO_{2(g)} + Ca^{2+}{}_{(aq)}$ (M-Rhn)	Rhn	$\log X_{CO2(g)}$ = -0.77, $\log fO_2 \approx$ -10 = HM+5.5
11	$2MnSiO_{3(s)} + SiO_{2(aq)} + CaCO_{3(s)} = CaMnSi_2O_{6(s)} + CO_{2(g)}$ (Rhn-Jhn)	Jhn-Sps	$\log X_{CO2(g)}$ = -2.1
12	$12MnSiO_{3(s)} + 4O_{2(g)} = 2Mn^{2+}Mn^{3+}{}_6SiO_{12(s)} + 10SiO_{2(aq)}$ (Rhn-Br)	Jhn-Sps	$\log fO_2$ = -17.9 = HM-0.4
13	$13MnSiO_{3(s)} + 6CaCO_{3(s)} + 1.5O_{2(g)} = Mn^{2+}Mn^{3+}SiO_{12} + 6CaMnSi_2O_{6(s)} + 6CO_{2(g)}$ (Rhd + Cal = Br + Jhn)	Jhn-Sps	$\log fO_2$ = -20.3 = HM-2.3
14	$7MnCO_{3(s)} + 8SiO_{2(aq)} + H_2O_{(l)} = Mn_7Si_8O_{22}(OH)_{2(s)} + 7CO_{2(g)}$ (Rds-Cum)	Sps-Cum	$\log X_{CO2(g)}$ = -3.5
15	$14Mn^{2+}Mn^{3+}{}_2O_{4(s)} + 32SiO_{2(aq)} + 4H_2O_{(l)} = 4Mn_7Si_8O_{22}(OH)_{2(s)} + 14O_{2(g)}$ (Hsm-Cum)	Sps-Cum	$\log fO_2$ = -24.6 = HM+0.8
	Calcic and mangan skarn		
16	$SiO_{2(s)} + 2H_2O_{(l)} = 2H_2O_{(l)} + SiO_{2(aq)} = H_4SiO_{4(aq)}$	Grt-Wo[1], Grt-Px[2], Grt-Ep[3]	$\log\alpha_{SiO2(aq)}$ = -3.5, -2.8, -1.8
17	$SiO_{2(aq)} + CaCO_{3(s)} = CaSiO_{3(s)} + CO_{2(g)}$ (Qz + Cal = Wo)	Grt-Wo	$\log X_{CO2(g)}$ = -1.00
18	$3CaSiO_{3(s)} + Fe_3O_{4(s)} + 3SiO_{2(aq)} = 3CaFeSi_2O_{6(s)} + 0.5O_{2(g)}$ (Wo + Mag = Hd)	Grt-Wo	$\log fO_2$ = -17 = HM-1.8
19	$Ca_3Al_2Si_3O_{12(s)} + CO_{2(g)} = CaAl_2Si_2O_{8(s)} + CaCO_{3(s)} + SiO_{2(aq)}$ (Grs = An + Cal)	Grt-Px	$\log X_{CO2(g)}$ = -1.46
20	$CaCO_{3(s)} + 2CaFeSi_2O_6(s) + 0.5O_{2(g)} = Ca_3Fe_2Si_3O_{12(s)} + SiO_{2(aq)} + CO_{2(g)}$ (Cal + Hd = And)	Grt-Px	$\log fO_2$ = -21.2 = HM-3.2
21	$Mn^{2+}{}_3Al_2Si_3O_{12(s)} + 2CaCO_{3(s)} + 3SiO_{2(aq)} + 19Mn^{3+}{}_{(aq)} + 87H_2O_{(l)} = Ca_2Al_2Mn^{3+}Si_3O_{12}(OH)_{(s)} + 3Mn^{2+}Mn^{3+}{}_6SiO_{2(s)} + 2CO_{2(g)} + 57H^+{}_{(aq)} + 15O_{2(g)}$ (Sps-Pmt)	Grt-Ep	$\log X_{CO2(g)}$ = -1.61
22	$3CaAl_2Si_2O_{8(s)} + CaCO_{3(s)} + H_2O_{(l)} + 8O_{2(g)} = 2Ca_2Al_3Si_3O_{12}(OH)_{(s)} + CO_2$ (Grs-Ep)	Grt-Ep	$\log fO_2$ = -32.8= HM-7.8

[1]Assuming for mangan skarn formation average temperatures of [1]550°, [2]500°and [3]380°C, pressure of ~120 and ~150 MPa, and ionic strength of 0.31. Thermodynamic properties of manganese ligands (c.f., Table 1) and data were compiled from Tian et al. (2014) for the hypothetical zones (e.g., Tep-Rhn, Sps-Di-Cum, Pmt-Phl zones produced during our modeling), or exposed in the field (e.g., Rhn, Jhn-Sps and Sps-Cum zones for Thapsana, and Grt-Wo, Grt-Rx and Grt-Ep zones for Panorama).

The temperature versus X_{CO2} plot was constructed for T = 500º and 380ºC and pressure of 1500 bars, with the following assumptions: (i). Fluid pressure is equal to total pressure, (ii). Constant volume change of each reaction for the minerals, and (iii). Ideal mixing of $H_2O_{(l)}$ and $CO_{2(g)}$.

We have also calculated the $logfO_2$ values of the residual melts of Panorama, Paros, Ikaria, Naxos and Tinos peraluminous granitoids, b**ased on the equation of** Zen (1985) for the assemblage Bt-Sps-Ms-Mag-Qz. The calculated $logfO_2$ values of these residual peraluminous melts of these granitoids are HM-4.9 for Tinos, HM-4.5 for Naxos, HM-3.9 for Panorama, HM-3.3 for Paros and HM-2.0 for Ikaria (where HM is the Hematite-Magnetite buffer).

* The initial composition of the skarn-forming fluid used in the simulation was $loga_{\Sigma Cl^-(aq)} = -0.6$, $loga_{HCl(aq)} = -1.6$, $m_{Si(aq)} = m_{\Sigma Al(aq)} = m_{\Sigma Mn(aq)} = 100$ ppm, $m_{Ca^{2+}(aq)} = m_{Mg^{2+}(aq)} = m_{\Sigma Fe(aq)} = m_{K^+(aq)} = 10$ ppm, $loga_{Mn^{2+}(aq)} = -0.3$ and $loga_{Mn^{3+}(aq)} = -1.2$ (at T = 565ºC, pH = 3.5, Eh = 0.5 V, I = 0.35, $a_{H2O} = 0.995$, solvent mass = 1000 g, solution mass = 1056.33 g, $logf_{CO2(g)} = -2$, chlorinity of 4390 ppm and d = 0.53 g/cm^3 (using our fluid inclusions data, Table 1).

Tombros, S., Kokkalas, S., Triantafyllidis, S., Fitros, M., Tsikos, H., Papadopoulou, L., Voudouris, P., Zhai, D., Skliros, V., Perraki, M., Kappis, K., Spiliopoulou, A., Simos, X., Papavasiliou, J., and Williams-Jones, A. 2023, Genesis of a new type of mangan skarn associated with peraluminous granitoids in Greece: Chemical Geology, v. 623, p. 121369

Electronic Supplementary Material, Table 10b Mineral stabilities and related reactions in the system MnO-CaO-FeO-Fe_2O_3-Al_2O_3-SiO_2-H_2O-CO_2 as function of the $\log[\alpha_{Mn}{}^{2+}/(\alpha_{H}{}^{+})^2]$ and $\log[\alpha_{Mn}{}^{3+}/(\alpha_{H}{}^{+})^3]$ ratios used in thermodynamic modeling of the metasomatic fluids from Panorama, Drama and Thapsana, Paros mangan skarns.

	Reaction	Zone	Calculated activity-fugacity
	Mangan skarn		
23	$MnCO_{3(s)} + 2SiO_{2(aq)} + H_2O_{(l)} + Mn^{+2}{}_{(aq)} = 2MnSiO_{3(s)} + CO_{2(g)} + 2H^{+}{}_{(aq)}$ (Rds-Rhn)	Tep-Rhn[1]	$\log[\alpha_{Mn}{}^{2+}/(\alpha_{H}{}^{+})^2] = 7.2$
24	$MnCO_{3(s)} + 2H^{+}{}_{(aq)} = Mn^{2+}{}_{(aq)} + CO_{2(g)} + H_2O_{(l)}$ (Rhd)	Sps-Di-Cum[2]	$\log[\alpha_{Mn}{}^{2+}/(\alpha_{H}{}^{+})^2] = 5.3$
25	$3Mn^{3+}{}_2O_{3(s)} + Mn^{2+}{}_{(aq)} + SiO_{2(aq)} + H_2O_{(l)} = Mn^{2+}Mn^{3+}{}_6SiO_{12(s)} + 2H^{+}{}_{(aq)}$ (Bxb-Br)	Pmt-Phl[3]	$\log[\alpha_{Mn}{}^{2+}/(\alpha_{H}{}^{+})^2] = 2.9$
26	$Ca_2Al_2Mn^{3+}Si_3O_{12}(OH)_{(s)} + 3Mn^{2+}Mn^{3+}{}_6SiO_{2(s)} + 2CO_{2(g)} + 57H^{+}{}_{(aq)} + 15O_{2(g)} = Mn^{2+}{}_3Al_2Si_3O_{12(s)} + 2CaCO_{3(s)} + 3SiO_{2(aq)} + 19Mn^{3+}{}_{(aq)} + 87H_2O_{(l)}$ (Pmt-Sps)	Pmt-Phl	$\log[\alpha_{Mn}{}^{3+}/(\alpha_{H}{}^{+})^3] = 2.7$
27	$MnSiO_{3(s)} + 2H^{+}{}_{(aq)} = Mn^{+2}{}_{(aq)} + SiO_{2(aq)} + H2O_{2(l)}$ (Rhn)	Rhn	$\log[\alpha_{Mn}{}^{2+}/(\alpha_{H}{}^{+})^2] = 6.2$
28	$CaCO_{3(s)} + Mn^{+2}{}_{(aq)} + H_2O_{(l)} + 2SiO_{2(s)} = CaMnSi_2O_{6(s)} + CO_{2(g)} + 2H^{+}{}_{(aq)}$ (M-Jhn)	Jhn-Sps	$\log[\alpha_{Mn}{}^{2+}/(\alpha_{H}{}^{+})^2] = 4.9$
29	$MnCO_{3(s)} + 2H^{+}{}_{(aq)} = Mn^{2+}{}_{(aq)} + CO_{2(g)} + H_2O_{(l)}$ (Rhd)	Sps-Cum	$\log[\alpha_{Mn}{}^{2+}/(\alpha_{H}{}^{+})^2] = 1.6$
30	$Mn^{3+}O(OH)_{(s)} + 3H^{+}{}_{(aq)} = Mn^{3+}{}_{(aq)} + 2H_2O_{(l)}$ (Mgn)	Sps-Cum	$\log[\alpha_{Mn}{}^{3+}/(\alpha_{H}{}^{+})^3] = 3.4$
	Calcic and mangan skarn		
31	$Mn^{3+}O(OH)_{(s)} + 3H^{+}{}_{(aq)} = Mn^{3+}{}_{(aq)} + 2H_2O_{(l)}$ (Mgn)	Grt-Px	$\log[\alpha_{Mn}{}^{2+}/(\alpha_{H}{}^{+})^2] = 5.1$
32	$MnCO_{3(s)} + 2H^{+}{}_{(aq)} = Mn^{2+}{}_{(aq)} + CO_{2(g)} + H_2O_{(l)}$ (Rhd)	Grt-Ep	$\log[\alpha_{Mn}{}^{3+}/(\alpha_{H}{}^{+})^3] = 4.8$

Abbreviations: Tep = Tephroite, Rhn = Rhodonite, Pmx = Pyroxmangite, Bxb = Bixbyite, Rds = Rhodochrosite, Br = Braunite, Cal = Calcite, Cum = Cummingtonite, Hsm = Hausmanite, Di = Diopside, Hd = Hedenbergite, Adr = Andradite, Grs = Grossular, Ep = Epidote, Pmt = Piemontite, An = Anorthite, Qz = Quartz, Wo = Wollastonite, Mag = Magnetite, Mgn = Manganite, Prs = Pyrolusite, M = Marble.

Tombros, S., Kokkalas, S., Triantafyllidis, S., Fitros, M., Tsikos, H., Papadopoulou, L., Voudouris, P., Zhai, D., Skliros, V., Perraki, M., Kappis, K., Spiliopoulou, A., Simos, X., Papavasiliou, J., and Williams-Jones, A. 2023, Genesis of a new type of mangan skarn associated with peraluminous granitoids in Greece: Chemical Geology, v. 623, p. 121369

ESM Figures

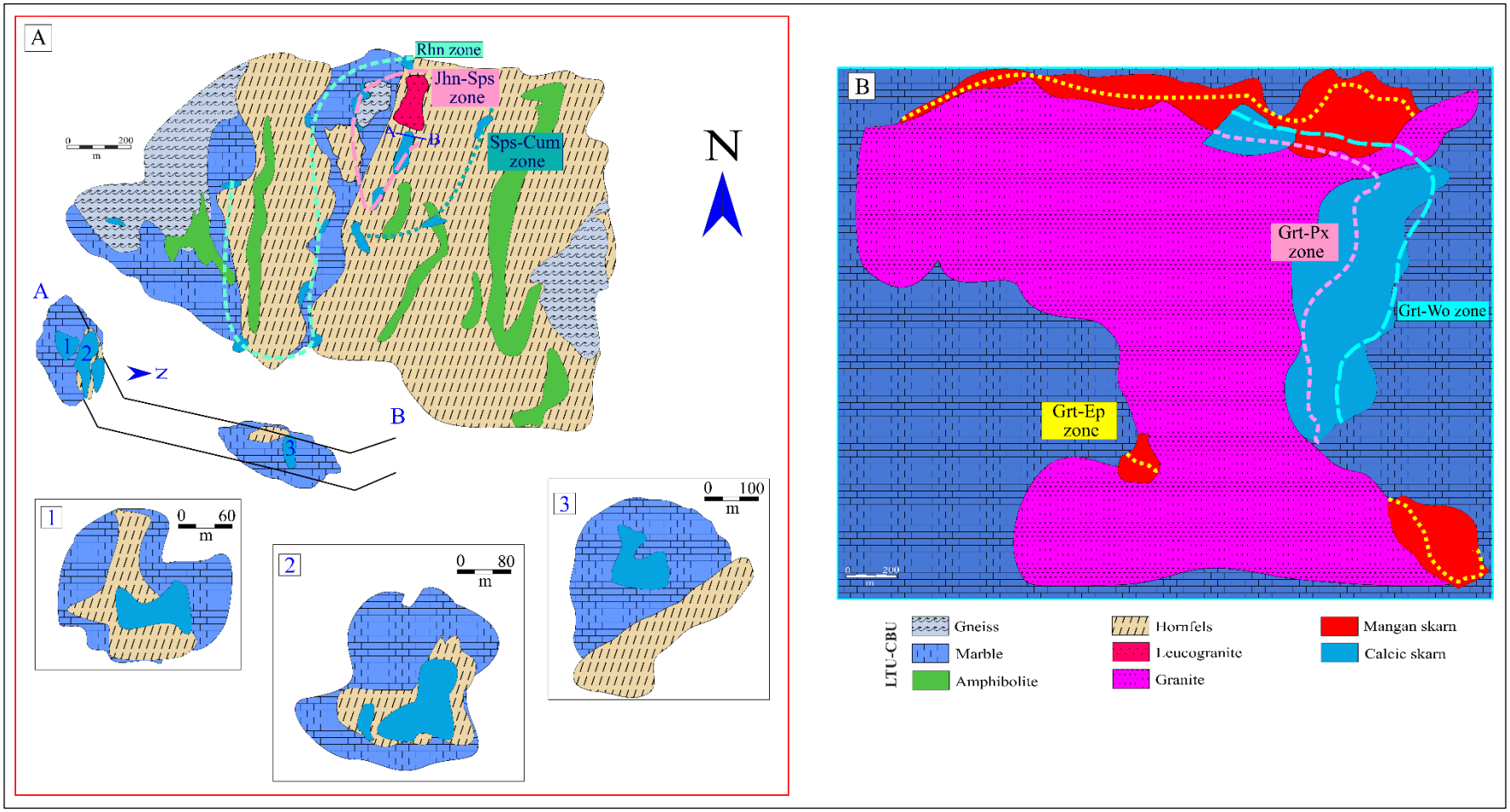

Electronic Supplementary Material, Figure 1. Schematic geological map of the mangan skarn in the mines of: (A) Thapsana in Paros and (B) Panorama (Wollastonite) in Drama.

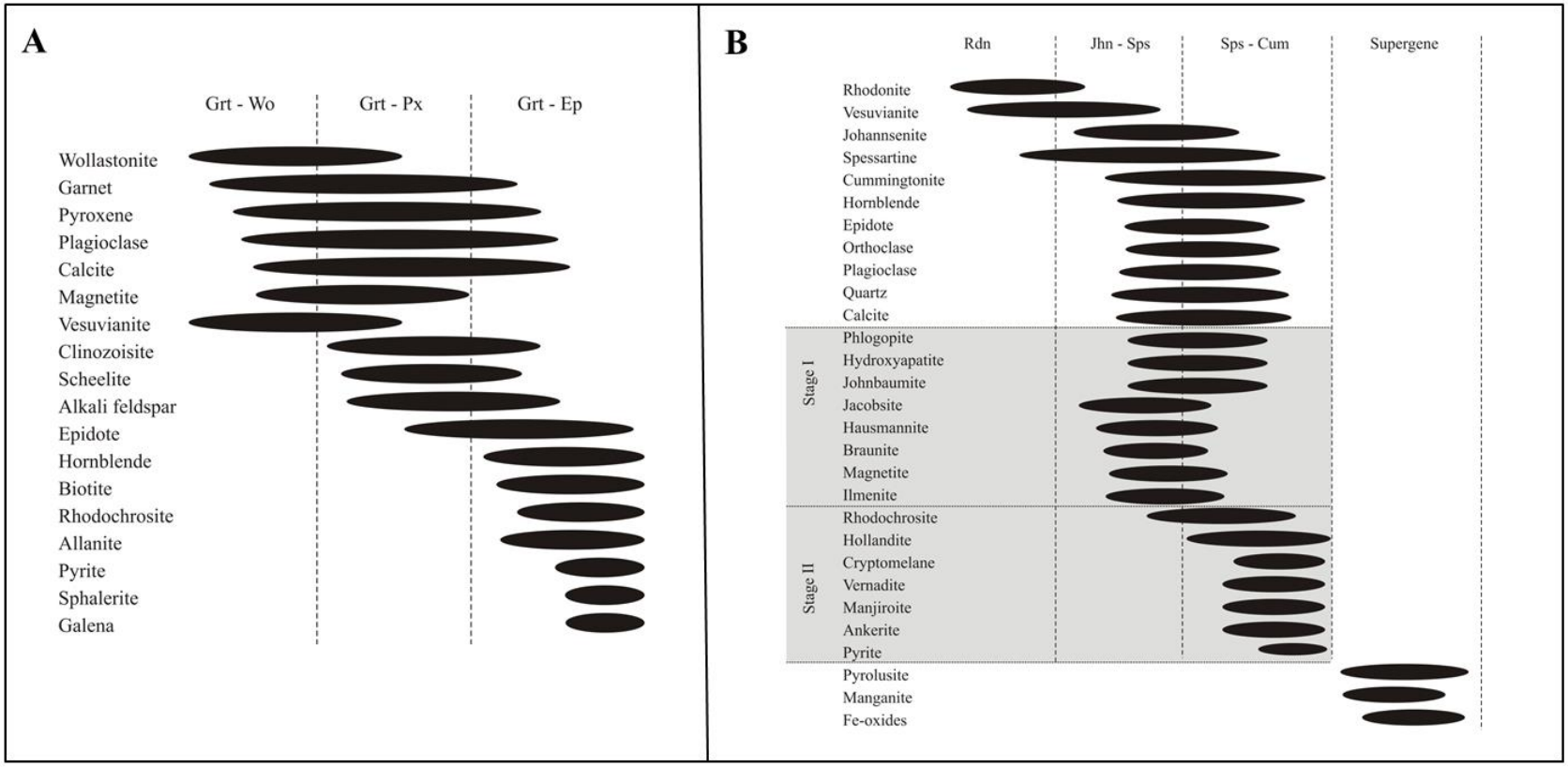

Electronic Supplementary Material, Figure 2. Paragenetic sequence of: (A) Panorama in Drama and (B): Thapsana in Paros mangan skarns.

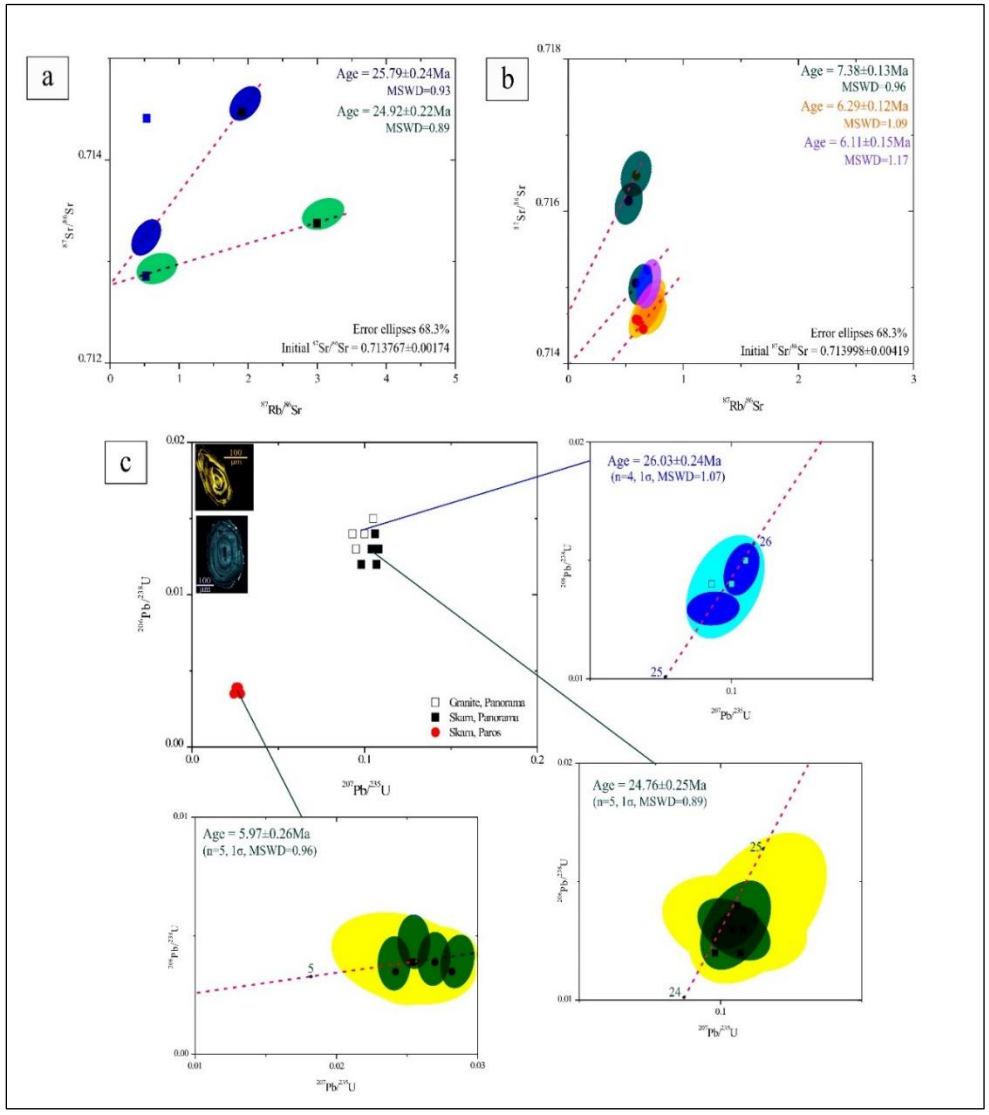

Electronic Supplementary Material, Figure 3. Rb-Sr and U-Pb age results from Panorama granite, and Panorama, Drama and Thapsana, Paros mangan skarns.

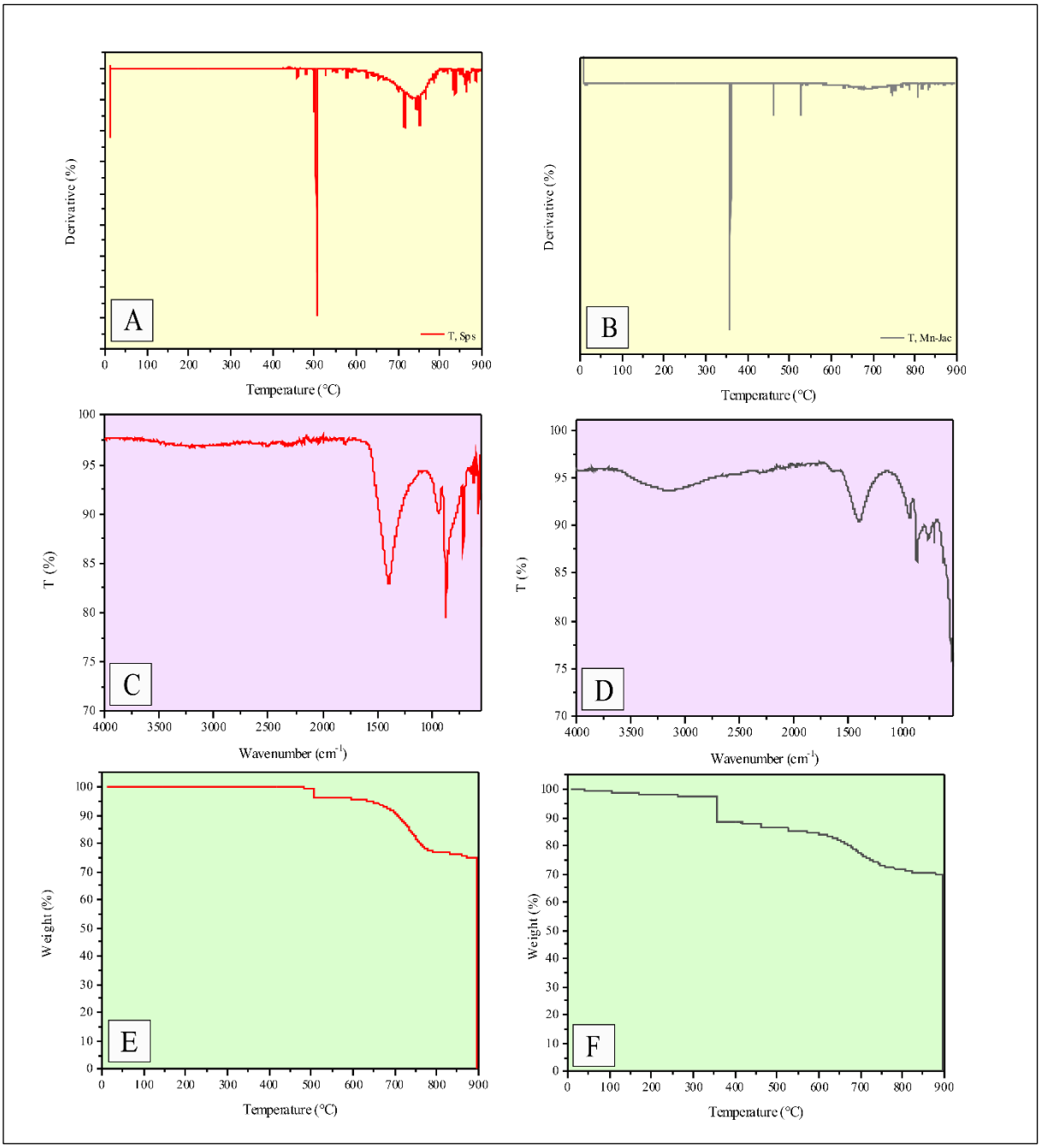

Electronic Supplementary Material, Figure 4. (A, B): Fourier-Transform Infrared Spectroscopy (FT-IR); (C, D): Differential Thermal Analysis (DTA); (E, F) Thermal Gravimetric Analysis (TGA) of spessartine (Sps) and jacobsite (Jac) from the Thapsana, Paros mangan skarn.